A&A 650, A182 (2021)
https://doi.org/10.1051/0004-6361/202039519

Astronomy & Astrophysics

Homogeneous study of Herbig Ae/Be stars from spectral energy distributions and *Gaia* EDR3⋆

J. Guzmán-Díaz[1], I. Mendigutía[1], B. Montesinos[1], R. D. Oudmaijer[2], M. Vioque[2,3,4], C. Rodrigo[1,5], E. Solano[1,5], G. Meeus[6], and P. Marcos-Arenal[1]

[1] Centro de Astrobiología (CSIC-INTA), ESA-ESAC Campus, 28692, Villanueva de la Cañada, Madrid, Spain
e-mail: jguzman@cab.inta-csic.es
[2] School of Physics and Astronomy, University of Leeds, Leeds LS2 9JT, UK
[3] Joint ALMA Observatory, Alonso de Córdova 3107, Vitacura, Santiago 763-0355, Chile
[4] National Radio Astronomy Observatory, 520 Edgemont Road, Charlottesville, VA 22903, USA
[5] Spanish Virtual Observatory, Spain
[6] Departamento Física Teórica, Facultad de Ciencias, Universidad Autónoma de Madrid, Campus de Cantoblanco, 28049 Madrid, Spain

Received 24 September 2020 / Accepted 6 April 2021

ABSTRACT

Context. Herbig Ae/Be stars (HAeBes) have so far been studied based on relatively small samples that are scattered throughout the sky. Their fundamental stellar and circumstellar parameters and statistical properties were derived with heterogeneous approaches before *Gaia*.

Aims. Our main goal is to contribute to the study of HAeBes from the largest sample of such sources to date, for which stellar and circumstellar properties have been determined homogeneously from the analysis of the spectral energy distributions (SEDs) and *Gaia* EDR3 parallaxes and photometry.

Methods. Multiwavelength photometry was compiled for 209 bona fide HAeBes for which *Gaia* EDR3 distances were estimated. Using the Virtual Observatory SED Analyser (VOSA), photospheric models were fit to the optical SEDs to derive stellar parameters, and the excesses at infrared (IR) and longer wavelengths were characterized to derive several circumstellar properties. A statistical analysis was carried out to show the potential use of such a large dataset.

Results. The stellar temperature, luminosity, radius, mass, and age were derived for each star based on optical photometry. In addition, their IR SEDs were classified according to two different schemes, and their mass accretion rates, disk masses, and the sizes of the inner dust holes were also estimated uniformly. The initial mass function fits the stellar mass distribution of the sample within $2 < M_*/M_\odot < 12$. In this aspect, the sample is therefore representative of the HAeBe regime and can be used for statistical purposes when it is taken into account that the boundaries are not well probed. Our statistical study does not reveal any connection between the SED shape from the Meeus et al. (2001, A&A, 365, 476) classification and the presence of transitional disks, which are identified here based on the SEDs that show an IR excess starting at the K band or longer wavelengths. In contrast, only ∼28% of the HAeBes have transitional disks, and the related dust disk holes are more frequent in HBes than in HAes (∼34% vs. 15%). The relatively small inner disk holes and old stellar ages estimated for most transitional HAes indicate that photoevaporation cannot be the main mechanism driving disk dissipation in these sources. In contrast, the inner disk holes and ages of most transitional HBes are consistent with the photoevaporation scenario, although these results alone do not unambiguously discard other disk dissipation mechanisms.

Conclusions. The complete dataset is available online through a Virtual Observatory-compliant archive, representing the most recent reference for statistical studies on the HAeBe regime. VOSA is a complementary tool for the future characterization of newly identified HAeBes.

Key words. protoplanetary disks – stars: pre-main sequence – stars: variables: T Tauri, Herbig Ae/Be – virtual observatory tools – stars: fundamental parameters – astronomical databases: miscellaneous

1. Introduction

The seminal work by Herbig (1960) defined the massive counterparts of T Tauri stars (TTs) as emission line objects with spectral type A or earlier that are located in obscured regions and illuminate bright and close nebulosities. This definition was subsequently nuanced. Currently, Herbig Ae/Be stars (HAeBes) are known as young ($\lesssim$10 Myr), optically visible pre-main-sequence (PMS) stars with emission lines in their spectra, typical spectral types A and B, stellar masses that typically range between ∼2 and ∼12 $M_\odot$, and infrared (IR) excesses associated with circumstellar disks. The initial list with dozens of sources (Herbig 1960) was extended with new catalogs (e.g., Finkenzeller & Mundt 1984; Herbig & Bell 1988; The et al. 1994; Carmona et al. 2010; Chen et al. 2016), and more than 200 HAeBes are known today. This is far fewer than the thousands of TTs that are known, and this discrepancy can be partially explained by the shape of the initial mass function (IMF), which favors the formation of less massive objects and the faster evolution of massive stars. Statistical studies of HAeBes are generally less reliable than those for TTs because they are not based on complete samples in different star-forming regions but on small, scattered subsamples

⋆ A copy of the complete dataset is available at the CDS via anonymous ftp to cdsarc.u-strasbg.fr (130.79.128.5) or via http://cdsarc.u-strasbg.fr/viz-bin/cat/J/A+A/650/A182

within the lists mentioned above and assume different stellar and circumstellar characterizations.

Many works have studied the stellar characterization of HAeBes (see, e.g., Montesinos et al. 2009, and references therein). However, before *Gaia*, most referred to relatively small samples and used different approaches to derive the stellar parameters. A major step toward a uniform characterization of HAeBes was made by Vioque et al. (2018), who placed 252 HAeBes in the HR diagram based on parallaxes from *Gaia* DR2 (Gaia Collaboration 2016, 2018; Lindegren et al. 2018). The stellar temperatures, gravities, extinctions, and other parameters were compiled from previous works in the literature, and the subsequent stellar luminosities, masses, and ages were then homogeneously inferred from the same atmospheric models and evolutionary tracks. Similarly, Arun et al. (2019) derived a homogeneous set of stellar parameters for 131 HAeBes, this time based on *Gaia* DR2 parallaxes and magnitudes alone (Lindegren et al. 2018; Riello et al. 2018). The most relevant reference for self-consistently obtained stellar parameters of HAeBes is the work by Wichittanakom et al. (2020; W2020 hereafter). This paper did not only update most of the spectroscopically determined stellar masses, luminosities, surface gravities, and ages of southern HAeBes derived by Fairlamb et al. (2015) using *Gaia* DR2 distances, but extended the same spectroscopic analysis to additional HAeBes in the north. Thus, W2020 represents the most reliable and homogeneous stellar characterization of a wide sample of HAeBes to date, including spectroscopically determined data for 121 such stars mostly based on *Gaia* DR2 distances.

An important caveat that was soon recognized as a result of the stellar characterization of HAeBes is that they do not constitute a homogeneous group. The group consists of two subsamples, HAes and HBes, that have specific ranges in stellar parameter space. In particular, HAes have relatively old ages and low masses (typically >3 Myr and 2–3 $M_{\odot}$), while HBes are younger and more massive (typically <3 Myr and >3 $M_{\odot}$). While the scarcity of old HBes results from the faster stellar evolution toward the main sequence (MS) with increasing stellar mass, the lack of very young HAes probably results from two main reasons. First, HAes become optically visible later in their evolution, and second, the younger population of intermediate-mass T Tauri stars (IMTTs) that will evolve into HAes is not well probed. For a related discussion, we refer to van Boekel et al. (2005); Calvet et al. (2004) and Mendigutía et al. (2011b), among others.

Regarding the circumstellar properties, disk-to-star accretion rates of relatively wide samples of HAeBes have been estimated either directly by modeling the near-ultraviolet (UV) excess (Blondel & Djie 2006; Mendigutía et al. 2011b; Fairlamb et al. 2015) or indirectly through correlations with spectroscopic emission lines (Garcia Lopez et al. 2006; Arun et al. 2019; W2020). Concerning the characterization of disk regions farther away from the star, the relative brightness and proximity of HAeBes make them the ideal targets for observations with high spatial resolution with the most advanced instrumentation (e.g., Dong et al. 2018, and references therein). However, these techniques are still affected by significant observational biases (Garufi et al. 2018), and for statistical purposes, we must still rely mainly on the analysis of the spectral energy distributions (SEDs) in the IR and longer wavelengths (e.g., Strom et al. 1989; Hillenbrand et al. 1992). A commonly adopted scheme to classify the SEDs of HAeBes was proposed by Meeus et al. (2001), who divided 14 such sources into two groups depending on the shape of their SEDs: Group I, in which the continuum from the IR to the submillimeter region could be fit by a power-law component plus a cool blackbody, and group II, in which only the power-law component was necessary to make the fit. It has been shown that the Meeus groups might be related to the disk geometry (Meeus et al. 2001; Dullemond 2002; Dullemond & Dominik 2004; Maaskant et al. 2013), the UXOr-type variability (Dullemond et al. 2003), the presence of organic molecules (Meeus et al. 2001; Acke & van den Ancker 2004), or the dust grain growth (Acke et al. 2004; Meijer et al. 2008), among others. While most previous works initially indicated an evolution from group I to group II, a more complex view is emerging, and there seems to be no evolutionary trend at the moment (Mendigutía et al. 2012; Maaskant et al. 2013; Garufi et al. 2017). The difference between the two groups is mainly related to the presence of gaps and cavities, as shown in high-resolution imaging (Maaskant et al. 2013; Honda et al. 2015; Garufi et al. 2017), which in turn may be connected with the potential presence of giant planets (Kama et al. 2015). Other works characterizing the circumstellar properties of HAeBes include the determination of their disk masses (e.g., Alonso-Albi et al. 2009; Mendigutía et al. 2012; Dong et al. 2018) or their K band inner dust disk radii from interferometry (Monnier & Millan-Gabet 2002; Eisner et al. 2003, 2004; Monnier et al. 2005; GRAVITY Collaboration 2019). Taken together, previous works suggest that HBes tend to have lower dust disk masses from millimeter-continuum fluxes (Alonso-Albi et al. 2009; Vioque et al. 2018) and dust inner radii from interferometric near- and mid-IR observations (e.g., Monnier et al. 2005, and references therein) than expected from the corresponding trends followed by TTs and HAes. These add to the possible differences between the physical mechanisms driving accretion in the two types of sources (see, e.g., the recent review in Mendigutía 2020; W2020, and references therein). A major caveat is the relatively small samples and heterogeneous approaches from which many of the previous conclusions related to the circumstellar properties of HAeBes were inferred. This situation is changing because more complete samples are analyzed now (Vioque et al. 2018, 2020).

Here, we contribute to the study of the HAeBe regime by providing a homogeneous characterization of the stellar and circumstellar properties of most of these confirmed sources, based on their complete SEDs from multiwavelength photometry. For all stars we make use of the recent *Gaia* Early Data Release 3 (EDR3, Gaia Collaboration 2016, 2021) parallaxes and photometry (Lindegren et al. 2021; Riello et al. 2021). Section 2 describes how the stellar and disk parameters were obtained using the same procedure for all stars, as well as the online archive in which these data are publicly available. Section 3 serves to exemplify the potential use of our dataset for the study of the HAeBe regime. It includes some general statistics that is mainly focused on the analysis of the different circumstellar properties of HAes and HBes as inferred from their SEDs. Finally, Sect. 4 includes a brief summary and conclusions.

2. Sample and results

The initial sample we selected included the 252 HAeBes studied in Vioque et al. (2018). However, some sources were excluded for reasons related to strong variability or the lack of enough photometric points, which altogether prevented us from extracting the full set of parameters from an SED analysis. In addition, stars that were recently discarded as HAeBes in Appendix A of Vioque et al. (2020) were not included here. Finally, some other sources were excluded because they lie below the MS in the HR diagram according to Vioque et al. (2018) or W2020, and the new *Gaia* EDR3 distances do not change this situation (see also Sect. 2.1). The SED-based stellar and circumstellar

characterization was finally carried out for the 209 bona fide HAeBes with coordinates (RA, DEC) listed in Cols. 1, 2, and 3 of Table B.1. Distance-independent stellar temperatures and visual extinctions inferred from them were derived by W2020 based on optical spectroscopy for 93 of the stars in our sample. These stars are indicated with italics, and their corresponding temperature (and extinction) values are included in Table B.1 in addition to our estimates because they serve as a main reference (see Sects. 2.1 and 3 and also Appendix A).

The SED analysis relies on the following distances and photometry. The distances were estimated based on the parallaxes provided in *Gaia* EDR3 (Lindegren et al. 2021). Following Bailer-Jones et al. (2021), the inverse of the parallax was used to estimate the distances when the fractional parallax error (*fpe*) was smaller than 0.1. A Bayesian method with a geometric prior from Bailer-Jones et al. (2021) was used to derive the distances in case $fpe > 0.1$, or when the parallax was negative. The distances for the 209 HAeBes in the sample are listed in Col. 4 of Table B.1. In addition, we assumed that a low-quality parallax and thus a potentially spurious distance can be obtained when any of the following criteria based on *Gaia* EDR3 parallaxes, uncertainties and quality flags are met: First, negative parallax or $fpe > 1$. Second, renormalised unit weight error (RUWE) > 3. Third, astrometric_excess_noise >0.5 and astrometric_excess_noise sig >2. Finally, RUWE >1.4 and ipd_gof_harmonic_amplitude >0.1. The last three criteria were defined according to Table 4 of Lindegren et al. (2021) and Sect. 3.2 of Fabricius et al. (2021). The 42 objects indicated with the dagger in Table B.1 have low-quality parallaxes according to the criteria listed above. Although we also derived the stellar and circumstellar properties of these objects, they were not considered in the analysis (Sect. 3). The potential spuriousness of *Gaia* EDR3 astrometric solutions is subject of ongoing work, for which we adopted conservative criteria. For instance, essentially all stars with low-quality parallaxes based on the very recent work by Rybizki et al. (2021) are also identified here, although roughly half of the sources with low-quality parallaxes according to our criteria are not classified as such based on Rybizki et al. (2021).

We used the online tool Virtual Observatory SED Analyser (VOSA)[1], developed by the Spanish Virtual Observatory, to automatically compile photometry from the UV to the IR from the available catalogs in the Virtual Observatory[2]. In addition to the new *Gaia* EDR3 photometry (Riello et al. 2021), we included data from GALEX[3] (Bianchi & GALEX Team 2000), APASS[4] 9 (Evans et al. 2002), the Stroemgren-Crawford uvbyβ photometry catalog (Paunzen 2015), 2MASS[5] (Skrutskie et al. 2006), WISE[6] (Wright et al. 2010); IRAS[7] (Beichman et al. 1988; Helou & Walker 1988), *Spitzer* (Evans et al. 2009), and AKARI (Kawada et al. 2007; Ishihara et al. 2010), among others. Information about the quality of the photometry is available in the catalogs, and the photometric points with poor-quality flags were discarded. Additional UBVRI and L,M photometry was extracted when necessary (Reed 2003; Vieira et al. 2003; Kun et al. 2009; Alfonso-Garzón et al. 2012; Mendigutía et al. 2012; Zacharias et al. 2012; Fairlamb et al. 2015). Fluxes at millimeter wavelengths were also used in this work, as indicated in Sect. 2.2.3.

[1] http://svo2.cab.inta-csic.es/theory/vosa
[2] http://svo2.cab.inta-csic.es/theory/vosa/help.php?what=credits#credits:vophot
[3] Galaxy Evolution Explorer.
[4] AAVSO Photometric All-Sky Survey.
[5] Two Micron All-Sky Survey.
[6] Wide-Field Infrared Survey Explore.
[7] Infrared Astronomical Satellite.

2.1. Stellar characterization

VOSA allows us to determine the stellar parameters comparing the observed SED with the synthetic photometry from photospheric theoretical models using a χ^2 test (see Bayo et al. 2008, for details). This tool enables us to restrict the models to those within a given range of stellar temperatures (T_*). We used this option by using the models with T_* values that were constrained by the error bars provided by Vioque et al. (2018), except for the HAeBes that are listed in W2020, for which their more recent and homogeneous estimates have been considered (see Col. 5 of Table B.1). It is also possible to constrain the visual extinction, A_V, but we let it be virtually free, providing a wide range of A_V from 0 to 10 mag for all HAeBes. VOSA then provides the combination of A_V and T_* that best fits Kurucz ODFNEW/NOVER models (Castelli et al. 1997) to the dereddened SEDs using the interstellar extinction law by Fitzpatrick (1999) that was improved by Indebetouw et al. (2005). The final A_V and T_* values resulting from these fits are listed in Cols. 6 and 7 of Table B.1. Uncertainties in both parameters were estimated by performing a 100-iteration Monte Carlo simulation. In the case of T_*, if the standard deviation is larger than half the grid step for the temperature, VOSA reports it as the uncertainty. Otherwise, half the grid step is the uncertainty of this parameter. Details about the procedure can be obtained from the online help provided in the VOSA web page. The uncertainties for the remaining stellar parameters (see below) depend on the previous uncertainties, which only reflect error bars derived from the SED fitting. A comparison with earlier determinations is included in Appendix A. The Kurucz models also depend on the surface gravities and metallicities, which were varied within the range of $\log g$ between 2.0 and 4.5 (g in cm s^{-2}), and [Fe/H] between −0.5 and +0.5 (where $[\mathrm{Fe/H}] = (\log N_{\mathrm{Fe}}/\log N_{\mathrm{H}})_* - (\log N_{\mathrm{Fe}}/\log N_{\mathrm{H}})_\odot$). However, the corresponding best-fit results are not tabulated because they do not produce significant changes in the shape of the SEDs, and thus they may not be representative.

Photometry at wavelengths shorter than U band or longer than J band was not generally considered to fit the photospheres because an excess may be present due to accretion and dust emission, respectively. However, after visual inspection, several sources without excesses show photospheric emission extending over a wider wavelength range. In these cases, the fitting procedure was repeated considering that range. This resulted in a lower χ^2 value. In addition, only the photometric points with the highest fluxes were fit when multiple, scattered data were available for the same wavelengths. This serves to reflect the brightest (less extincted) state in variable sources. A minimum of six photometric points in the optical were used to carry out the fit for each star, which also served to minimize uncertainties. The dereddened SEDs and their photospheric fits are plotted in Appendix C.

After we fit the photospheres, spectral types were associated with the resulting stellar temperatures using the relation in Kenyon & Hartmann (1995). They are listed in Col. 8 of Table B.1. In addition, VOSA derives the stellar luminosity as $L_* = 4\pi d^2 F_*$, where F_* is the dereddened flux derived from the integration of the best-fitting model (see Appendix A in Bayo et al. 2008). The stellar radius was then estimated as $R_* = (L_*/4\pi\sigma_{\mathrm{SB}} T_*^4)^{1/2}$, where σ_{SB} is the Stefan-Boltzmann constant. The stellar radius and luminosity for each star, as

well as their propagated errors, are listed in Cols. 9 and 10 of Table B.1.

Finally, VOSA allows us to estimate the stellar masses (M_*) and ages (t_*) through the comparison with several isochrones and evolutionary tracks. In our case, PARSEC V2.1s[8] stellar tracks and isochrones from Bressan et al. (2012) were used. Using the error bars in T_* and L_* obtained in the fit process, we derived the minimum and maximum possible values for M_* and t_*, which were used as an estimate of the corresponding error bars. Stellar ages, masses, and their corresponding errors are included in Cols. 11 and 12 of Table B.1.

Three objects for which different initial constraints of temperature were used with respect to those described previously deserve special mention. A wider initial temperature range was given for HD 290500 and HD 288012 (8500–10 500 K and 7250–12 250 K, respectively), whereas the relatively narrow range around the temperature value determined in Meeus et al. (2010) was fixed for HD 169142 (7000–8000 K). We followed a different strategy for these HAeBes because under the initial approach, they appear to be located below the MS line in the HR diagram. The new T_* constraints provide fits that are consistent with the PMS zone and allow VOSA to derive reasonable values for M_* and t_*.

2.2. Circumstellar characterization

The previous SEDs and stellar parameters allow us to characterize circumstellar properties of the sample of HAeBes in terms of IR-SED classification, disk-to-star accretion rates, disk masses, and inner disk sizes. We describe these next.

2.2.1. SED classification

Infrared-SEDs were classified into groups I and II from the Meeus et al. (2001) scheme, which we call "M01" classification hereafter. The ratio between the near-IR and the mid-IR luminosity, $L_{\rm NIR}/L_{\rm IR}$, and the non-color-corrected IRAS color, [12]−[60], were used to carry out this classification following the procedure in van Boekel et al. (2003) and Acke et al. (2004). When the required *J, H, K, L, M*, or IRAS photometry was not available, the corresponding fluxes were estimated by interpolation from adjacent data. A few HAeBes that lie close to the limit of groups I or II or have IRAS fluxes that are upper limits were classified from direct visual inspection of their SEDs and comparing these classifications with those in other works (Acke et al. 2005, 2010; Acke & van den Ancker 2006; Mendigutía et al. 2012). As a result, four stars in the sample have a dubious group I or II classification. In addition, 23 sources cannot be classified because photometry was not available in the relevant ranges. It is also noted that the IRAS bands may be contaminated by the environment close to some stars (Verhoeff et al. 2012; Jiménez-Donaire et al. 2017), which may affect the M01 group assignment.

In addition, the SEDs were also classified in a classical approach similar to that in Strom et al. (1989). In particular, we followed the criteria adopted in Mendigutía et al. (2012) based on the shortest wavelength from which the infrared excess starts. This wavelength corresponds to the first photometric point that is not fit by the photosperic model from VOSA, which in turn is related to the sizes of the inner dust disk holes (see Sect. 2.2.4). In this way, sources belong to groups *J, H*, or *K* if the shortest wavelength at which the IR excess is apparent corresponds to these near-IR bands (1.24, 1.66, and 2.16 µm, respectively), and they belong to group $>K$ if the IR starts at $\lambda > 2.16$ µm. This scheme is called *JHK* classification hereafter. The results of the SED classification from the M01 and *JHK* criteria are listed in Cols. 2 and 3 of Table B.2.

2.2.2. Disk-to-star accretion rates

Accretion luminosities ($L_{\rm acc}$) were derived from the new empirical correlations with L_* quantified in W2020, which depend on the stellar mass: $\log(L_{\rm acc}/L_\odot) = (-0.87 \pm 0.11) + (1.03 \pm 0.08) \times \log(L_*/L_\odot)$ for $M_* < 4\,M_\odot$, and $\log(L_{\rm acc}/L_\odot) = (0.19 \pm 0.27) + (0.60 \pm 0.08) \times \log(L_*/L_\odot)$ for $M_* > 4\,M_\odot$. Mass accretion rates were then estimated from the usual expression,

$$\dot{M}_{\rm acc} = \frac{L_{\rm acc} R_*}{G M_*}\left(1 - \frac{R_*}{R_i}\right)^{-1}, \quad (1)$$

where R_i is the disk truncation radius from which gas is channeled onto the star. For simplicity, we assumed that $R_i = 2.5\ R_*$ for all sources (Mendigutía et al. 2011a). Mass accretion rates and accretion luminosities are included in Cols. 4 and 5 of Table B.2.

Although accretion estimates from emission line luminosities and from L_* are roughly equivalent and accurate for most stars (Mendigutía et al. 2015), the latter was chosen because it allowed us to derive accretion rates based on self-consistent data derived in this work using a homogeneous criterion for the whole sample. Emission line luminosities (in Hα or any other line) in the literature come from relatively heterogenous measurements, and more importantly, they are not available for all stars. However, accretion luminosities and mass accretion rates based on empirical correlations with the stellar (or emission line) luminosities may be incorrectly high in a few sources that do not show evidence of accretion based on a direct probe such as the near-UV excess (see Mendigutía et al. 2011b; Fairlamb et al. 2015, for the corresponding measurements in some HAeBes). Moreover, it must be taken into account that mass accretion rates for HBes have strong associated uncertainties because accretion rates are poorly known in this regime (for details, see, e.g., Mendigutía 2020; W2020, and references therein).

2.2.3. Disk masses

Continuum fluxes at millimeter and submillimeter wavelengths are commonly used to derive total (dust + gas) disk masses ($M_{\rm disk}$), making the assumption that the emission at these wavelengths is optically thin and that the gas-to-dust mass ratio is equal to 100 (e.g., Beckwith et al. 1990). In the Rayleigh-Jeans limit,

$$M_{\rm disk} = F_\nu \frac{d^2}{2kT_{\rm D}} \frac{c^2}{\nu^2 \kappa_\nu}, \quad (2)$$

where F_ν is the measured flux (normally at 1.3 mm), $T_{\rm D}$ is the dust temperature, k is the Boltzmann constant, and κ_ν is the opacity. Total disk masses are determined from the previous expression for ∼1/3 of the stars in the sample (those for which previous F_ν measurements are available). We adopted $\kappa_{1.3\,\rm mm} = 0.02\,{\rm cm^{-2}\,g^{-1}}$, which already includes a gas-to-dust ratio = 100, and a wavelength dependence $\kappa_{\rm mm} \propto \lambda^{-\beta}$ (Beckwith et al. 1990)[9], where $0 < \beta \leq 2$ is the dust opacity

[8] https://people.sissa.it/~sbressan/parsec.html

[9] I.e., opacities at different wavelengths are given by $\kappa_\lambda = \kappa_{1.3\,\rm mm}/(\lambda/1.3)^{-\beta}$

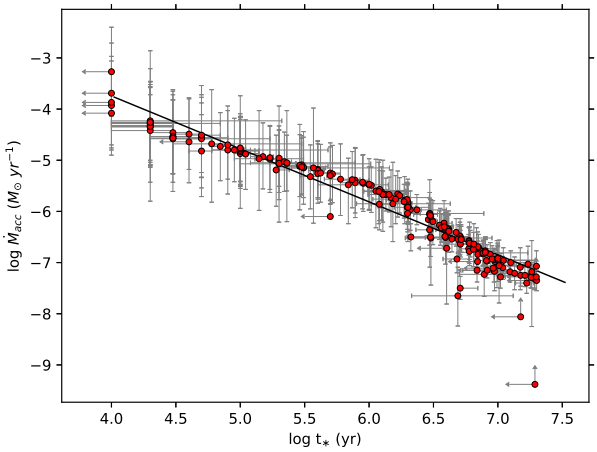

Fig. 1. Mass accretion rate vs. stellar age. The best power-law fit ($\eta = 1.03 \pm 0.02$) is plotted with a solid line. Upper and lower limits are indicated by arrows.

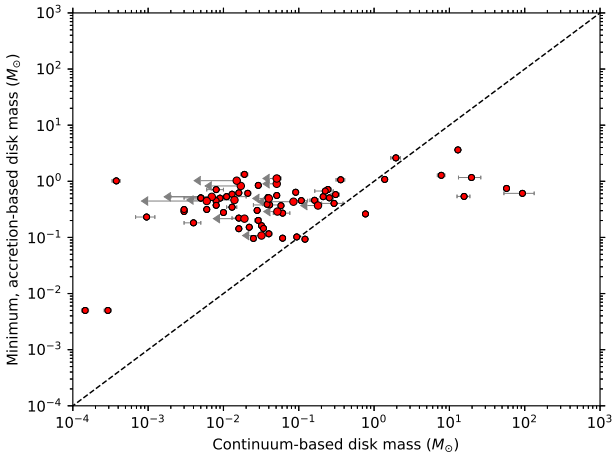

Fig. 2. Disk masses from accretion and age vs. those from dust emission at millimeter wavelengths. Upper limits are represented by arrows. The dashed black line indicates equal values.

index associated with the typical dust grain size probed at (sub-) millimeter wavelengths (1.5–2 for the interstellar medium and smaller for larger grains). The values for T_D and β are inferred from the best graybody model that fits the observed millimeter photometry using a χ^2 criterion (see, e.g., Andre et al. 1993; Sandell 2000; Mendigutía et al. 2012). For the HAeBes with one single measurement of the millimeter flux, β was fixed to 1 and T_D to the value in Table II of Natta et al. (2000) associated with the corresponding spectral type. The values of β, T_D and M_{disk} are listed in Cols. 2, 3, and 4 of Table B.3 whenever these estimates have been possible, and Cols. 5 and 6 show the number of photometric points and the corresponding references that we used. The errors in M_{disk} were determined by propagation, considering only the uncertainties in the (sub-) millimeter fluxes. For the few flux values without associated error bars in the literature, typical ∼10% uncertainties were assigned.

Nevertheless, several studies have pointed out that disk masses derived from dust continuum emission could be underestimated (see, e.g., Zhu et al. 2019; Ballering & Eisner 2019, and references therein). An alternative method for estimating the disk mass is followed in this paper. It is based on previous works that inferred that parameter from measurements of the stellar mass accretion rates and ages (Hartmann et al. 1998; Andrews & Williams 2007; Mendigutía et al. 2012; Dong et al. 2018). Given that a significant fraction of the disk is dissipated through accretion onto the star, a lower limit for the current gas disk mass is given by

$$M_{disk}^{min}(t_*) \equiv M_{disk}^{min} = \int_{t_*}^{t_{MS}} \dot{M}_{acc}(t)\,dt, \quad (3)$$

t_{MS} being the zero-age main sequence, when the gas disk mass is negligible. A relation between $\dot{M}_{acc}$ and age with the shape $\dot{M}_{acc} = At^{-\eta}$ is commonly considered (e.g., Hartmann et al. 1998; Sicilia-Aguilar et al. 2010; Mendigutía et al. 2012; De Marchi et al. 2017; Arun et al. 2019), where the constant A is determined under the condition $\dot{M}_{acc}(t_*) = \dot{M}_{acc}$. We replaced $\dot{M}_{acc}$ by the power law in Eq. (3) and resolved the integral,

$$M_{disk}^{min} = \frac{\dot{M}_{acc}(t_*)t_*}{\eta - 1} \times \left\{1 - \left(\frac{t_*}{t_{MS}}\right)^{\eta-1}\right\}. \quad (4)$$

In order to derive M_{disk}^{min} values from the previous expression, the value of η characterizing the accretion evolution of the HAeBes is needed. Figure 1 shows the accretion rates and stellar ages that were previously derived for the stars in our sample. The best power-law fit without considering upper and lower limits has an exponent $\eta = 1.03 \pm 0.02$. This value indicates a slightly shallower decline than previously estimated by Mendigutía et al. (2012) ($\eta = 1.8^{+1.4}_{-0.7}$) and Arun et al. (2019) ($\eta = 1.2 \pm 0.1$). M_{disk}^{min} was then estimated for each star in our sample from Eq. (4), using t_{MS} values from Tayler (1994). Negative disk masses were obtained for 31 stars with $t_* > t_{MS}$, as indicated in Table B.2. In these cases, M_{disk}^{min} was derived again assuming either the minimum values of t_* and M_* from this work or the values of the same stellar parameters plus the $\dot{M}_{acc}$ values from the literature (Vioque et al. 2018, W2020). Furthermore, for HAeBes with upper limits on t_* and M_*, the values from Vioque et al. (2018) and W2020 were also used (for the specific case of HD 169142, the age was obtained from Grady et al. 2007). M_{disk}^{min} values for all stars in the sample are included in Col. 6 of Table B.2.

Figure 2 compares the disk mass estimates from dust continuum emission and from accretion rates. Six sources have extremely high continuum-based disk masses >2 $M_\odot$ that may reflect contamination of the millimeter fluxes from envelopes or the surroundings. For the others, our data support previous claims indicating that continuum-based disk masses are typically lower than those inferred from accretion by about one order of magnitude (Hartmann et al. 1998; Andrews & Williams 2007; Mendigutía et al. 2012; Dong et al. 2018), probably suggesting that dust emission does not reflect the whole solid population in a protoplanetary disk. However, we note that accretion-based disk masses can be unrealistically high in several sources because the accretion rate decline commonly inferred through the comparison between accretion rates and ages (like in Fig. 1) does not consider the corresponding nonaccreting fractions, which can be significant at least in well-studied samples of TTs (e.g., Fedele et al. 2010). Moreover, the accretion rate decline shown in Fig. 1 also reflects the underlying dependence of $\dot{M}_{acc}$ and M_* (as described in Sect. 1, more massive objects are also younger and thus show higher accretion rates; see, e.g., Mendigutía et al. 2011b). W2020 studied the accretion rate decline by dividing the sample of HAeBes into different stellar mass bins, showing that the decay of accretion with age persists for the mass range

2.0–2.5 $M_\odot$ but perhaps not for more massive stars that were less well sampled. Accretion-based disk masses are provided here for the whole sample and not just for a fraction like continuum-based disk masses (Tables B.2 and B.3, respectively), but the previous caveats concerning both types of estimates must be taken into account.

2.2.4. Inner dust holes

The sizes of the inner dust holes ($r_{\rm in}$) for the HAeBes of our sample were estimated from their SEDs as follows. First, we assumed that the disk temperature decreases with the distance as $T_{\rm disk} = K \times r^{-3/4}$ (e.g., Armitage 2009). For each star, the constant K was estimated by replacing $T_{\rm disk}$ by the dust sublimation temperature $T_{\rm sub}$, assumed to be 2000 K, and r by the dust sublimation radius, $r_{\rm sub} = R_*(T_{\rm sub}/T_*)^{-2.1}$ (Robitaille et al. 2006). When the value of the constant is known, the size of the inner dust holes corresponding to the disk temperatures where the IR excess starts, determined from the Wien law and the SEDs, were derived from the above expression for $T_{\rm disk}$. The size of the inner dust holes is listed in Col. 8 of Table B.2 along with its corresponding errors, which were determined by propagation considering the effective width of the photometric filter where the IR excess starts as the only uncertainty. As described in Sect. 2.2.1, the SED classification based on the *JHK* groups is directly related to the size of the inner disk dust holes estimated here, with the relative sizes increasing from group *J* to group >*K*.

2.3. Online archive of HAeBes

All data derived in the previous sections are collected in an online archive of HAeBes[10], including the already introduced tables associated with this paper. This is a Virtual Observatory-compliant archive built in the framework of the Spanish VO using the SVOCat[11] publishing tool. Additional features of the archive include individual figures showing the SEDs, and a tool for visualizing the on-sky position of the stars. The archive will be updated to include new HAeBes that are confirmed and characterized in the future, constituting a unique tool for the study of this type of objects from a homogeneous characterization of their properties.

3. Analysis and discussion

In this section, we carry out a statistical analysis and discuss part of the previous results, focusing on different relations in the M01 and JHK SED classifications, stellar parameter accretion rates, and the mechanisms dissipating the inner part of the disks. Stellar and circumstellar parameters derived in previous sections and based on up to date *Gaia* EDR3 distances are used in the analysis, with the only exception of the stellar effective temperature (i.e., spectral type). Although our own estimates are used for the majority of the stars, the effective temperatures in W2020 (and the corresponding spectral types based on the relation in Kenyon & Hartmann 1995) are used for the subsample included in both works. The reason is that T_* is a distance-independent parameter that was derived homogeneously by W2020 based on optical spectra instead of photometry, thus using a more accurate method. However, because we used the error bars provided by W2020 to define the initial ranges of T_* for the SED fitting (Sect. 2.1), the overall results remain essentially the same when our T_* estimates are used for the whole sample. Finally, we recall that the 42 objects whose parallaxes might be spurious according to the discussion at the beginning of Sect. 2 are not considered in this statistical study.

3.1. Representativeness of the sample

This work provides the largest dataset to date of stellar and circumstellar parameters of HAeBes homogeneously derived from SEDs. However, this sample was compiled from catalogs that do not take into account completeness criteria concerning specific star-forming regions or brightness limits (see the detailed discussion in Vioque et al. 2018), as is common for lower-mass TTs, for instance. Before we carry out any statistical analysis, it is therefore worth asking what the sample represents. As we mentioned in the introduction, HAeBes are heterogeneous by definition, and the specific distributions of HAes and HBes concerning stellar mass and age must be taken into account when statistical results are interpreted (see Sects. 2.2.3, 3.2, 3.4). In addition to the well-known caveats, we discuss below whether our sample represents HAes and HBes well, or if, on the contrary, the relative number of stars included in the subsamples is physically unrealistic.

Figure 3 (top) shows in blue the distribution of the sample as a function of the spectral type. The sample contains 46 HAes and 98 HBes (mostly late type), the remaining being within the boundaries, 21 IMTTs, defined here as the stars with F and later spectral types, and 2 O-type stars. These numbers imply proportions of ∼28% and ∼59% of HAes and HBes, respectively. That the number of HBes is larger than the number of HAes was discussed in Vioque et al. (2018) (see also The et al. 1994), who pointed out that it probably reflects an observational bias resulting from the fact that HBes are brighter and extend over a larger volume in the sky. As we show next, this bias is even more significant when we consider the fractions of A and B stars after the HAeBes reach the MS.

The orange histogram in Fig. 3 (top) represents the future distribution of spectral types that the objects would have when they settle into the MS. These predicted spectral types were derived from the stellar temperatures corresponding to the points at which the MS starts, as inferred from the evolutionary tracks of each star. Although IMTTs will transform into A-stars (Calvet et al. 2004), most of these objects are not considered in the original HAeBe catalogs from which our sample has been compiled. In turn, many HAes will transform into B sources, and only a few early-type HBes will end up as O-sources when they reach the MS. As a result, the ratio between the number of B and A in the MS (2.7) is even higher than the corresponding ratio between HBes and HAes in the PMS (2.1). This is a consequence of our own definition of HAeBes as "the massive counterparts of classical TTs" , that is, emission line PMS stars with spectral types A and B, instead of "the precursors of A and B MS stars". If the latter definition were adopted, our sample of HAeBes would be biased in the sense that it lacks IMTTs and contains an excess of hot sources that will transform into O-stars.

Figure 3 (bottom) shows the stellar mass distribution for the HAeBes in our sample, which has to be very similar to the mass distribution when the objects reach the MS. The expected distribution of spectral types (orange bars in Fig. 3, top) was derived under the approximation that the mass gained by the stars due to accretion during the optically visible PMS evolution is negligible compared with the stellar mass in this evolutionary stage (i.e., most stellar mass is accreted during previous, embedded phases). Therefore it is useful to compare the histogram in Fig. 3

[10] "HArchiBe": http://svo2.cab.inta-csic.es/projects/harchibe/
[11] http://svo2.cab.inta-csic.es/vocats/SVOCat-doc/

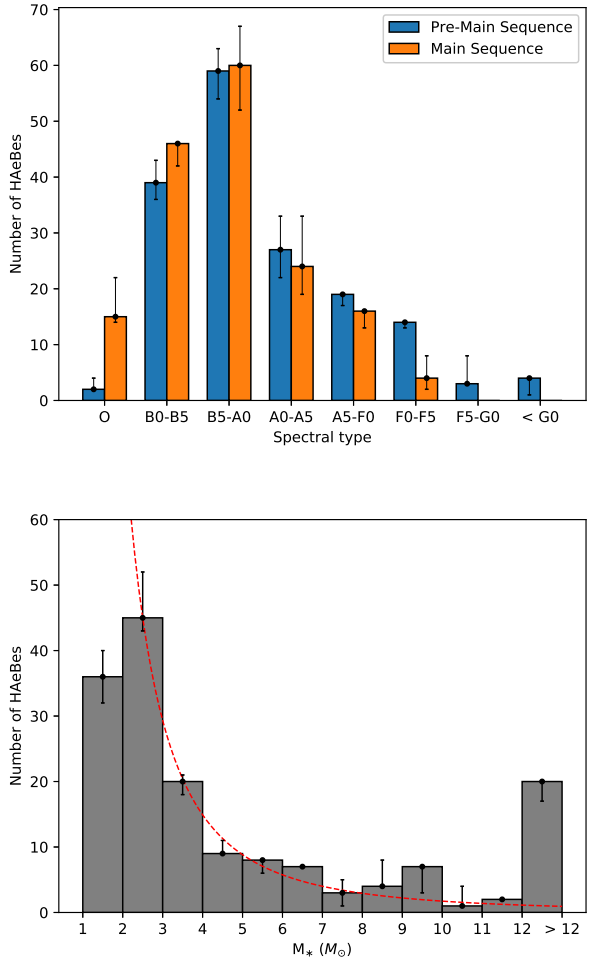

Fig. 3. *Top panel:* current distribution of spectral types in the PMS and expected distribution when the stars reach the MS, as indicated in the legend. The error bars reflect the uncertainties on the spectral types. *Bottom panel:* number of HAeBes vs. stellar mass. The error bars for the number of stars per bin considering the uncertainties in M_* are indicated. The dashed red line corresponds to the IMF (Salpeter 1955) normalized to the bin 2–3 $M_\odot$. Stars with masses >12 $M_\odot$ have been grouped together for simplicity.

(bottom) with the IMF, which by definition reflects the expected mass distribution when the stars reach the MS. The comparison with the IMF from Salpeter (1955)[12] confirms that our sample is indeed representative in this sense (Vioque et al. 2018), at least within the stellar mass range between 2 and 12 $M_\odot$ that is normally associated with the HAeBe regime. As discussed above, the first bin in the figure is smaller than expected mainly because of the lack of IMTTs. In turn, the last bin is larger than expected because the stars with $M_* > 12\ M_\odot$ were all grouped together.

New searches based on machine-learning algorithms and making use of *Gaia* data (e.g., Vioque et al. 2020) will give much more complete sets of stars that are even better accommodated to the IMF and provide volume-limited samples that reflect more physically realistic fractions of HBes versus HAes. Still, the statistical results presented in the following sections are based on a sample of HAeBes that is representative in the sense that it roughly follows the IMF in the mass range ~2–12 $M_\odot$.

[12] All inferred IMFs have virtually the same shape for the stellar mass range we analyzed.

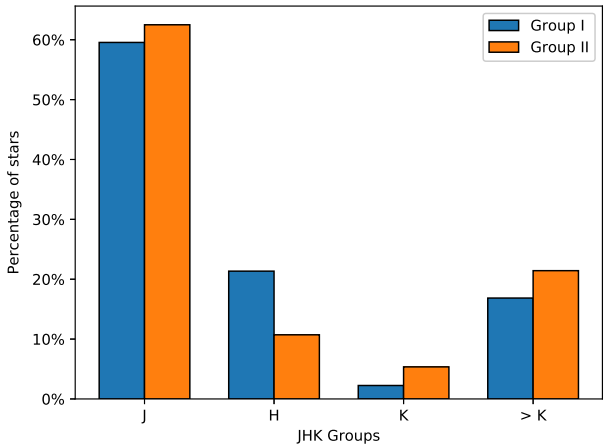

Fig. 4. Histogram comparing the distributions of the *JHK* groups (based on the wavelength at which the infrared excess starts) and M01 groups (based on the shape of the SEDs), as indicated in the *x*-axis and the legend.

3.2. M01 and JHK SED classifications

Figure 4 shows the distribution of the stars according to the M01 and *JHK* SED classification schemes. No trend is apparent, and the SED shape according to the M01 scheme is not related to the wavelength at which the IR excess departs from the photosphere. A two-sample Kolmogorov-Smirnov (K-S) test rejects the null hypothesis that both samples are drawn from the same parent distributions at a 1% significance level. Group I sources were associated to the presence of imaged dust gaps and cavities (see references in the introduction), but these are difficult to trace based on the SEDs alone. In turn, GRAVITY Collaboration (2019) hypothesized that group I sources may also have larger inner disk sizes than group II, although no definitive trend based on interferometric data was found in that work. Our result above does not support the hypothesis that the M01 group I stars also tend to be group *K* and group >*K* sources, whose inner dust holes are comparatively larger than for the stars in groups *J* and *H*. Moreover, the larger number of group I stars compared to group II sources (89 vs. 56; the 21 remaining objects have a doubtful or unknown classification) sharply contrasts with the smaller fraction of transitional disks compared to full disks in the lower-mass regime, which roughly ranges between 20% and 50% depending on the age (Currie & Sicilia-Aguilar 2011). However, given that IMTTs are not well probed in the sample (Sect. 3.1) and they are the precursors of HAes (thus in principle hosting less evolved disks), the currently observed proportion of sources in groups *J* and *H* is potentially underestimated. In turn, if group II stars probe disks without holes, the inclusion of additional IMTTs in the sample would potentially increase the observed proportion of group II sources.

The *JHK* classification can be roughly translated into the "full" and "transitional" disk nomenclature similar to that used in the lower-mass regime. We considered that HAeBes have "full disks" if their IR excess starts at the *J* or *H* bands (group *J* and group *H* stars), while HAeBes with "transitional" disks show IR excess only at longer wavelengths (group *K* and group >*K* stars). We note that although the definition of transitional disk in TTs is usually based on an IR excess starting at wavelengths (~10 μm) longer than adopted here (*K* band), the size of the associated inner disk holes are roughly the same because HAeBes are hotter (see Sect. 2.2.4 and the discussion in Mendigutía et al. 2012). In this respect, the two definitions are therefore physically

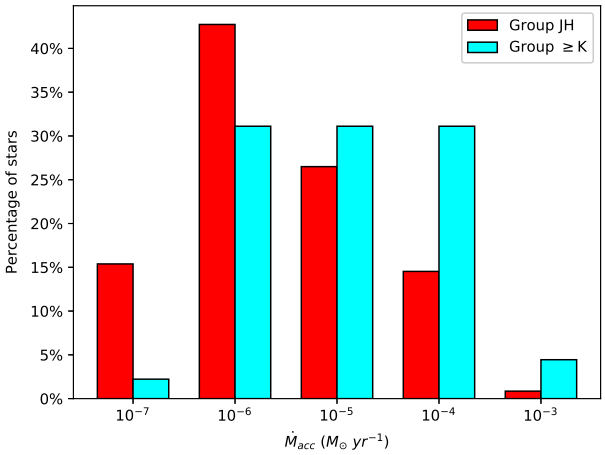

Fig. 5. Histogram comparing the distributions of mass accretion rates and *JHK* groups, as indicated in the *x*-axis and the legend.

equivalent. However, our definition of a transitional disk for HAeBes does not consider the stars that have relatively weak emission at short, IR wavelengths (sometimes called "pretransitional" disks), but only the sources that are completely devoid of dust in their cavities according to their SEDs. Under the previous definitions and caveats, we found that 121 HAeBes have full disks and only 46 can be considered transitionals. This represents ∼28% of HAeBes, which is significantly smaller than the fraction of Class I HAeBes, but more similar to the fraction of transitional disks in TTs. We repeat that the inclusion of additional IMTTs in the sample would in principle decrease the fraction of transitional disks compared to what is currently observed.

On the other hand, our empirically based accretion rates do not show any apparent relation with the M01 groups, supporting previous claims in this respect (Mendigutía et al. 2012). Moreover, our data also support previous findings indicating that group II sources tend to have larger dust grains than group I (Acke et al. 2004), and that the former tend to show UXOr-like variability as well (Dullemond et al. 2003). Concerning the two latter statements, the typical dust opacity index β reflecting the submillimeter and millimeter dust grain size (Sect. 2.2.3 and Table B.3) changes from ∼1.15 (group I) to ∼0.72 (group II), and the sources classified as UXOrs in Vioque et al. (2018) mostly belong to group II (∼78 %, vs. ∼22 % in group I).

3.3. Accretion rates and JHK SED classification

Figure 5 shows the distributions of the stars according to their $\dot{M}_{\rm acc}$ values and the *JHK* SED classification scheme. HAeBes belonging to group ≥*K* tend to show higher accretion rates, which is confirmed by a K-S test. This result disagree with a previous similar analysis in Mendigutía et al. (2012). The opposite result was found in that work, where HAeBes belonging to the *JH* group tend to be the strongest accretors. However, the sample analyzed in Mendigutía et al. (2012) was comparatively smaller and mainly dominated by HAes, whereas our current result is driven mainly by the HBes in our sample, as we show below.

3.4. Stellar parameters and JHK SED classifications

Figure 6 shows three histograms representing the percentage of HAeBes classified in *JHK* groups as a function of the stellar luminosity, mass, and age. Two-sample K–S tests indicate

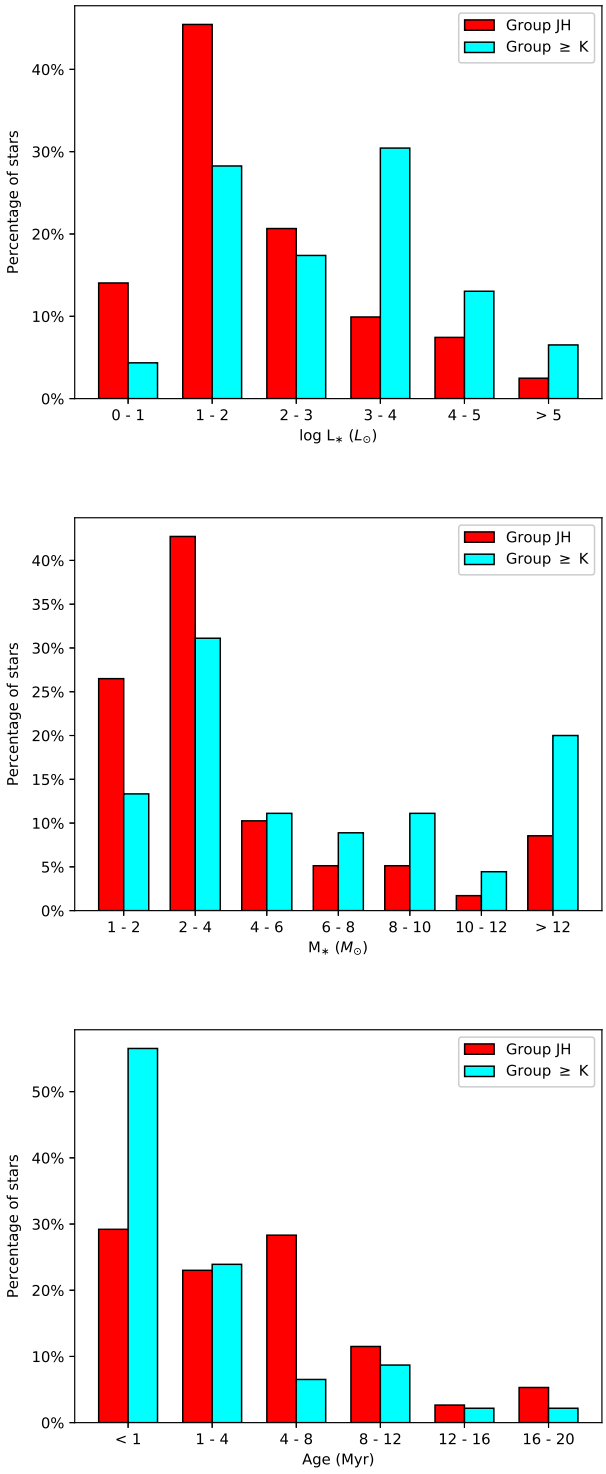

Fig. 6. Histogram comparing the distributions of stellar parameters (luminosity, stellar mass, and age) and *JHK* groups, as indicated in the *x*-axis and the legend.

that there are low probabilities that *JH* and ≥*K* groups are drawn from the same parent distribution when these groups are related to the stellar parameters. Group ≥*K* HAeBes are typically younger, brighter, and more massive than group *JH* HAeBes, which mainly corresponds to the early-type HBes in our sample. A similar analysis does not reveal any trend relating the M01 groups and the stellar parameters. In turn, the *JHK* groups are associated with the size of the inner dust holes (see Sect. 2.2.4

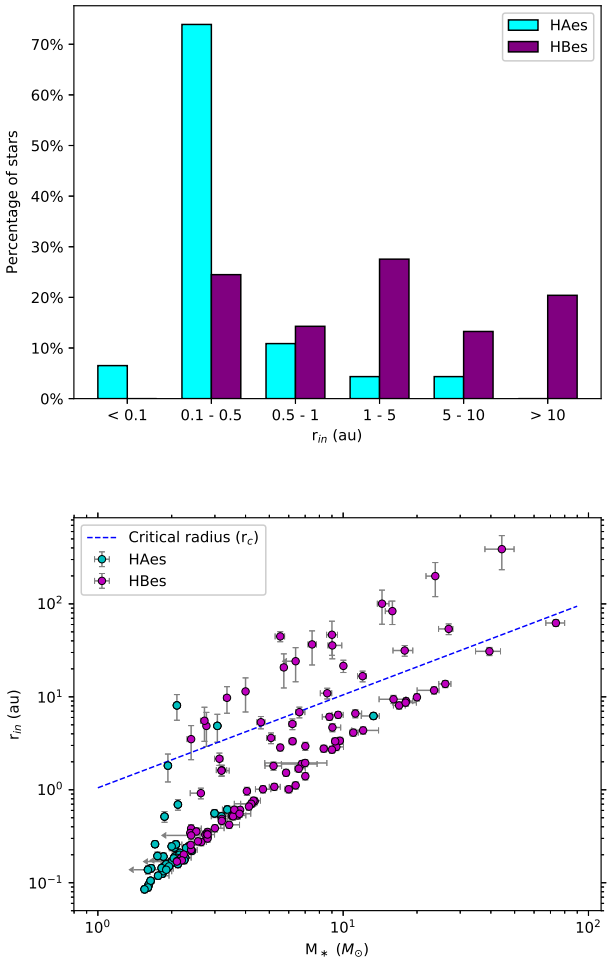

Fig. 7. *Top panel:* histogram comparing the distributions of sizes of the inner disk holes for HAes and HBes, as indicated in the x-axis and the legend. *Bottom panel:* inner disk holes as a function of the stellar mass for HAes and HBes. The dashed blue line represents the critical radius above which the stars are consistent with the photoevaporation scenario (see text). Upper limits are indicated by arrows.

and below). The top panel of Fig. 7 shows the distributions of r_{in} for HAes and HBes separately. HBes tend to have larger inner disk holes than HAes, which is confirmed by a K-S test. This is better seen in the bottom panel of Fig. 7, where r_{in} is plotted against the stellar mass considering both subsamples. Associating groups K and $>K$ sources again to "transitional" disks, we found that ∼34% of the HBes in our sample have such disks, which is significantly higher than the ∼15% ratio found for the HAes. If less evolved IMTTs were well probed in the sample (Sect. 3.1), the difference between the fraction of transitional disks in HBes and lower-mass stars would in principle be even larger.

3.5. Inner disk holes and associated physical processes

The inner disk holes associated with excesses starting at relatively long wavelengths can be explained mainly by four different processes (see, e.g., Espaillat et al. 2014, and references therein): viscous evolution, substantial grain growth causing a depletion of the small dust particles in the inner regions, companions that sweep the material in their orbits, and/or photoevaporation. Viscous evolution alone is not expected to produce a preferential depletion of dust at small radii, especially considering that HBes are typically young (≤1 Myr; see below) and the timescales involved would be too short. The dust opacity index β indicates that although disks around HAeBes show grain growth compared to the interstellar medium, the median value is roughly the same in group JH as in group $\geq K$ (1.2 and 1.1, respectively). Our data therefore contain no evidence to support the idea that dust grain growth in HBes with IR excesses starting at long wavelengths is different from that in the rest of the stars. Similarly, the fraction of HAeBes in group JH with stellar companions (as tabulated in Vioque et al. 2018) is larger than the same fraction in group $\geq K$ (∼33% vs. ∼22%), which contradicts the hypothesis that these companions causing larger inner disk holes in the second group. Still, a population of (undetected) substellar companions and planets might explain the presence of inner disk holes. However, the previous arguments and the available data leave photoevaporation as the most plausible mechanism that dominates the formation of inner holes in many HBes.

In the photoevaporation scenario (see, e.g., Alexander et al. 2014, and references therein) UV and/or X-ray photons cause photoevaporative winds limiting the resupply of inner disk material from accretion flows and producing a relatively fast inside-out disk dispersal. HBes have associated intrinsically high UV luminosities and excesses (e.g., Fairlamb et al. 2015), and wind signatures in their spectra are significantly stronger than for HAes (e.g., Mendigutía et al. 2011a). The fact that HBes show lower IR excess, disk masses, and accretion rates than expected from the trend followed by TTs and HAes (Alonso-Albi et al. 2009; Vioque et al. 2018; W2020) also supports photoevaporation as the main mechanism that drives the dissipation of their disks (see also Fuente et al. 1998; Mendigutía et al. 2012), although strong uncertainties are still involved in the determination of disk masses and accretion rates in HBes (Sects. 2.2.2 and 2.2.3). Two additional lines of evidence based on comparatively better known SEDs and stellar parameters are provided here to support photoevaporation as the dominant disk dissipation mechanism in HBes.

On the one hand, the bottom panel of Fig. 7 overplots the critical radius (dashed line) representing the distance from the star from which a gap opens due to photoevaporation, $r_c \sim 1.05(M_*/M_\odot)$ for a typical temperature of the UV/X-ray heated gas $\sim 10^4$ K (Gorti et al. 2009). Although the majority of HAeBes show inner disk holes below the critical radius in agreement with interferometric measurements (GRAVITY Collaboration 2019), the inferred inner holes for more than 60% of HBes with transitional disks (i.e., groups K and $>K$) are equal to or above this limit. This proportion is significantly smaller for transitional HAes (30%). On the other hand, Fig. 8 shows the stellar ages and masses of the HAeBes. The expected disk lifetime assuming photoevaporation as the main mechanism driving disk dissipation from the model by Gorti et al. (2009, see their Fig. 12) is overplotted. Almost all HAes are older than the photoevaporative lifetime. However, the trend is the opposite for the HBes because most of these sources are younger and do not survive for timescales longer than expected from photoevaporation. These two previous results indicate that while photoevaporation cannot be the main disk dissipation mechanism for most HAes, the inferred inner disk holes and ages of most HBes are consistent with this scenario.

4. Conclusions

We presented the largest database of stellar and circumstellar parameters that are uniformly derived from an SED analysis

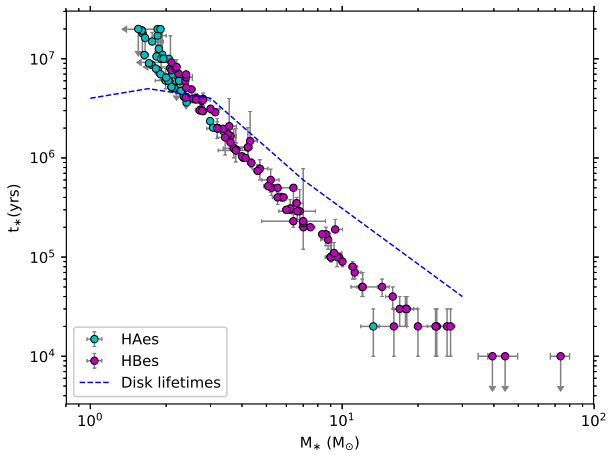

Fig. 8. Stellar age vs. stellar mass for HAes and HBes. The dashed blue line represents the disk lifetime below which the stars are consistent with the photoevaporation scenario (see text). Upper limits are indicated by arrows.

for 209 HAeBes. Stellar temperatures and spectral types, luminosities, radii, masses, and ages, as well as SED shape classifications, accretion rates, disk masses, and sizes of dust inner holes have been homogeneously derived based on multiwavelength photometry and *Gaia* EDR3 distances. This database is stored in an online archive of HAeBes[13] and constitutes a unique tool for the study of this type of sources based on the most recent information available for them.

This sample reproduces the IMF, with the exception of the lower- and higher- mass ends that belong to the IMTT and MYSO limits, respectively. In this sense, the stars characterized in this work represents the HAeBe regime within the stellar mass range $2 < M_*/M_\odot < 12$ well, but when the associated data are used for statistical purposes, the lack of sources in the boundaries, especially IMTTS, must be taken into account. A statistical analysis was carried out in order to exemplify the potential use of these data. We derived the following two main conclusions:

– The distributions of the SEDs according to the M01 groups and the wavelength at which the IR excess starts (*JHK*) are not related to each other, implying that they reflect different properties. In particular, our more complete dataset confirms previous claims suggesting that the M01 groups are not connected to accretion rates but to dust grain growth or the UXOr-type variability. However, when the presence of inner dust disk holes is inferred from the *JHK* classification, no statistical evidence supports a relation between M01 group I sources and stars with transitional disks (defined here as those with IR excesses starting at wavelengths ≥2.16 µm).
– In turn, we found that relatively wide inner dust disk holes inferred from SEDs are present in ∼28% of HAeBes, similar to the fraction of transitional disks in TTs, and are about twice as frequent in early-type HBes than in HAes. The relatively small inner disk holes and old ages inferred for most transitional HAes cannot be explained from photoevaporation. In contrast, the inner holes and ages of most transitional HBes are compatible with the critical radii and lifetimes predicted by this scenario. This evidence supports photoevaporation as the main process driving disk dissipation in HBes, although we do not rule out other potential mechanism.

[13] http://svo2.cab.inta-csic.es/projects/harchibe/

Finally, our results show the potential use of SED analysis with VOSA for characterizing the stellar and circumstellar properties of newly discovered HAeBe candidates (see Appendix A). In particular, Vioque et al. (2020) have published a new catalog with thousands of these objects, and methods complementary to spectroscopy could be of great help to study this large number of new stars that might belong to the HAeBe regime.

Acknowledgements. JGD, IM and PMA acknowledge the Government of Comunidad Autónoma de Madrid (Spain) for funding this research through a 'Talento' Fellowship (2016-T1/TIC-1890 PI I. Mendigutía). The research of IM, JGD, BM and GM is also partially funded by the Spanish "Ministerio de Ciencia, Innovación y Universidades" through the national project "On the Rocks II" (PGC2018-101950-B-100; PI E. Villaver). MV acknowledges the STARRY project, which has received funding from the European Union's Horizon 2020 research and innovation programme under MSCA ITN-EID grant agreement No 676036. This publication makes use of VOSA, developed under the Spanish Virtual Observatory project supported by the Spanish MINECO through grant AyA2017-84089. VOSA has been partially updated by using funding from the European Union's Horizon 2020 Research and Innovation Programme, under Grant Agreement n° 776403 (EXOPLANETS-A). This work has made use of data from the European Space Agency (ESA) mission *Gaia* (https://www.cosmos.esa.int/gaia), processed by the *Gaia* Data Processing and Analysis Consortium (DPAC, https://www.cosmos.esa.int/web/gaia/dpac/consortium). Funding for the DPAC has been provided by national institutions, in particular the institutions participating in the *Gaia* Multilateral Agreement. The authors also acknowledge the referee for her/his useful comments, which have served to improve the original manuscript.

References

Acke, B., & van den Ancker, M. E. 2004, A&A, 426, 151
Acke, B., & van den Ancker, M. E. 2006, A&A, 457, 171
Acke, B., van den Ancker, M. E., Dullemond, C. P., van Boekel, R., & Waters, L. B. F. M. 2004, A&A, 422, 621
Acke, B., van den Ancker, M. E., & Dullemond, C. P. 2005, A&A, 436, 209
Acke, B., Bouwman, J., Juhász, A., et al. 2010, ApJ, 718, 558
Alexander, R., Pascucci, I., Andrews, S., Armitage, P., & Cieza, L. 2014, in Protostars and Planets VI, eds. H. Beuther, R. S. Klessen, C. P. Dullemond, & T. Henning, 475
Alfonso-Garzón, J., Domingo, A., Mas-Hesse, J. M., & Giménez, A. 2012, A&A, 548, A79
Alonso-Albi, T., Fuente, A., Bachiller, R., et al. 2009, A&A, 497, 117
Andre, P., Ward-Thompson, D., & Barsony, M. 1993, ApJ, 406, 122
Andrews, S. M., & Williams, J. P. 2007, ApJ, 671, 1800
Armitage, P. J. 2009, Astrophysics of Planet Formation (Cambridge, UK: Cambridge University Press)
Arun, R., Mathew, B., Manoj, P., et al. 2019, ApJ, 157, 159
Bailer-Jones, C. A. L., Rybizki, J., Fouesneau, M., Demleitner, M., & Andrae, R. 2021, AJ, 161, 147
Ballering, N. P., & Eisner, J. A. 2019, AJ, 157, 144
Barenfeld, S. A., Carpenter, J. M., Ricci, L., & Isella, A. 2016, VizieR Online Data Catalog: J/ApJ/827/142
Bayo, A., Rodrigo, C., Barrado Y Navascués, D., et al. 2008, A&A, 492, 277
Beckwith, S. V. W., Sargent, A. I., Chini, R. S., & Guesten, R. 1990, AJ, 99, 924
Beichman, C. A., Neugebauer, G., Habing, H. J., Clegg P. E., & Chester T. J. 1988, Infrared Astronomical Satellite (IRAS) Catalogs and Atlases 1, 1
Bianchi, L., & GALEX Team. 2000, Mem. Soc. Astron. It., 71, 1123
Blondel, P. F. C., & Djie, H. R. E. T. A. 2006, A&A, 456, 1045
Boissier, J., Alonso-Albi, T., Fuente, A., et al. 2011, A&A, 531, A50
Bressan, A., Marigo, P., Girardi, L., et al. 2012, MNRAS, 427, 127
Calvet, N., Muzerolle, J., Briceño, C., et al. 2004, AJ, 128, 1294
Carmona, A., van den Ancker, M. E., Audard, M., et al. 2010, A&A, 517, A67
Castelli, F., Gratton, R. G., & Kurucz, R. L. 1997, A&A, 318, 841
Chen, P. S., Shan, H. G., & Zhang, P. 2016, New Astron., 44, 1
Cotten, T. H., & Song, I. 2016, VizieR Online Data Catalog: J/ApJS/225/15
Currie, T., & Sicilia-Aguilar, A. 2011, ApJ, 732, 24
De Marchi, G., Panagia, N., & Beccari, G. 2017, ApJ, 846, 110
Di Francesco, J., Johnstone, D., Kirk, H., MacKenzie, T., & Ledwosinska, E. 2008, ApJS, 175, 277
Dong, R., Najita, J. R., & Brittain, S. 2018, ApJ, 862, 103
Dullemond, C. P. 2002, A&A, 395, 853
Dullemond, C. P., & Dominik, C. 2004, A&A, 417, 159
Dullemond, C. P., van den Ancker, M. E., Acke, B., & van Boekel, R. 2003, ApJ, 594, L47

Eisner, J. A., Lane, B. F., Akeson, R. L., Hillenbrand , L. A., & Sargent, A. I. 2003, ApJ, 588, 360
Eisner, J. A., Lane, B. F., Hillenbrand, L. A., Akeson, R. L., & Sargent, A. I. 2004, ApJ, 613, 1049
Enoch, M. L., Evans, Neal J., I., Sargent, A. I., et al. 2008, ApJ, 684, 1240
Espaillat, C., Muzerolle, J., Najita, J., et al. 2014, in Protostars and Planets VI, eds. H. Beuther, R. S. Klessen, C. P. Dullemond, & T. Henning, 497
Evans, D. W., Irwin, M. J., & Helmer, L. 2002, A&A, 395, 347
Evans, Neal J., I., Dunham, M. M., Jørgensen, J. K., et al. 2009, ApJS, 181, 321
Fabricius, C., Luri, X., Arenou, F., et al. 2021, A&A, 649, A5
Fairlamb, J. R., Oudmaijer, R. D., Mendigutía, I., Ilee, J. D., & van den Ancker, M. E. 2015, MNRAS, 453, 976
Fedele, D., van den Ancker, M. E., Henning, T., Jayawardhana, R., & Oliveira, J. M. 2010, A&A, 510, A72
Finkenzeller, U., & Mundt, R. 1984, A&AS, 55, 109
Fitzpatrick, E. L. 1999, PASP, 111, 63
Fuente, A., Martin-Pintado, J., Bachiller, R., Neri, R., & Palla, F. 1998, A&A, 334, 253
Gaia Collaboration (Prusti, T., et al.) 2016, A&A, 595, A1
Gaia Collaboration (Brown, A. G. A., et al.) 2018, A&A, 616, A1
Gaia Collaboration (Brown, A. G. A., et al.) 2021, A&A, 649, A1
Garcia Lopez, R., Natta, A., Testi, L., & Habart, E. 2006, A&A, 459, 837
Garufi, A., Meeus, G., Benisty, M., et al. 2017, A&A, 603, A21
Garufi, A., Benisty, M., Pinilla, P., et al. 2018, A&A, 620, A94
Giannini, T., Lorenzetti, D., Nisini, B., et al. 1996, in The Role of Dust in the Formation of Stars, eds. H. U. Käufl, & R. Siebenmorgen, 27
Ginsburg, A., Glenn, J., Rosolowsky, E., et al. 2013, ApJS, 208, 14
Gorti, U., Dullemond, C. P., & Hollenbach, D. 2009, ApJ, 705, 1237
Grady, C. A., Schneider, G., Hamaguchi, K., et al. 2007, ApJ, 665, 1391
GRAVITY Collaboration, (Perraut, K., et al.) 2019, A&A, 632, A53
Guedel, M., Benz, A. O., Catala, C., & Praderie, F. 1989, A&A, 217, L9
Hartmann, L., Calvet, N., Gullbring, E., & D'Alessio, P. 1998, ApJ, 495, 385
Helou, G., & Walker, D. W. 1988, Infrared astronomical satellite (IRAS) catalogs ans atlases, 7, 1
Henning, T., Pfau, W., Zinnecker, H., & Prusti, T. 1993, A&A, 276, 129
Henning, T., Launhardt, R., Steinacker, J., & Thamm, E. 1994a, ASP Conf. Ser., 62, 171
Henning, T., Launhardt, R., Steinacker, J., & Thamm, E. 1994b, A&A, 291, 546
Herbig, G. H. 1960, ApJS, 4, 337
Herbig, G. H., & Bell, K. R. 1988, Third Catalog of Emission-Line Stars of the Orion Population, 3, 1988
Hillenbrand, L. A., Strom, S. E., Vrba, F. J., & Keene, J. 1992, ApJ, 397, 613
Honda, M., Maaskant, K., Okamoto, Y. K., et al. 2015, ApJ, 804, 143
Indebetouw, R., Mathis, J. S., Babler, B. L., et al. 2005, ApJ, 619, 931
Ishihara, D., Onaka, T., Kataza, H., et al. 2010, A&A, 514, A1
Jiménez-Donaire, M. J., Meeus, G., Karska, A., et al. 2017, A&A, 605, A62
Kama, M., Folsom, C. P., & Pinilla, P. 2015, A&A, 582, A10
Kauffmann, J., Bertoldi, F., Bourke, T. L., Evans, N. J., I., & Lee, C. W. 2008, VizieR Online Data Catalog: J/A+A/487/993
Kawada, M., Baba, H., Barthel, P. D., et al. 2007, PASJ, 59, S389
Kenyon, S. J., & Hartmann, L. 1995, ApJS, 101, 117
Kraus, S., Kreplin, A., Fukugawa, M., et al. 2017, ApJ, 848, L11
Kun, M., Balog, Z., Kenyon, S. J., Mamajek, E. E., & Gutermuth, R. A. 2009, ApJS, 185, 451
Lindegren, L., Hernández, J., Bombrun, A., et al. 2018, A&A, 616, A2
Lindegren, L., Klioner, S. A., Hernández, J., et al. 2021, A&A, 649, A2
Maaskant, K. M., Honda, M., Waters, L. B. F. M., et al. 2013, A&A, 555, A64
Mairs, S., Johnstone, D., Kirk, H., et al. 2016, MNRAS, 461, 4022
Mannings, V. 1994, MNRAS, 271, 587
Mannings, V., & Sargent, A. I. 1997, ApJ, 490, 792
Mannings, V., & Sargent, A. I. 2000, ApJ, 529, 391
Meeus, G., Waters, L. B. F. M., Bouwman, J., et al. 2001, A&A, 365, 476
Meeus, G., Pinte, C., Woitke, P., et al. 2010, A&A, 518, A124
Meeus, G., Montesinos, B., Mendigutía, I., et al. 2012, A&A, 544, A78
Meijer, J., Dominik, C., de Koter, A., et al. 2008, A&A, 492, 451
Mendigutía, I. 2020, Galaxies, 8, 39
Mendigutía, I., Calvet, N., Montesinos, B., et al. 2011a, A&A, 535, A99
Mendigutía, I., Eiroa, C., Montesinos, B., et al. 2011b, A&A, 529, A34
Mendigutía, I., Mora, A., Montesinos, B., et al. 2012, A&A, 543, A59
Mendigutía, I., Oudmaijer, R. D., Rigliaco, E., et al. 2015, MNRAS, 452, 2837
Monnier, J. D., & Millan-Gabet, R. 2002, ApJ, 579, 694
Monnier, J. D., Millan-Gabet, R., Billmeier, R., et al. 2005, ApJ, 624, 832
Montesinos, B., Eiroa, C., Mora, A., & Merín, B. 2009, A&A, 495, 901
Natta, A., Grinin, V. P., Mannings, V., & Ungerechts, H. 1997, ApJ, 491, 885
Natta, A., Grinin, V., & Mannings, V. 2000, in Protostars and Planets IV, eds. V. Mannings, A. P. Boss, & S. S. Russell, 559
Paunzen, E. 2015, A&A, 580, A23
Péricaud, J., Di Folco, E., Dutrey, A., Guilloteau, S., & Piétu, V. 2017, A&A, 600, A62
Pezzuto, S., Strafella, F., & Lorenzetti, D. 1997, ApJ, 485, 290
Piétu, V., Dutrey, A., & Kahane, C. 2003, A&A, 398, 565
Piétu, V., Dutrey, A., Guilloteau, S., Chapillon, E., & Pety, J. 2006, A&A, 460, L43
Planck Collaboration 2013, VizieR Online Data Catalog: VIII/91
Planck Collaboration Int. LIV. 2018, VizieR Online Data Catalog: J/A+A/619/A94
Reed, B. C. 2003, AJ, 125, 2531
Reipurth, B., Chini, R., Krugel, E., Kreysa, E., & Sievers, A. 1993, A&A, 273, 221
Ribas, A., Espaillat, C. C., Macias, E., et al. 2018, VizieR Online Data Catalog, J/ApJ/849/63
Riello, M., De Angeli, F., Evans, D. W., et al. 2018, A&A, 616, A3
Riello, M., De Angeli, F., Evans, D. W., et al. 2021, A&A, 649, A3
Robitaille, T. P., Whitney, B. A., Indebetouw, R., Wood, K., & Denzmore, P. 2006, ApJS, 167, 256
Rybizki, J., Green, G., Rix, H.-W., et al. 2021, ArXiv e-prints [arXiv:2101.11641]
Salpeter, E. E. 1955, ApJ, 121, 161
Sandell, G. 2000, A&A, 358, 242
Sandell, G., Weintraub, D. A., & Hamidouche, M. 2011, ApJ, 727, 26
Sheret, I., Dent, W. R. F., & Wyatt, M. C. 2004, MNRAS, 348, 1282
Sicilia-Aguilar, A., Henning, T., & Hartmann, L. W. 2010, ApJ, 710, 597
Skrutskie, M. F., Cutri, R. M., Stiening, R., et al. 2006, AJ, 131, 1163
Strom, K. M., Strom, S. E., Edwards, S., Cabrit, S., & Skrutskie, M. F. 1989, AJ, 97, 1451
Sylvester, R. J., Skinner, C. J., Barlow, M. J., & Mannings, V. 1996, MNRAS, 279, 915
Sylvester, R. J., Dunkin, S. K., & Barlow, M. J. 2001, MNRAS, 327, 133
Tayler, R. J. 1994, The Stars, Their Structure and Evolution
The, P. S., de Winter, D., & Perez, M. R. 1994, A&AS, 104, 315
Urquhart, J. S., Moore, T. J. T., Csengeri, T., et al. 2014, VizieR Online Data Catalog: J/MNRAS/443/1555
van Boekel, R., Waters, L. B. F. M., Dominik, C., et al. 2003, A&A, 400, L21
van Boekel, R., Min, M., Waters, L. B. F. M., et al. 2005, A&A, 437, 189
Verhoeff, A. P., Waters, L. B. F. M., van den Ancker, M. E., et al. 2012, A&A, 538, A101
Vieira, S. L. A., Corradi, W. J. B., Alencar, S. H. P., et al. 2003, AJ, 126, 2971
Vioque, M., Oudmaijer, R. D., Baines, D., Mendigutía, I., & Pérez-Martínez, R. 2018, A&A, 620, A128
Vioque, M., Oudmaijer, R. D., Schreiner, M., et al. 2020, A&A, 638, A21
Wichittanakom, C., Oudmaijer, R. D., Fairlamb, J. R., et al. 2020, MNRAS, 493, 234
Wright, E. L., Eisenhardt, P. R. M., Mainzer, A. K., et al. 2010, AJ, 140, 1868
Zacharias, N., Finch, C. T., Girard, T. M., et al. 2012, VizieR Online Data Catalog, 1322
Zhu, Z., Zhang, S., Jiang, Y.-F., et al. 2019, ApJ, 877, L18

Appendix A: Comparison with previous stellar parameters

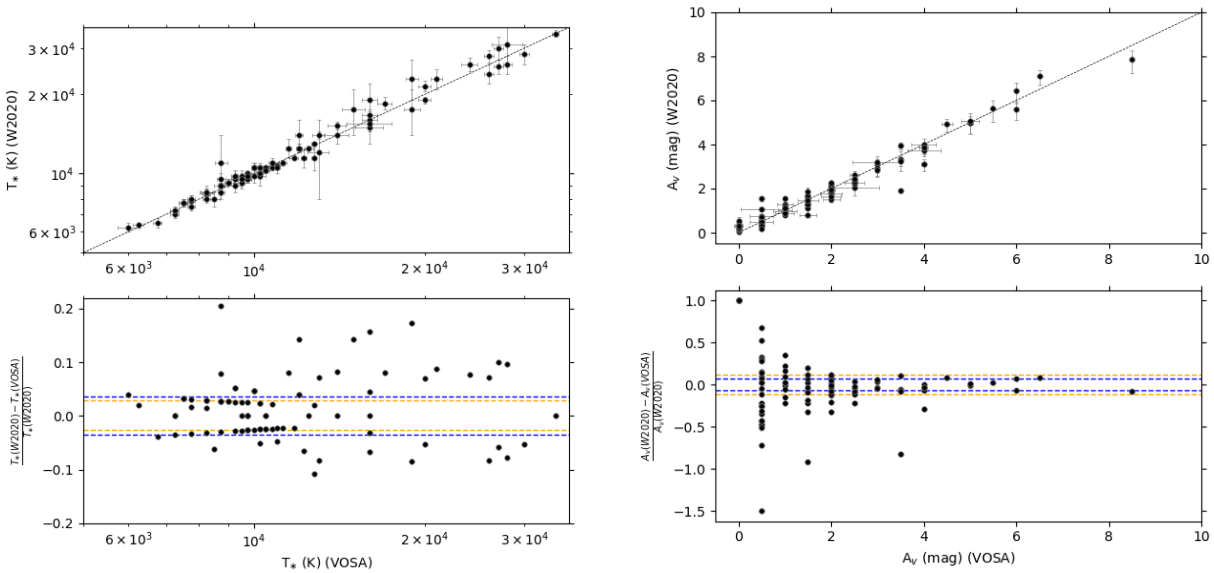

Fig. A.1. *Top*: comparison between T_* and A_V estimated from VOSA and from W2020. The dashed black line indicates equal values. *Bottom*: relative errors resulting from the comparison of the corresponding values from VOSA and W2020. The orange line indicates the typical median relative (±) error of this comparison. The median relative (±) error provided in W2020 is also plotted with the blue lines for reference.

In this appendix the stellar parameters (T_*, L_*, R_*, M_*, and t_*) and extinction (A_V) derived from SED fitting with VOSA are compared with the corresponding values estimated by W2020 for the 93 stars included in both samples. The T_* values were inferred in W2020 from spectral typing in the optical, and the A_V values directly resulted from the comparison of the corresponding Kurucz synthetic models with optical photometry. In our case, the extinction was set virtually free ($0 < A_V < 10$) and the temperature range of the Kurucz fitting models was fixed by the error bars ΔT_* provided in W2020 for each star (Sect. 2.1). Figure A.1 compares the T_* and A_V values obtained in both works. The bottom panels show that the typical (median) relative error from the comparison between the SED-based T_* values and those spectroscopically determined collapses to ±3% from the typical (median) relative errors of ±4% reported in W2020. The difference between the T_* values from VOSA and from W2020 increases for $T_* > 10\,000$ K because of the comparatively larger error bars reported in W2020 for hotter stars. Concerning the optical extinction, the typical (median) relative error is ±12%. For reference, the corresponding median error reported in W2020 is ±7%.

The remaining stellar parameters determined in this work and in W2020 depend on the assumed distances to the sources. Figure A.2 shows the distances used in W2020, based on *Gaia* DR2, versus the distances used in this work, based on *Gaia* EDR3. Using the code indicated in the legend of that figure, we find a good agreement within the error bars between *Gaia* DR2 and EDR3 for most stars with high-quality parallaxes in both releases. The uncertainties in EDR3 are smaller than in DR2. However, one of these sources (PDS 241) has a current *Gaia* EDR3 distance, ~5000 pc, that almost doubles the previous *Gaia* DR2 distance. The reason for this discrepancy is the use of Bayesian inference under different priors to derive the distances (see Vioque et al. 2018, and Sect. 2 for details). A few stars are classified with low-quality parallaxes

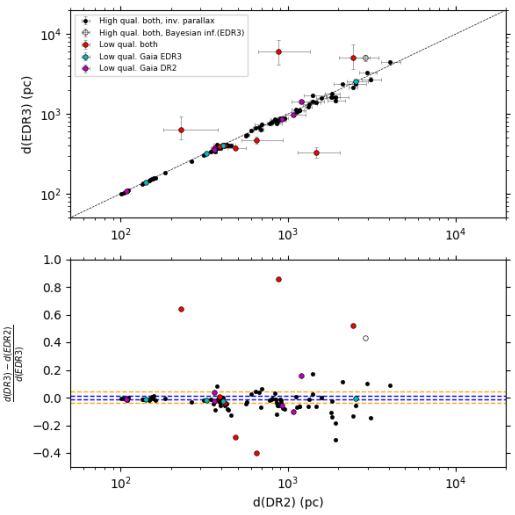

Fig. A.2. *Top*: comparison of *Gaia* DR2 and *Gaia* EDR3 distances. Black, red, cyan, and purple circles correspond to objects that have high-quality parallaxes in both releases, low quality in both releases, low quality in *Gaia* EDR3, and low quality in *Gaia* DR2, respectively. In addition, objects with high quality in both releases whose EDR3 distances have been estimated using the inverse of parallax (filled black circles) or Bayesian inference (open black circles) are indicated (note that all DR2 distances were estimated using Bayesian inference; Vioque et al. 2018). *Bottom*: relative errors resulting from the comparison of *Gaia* DR2 and *Gaia* EDR3 distances. The orange line indicates the typical median relative (±) error of such a comparison. The median relative (±) error in *Gaia* EDR3 distances is also plotted with the blue lines for reference. The relative error of VY Mon is <−1 and is not plotted for clarity.

in DR2 or in EDR3 whose corresponding distances show a reasonable agreement as well. This is probably indicative of the conservative approaches used to make such classifications.

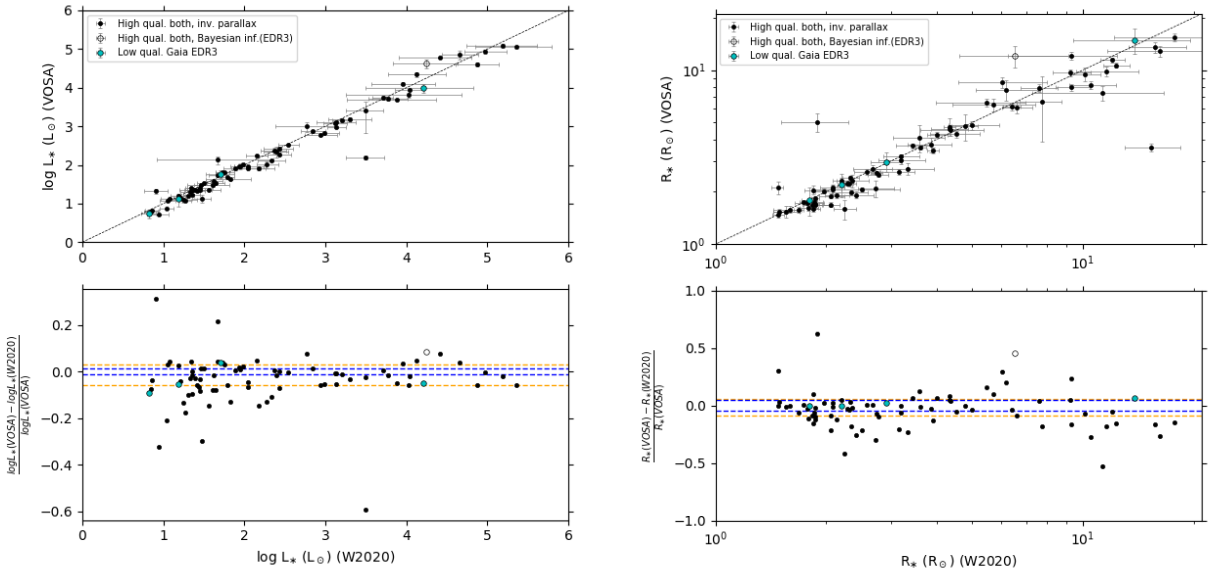

Fig. A.3. *Top:* comparison of L_* and R_* estimated from VOSA and from W2020. The dashed black line indicates equal values. *Bottom*: relative errors resulting from the comparison of the corresponding values from VOSA and W2020. The orange line indicates the typical median relative (±) error of such a comparison. The median relative (±) error estimated in VOSA is also plotted with the blue lines for reference. The relative error of HD 250550 in R_* is <−1 and is not plotted for clarity.

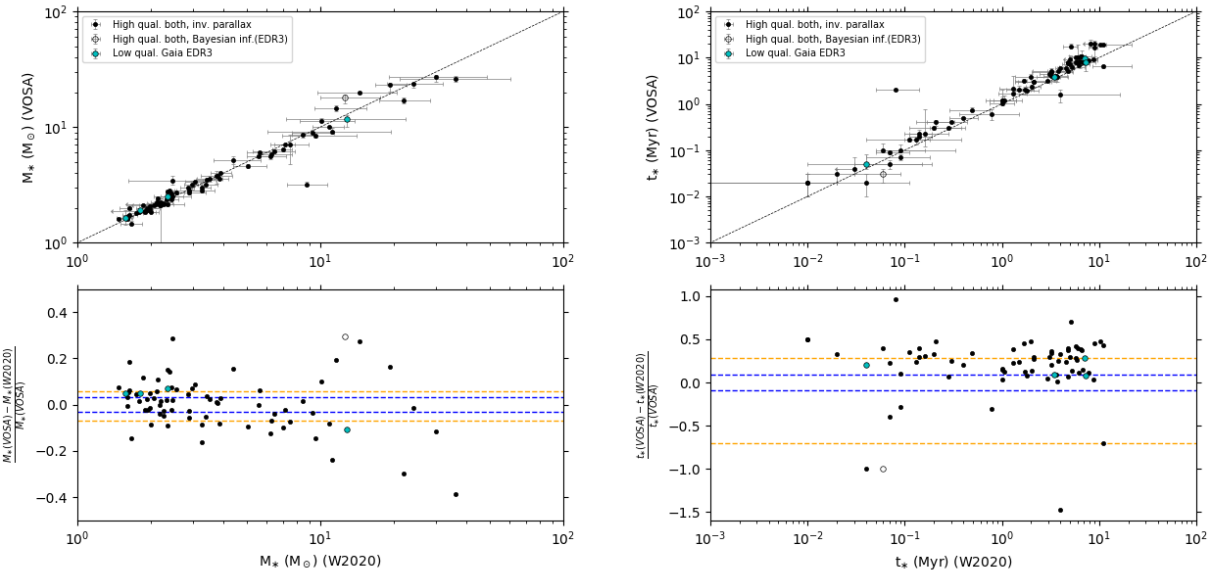

Fig. A.4. *Top*: comparison of M_* and R_* estimated from VOSA and from W2020. The dashed black line indicates equal values. *Bottom*: relative errors resulting from the comparison of the corresponding values from VOSA and W2020. The orange line indicates the typical median relative (±) error of such a comparison. The median relative (±) error estimated in VOSA is also plotted with the blue lines for reference. The relative error of HD 250550 in M_* is <−0.5 and is not plotted for clarity.

Still, the most significant differences are found for the stars with low-quality parallaxes both in *Gaia* DR2 and in EDR3, indicating that the distances to these sources are basically unknown.

The remaining figures compare the stellar parameters in W2020 and in this work that are distance dependent, using the same code as in Fig. A.2, stellar luminosities and radii in Fig. A.3, and stellar masses and ages in Fig. A.4. We note that the previous parameters were not determined by W2020 for the stars with low-quality parallaxes in *Gaia* DR2 (red and purple circles in Fig. A.2), and thus they are not included in the analysis. For the remaining stars, the typical (median) relative errors resulting from the comparison are $^{+3}_{-6}$%, $^{+6}_{-9}$%, $^{+6}_{-7}$%, and $^{+28}_{-70}$% for L_*, R_*, M_*, and t_*, respectively. For reference, the corresponding median errors obtained here and based on *Gaia* EDR3 are ±1%, ±5%, ±3%, and ±9%.

Second, *Gaia* allows us to identify thousands of new HAeBe candidates (Vioque et al. 2020) that will need to be characterized in the future. Although an analysis of optical spectra is the best way for a proper stellar characterization, SED fitting with VOSA could be a complementary tool for specific subsamples of stars. Photometry of many candidates is available, which facilitates an SED analysis in a comparatively faster and cheaper way in terms of observational and data reduction time. In turn, a priori information on the stellar temperatures of the candidates is in principle very rough, and some independent knowledge

of extinction could be available toward several star-forming regions. The previous comparisons were therefore carried out again assuming that we have very uncertain preliminary information on T_* and A_V. In particular, the VOSA models were run within a range of T_* and A_V given by the corresponding values listed in W2020 ∼±30% and ±50% of these values, simulating the large uncertainties that will in principle be associated with most HAeBe candidates. Because L_*, R_*, M_*, and t_* are distance dependent and W2020 worked with *Gaia* DR2 data, these parameters were derived again using VOSA and the same *Gaia* DR2 distances as in Vioque et al. (2018) and W2020, allowing a direct comparison. As a result, the typical (median) relative errors are $^{+8}_{-12}$%, $^{+25}_{-20}$%, $^{+8}_{-5}$%, $^{+13}_{-6}$%, $^{+8}_{-12}$% and $^{+29}_{-13}$% for T_*, A_V, L_*, R_*, M_*, and t_*, respectively. These numbers roughly quantify the accuracy that will be obtained with VOSA in future characterizations of newly discovered HAeBe candidates, where the values in W2020 have been taken as reference.

Finally, following this second case scenario, we also tested whether there is a parameter that primarily affects the accuracy obtained in the estimation of the stellar parameters with VOSA. Specifically, we analyzed whether there is any dependence on the extinction or on the number of photometric points used in the fit. Apart from the fact that the sources with relative errors in $T_* > 20\%$ have extinctions $A_V > 1$, there is no particular trend at least for the corresponding ranges explored here. In summary, the main requirement for a reasonable stellar characterization with VOSA is a proper photometric coverage (at least five photometric points) in the optical range where HAeBes peak, the tool tending to perform slightly better for low-extincted ($A_V < 1$) sources.

Appendix B: Tables with results

Table B.1. Stellar parameters.

Object	RA (h:m:s)	Dec (d:m:s)	d (pc)	ΔT_* (K)	A_V (mag)	T_* (K)	Sp. type	R_* ($R_\odot$)	Log(L_*) ($L_\odot$)	t_* (Myr)	M_* ($M_\odot$)
HBC 1 †	00:07:02.6	+65:38:38	$5043.53^{+2276.09}_{-1565.26}$	8000-8500	5.50 ± 0.00	8000 ± 125	A5-A6	13.24 ± 5.15	$2.81^{+0.25}_{-0.65}$	$0.20^{+0.83}_{-0.10}$	$6.42^{+1.57}_{-2.63}$
MQ Cas †	00:09:37.6	+58:13:11	$745.96^{+47.66}_{-42.26}$	9500-10750	3.00 ± 0.00	10250 ± 125	B9	2.51 ± 0.16	$1.80^{+0.05}_{-0.06}$	$3.57^{+0.37}_{-0.34}$	$2.58^{+0.26}_{-0.00}$
VX Cas	00:31:30.7	+61:58:51	$524.76^{+5.58}_{-5.47}$	9750-10250	1.50 ± 0.11	10000 ± 125	B9	1.68 ± 0.10	$1.40^{+0.05}_{-0.05}$	<7.99	$2.18^{+0.02}_{-0.00}$
V594 Cas	00:43:18.3	+61:54:40	$551.16^{+4.20}_{-4.13}$	11250-11750	2.50 ± 0.21 ($2.27^{+0.18}_{-0.23}$)	11750 ± 215 (*11 500 ± 250*)	B7-B8	3.74 ± 0.37	$2.38^{+0.07}_{-0.09}$	$1.67^{+0.31}_{-0.46}$	$3.60^{+0.20}_{-0.21}$
HBC 7	00:43:25.3	+61:38:23	$2512.43^{+84.88}_{-79.51}$	16000-25000	4.50 ± 0.00	19000 ± 500	B2-B3	6.81 ± 0.48	$3.74^{+0.04}_{-0.04}$	$0.15^{+0.03}_{-0.03}$	$8.79^{+0.21}_{-0.57}$
PDS 2	01:17:43.5	−52:33:31	$399.04^{+2.69}_{-2.65}$	6500-7000	0.00 ± 0.00	6750 ± 125	F2-F3	1.77 ± 0.07	$0.77^{+0.01}_{-0.01}$	$15.04^{+2.67}_{-2.50}$	$1.46^{+0.04}_{-0.01}$
HD 9672	01:34:37.9	−15:40:35	$57.12^{+0.18}_{-0.18}$	8750-9250	0.00 ± 0.00	9000 ± 125	A1-A2	1.64 ± 0.06	$1.20^{+0.02}_{-0.02}$	$11.02^{+8.96}_{-1.15}$	$1.93^{+0.02}_{-0.03}$
HD 17081 †	02:44:07.3	−13:51:32	$118.57^{+2.80}_{-2.67}$	11500-14000	0.00 ± 0.00	12750 ± 228	B7	4.51 ± 0.28	$2.68^{+0.04}_{-0.05}$	$0.90^{+0.10}_{-0.10}$	$4.39^{+0.16}_{-0.19}$
BD+30 549	03:29:19.8	+31:24:57	$284.64^{+1.93}_{-1.90}$	10750-13000	2.00 ± 0.20	10750 ± 201	B8	1.76 ± 0.23	$1.57^{+0.10}_{-0.12}$	<6.51	$2.40^{+0.14}_{-0.00}$
PDS 4	03:39:00.6	+29:41:46	$389.04^{+3.51}_{-3.45}$	9500-10750	1.00 ± 0.00	9500 ± 125	B9-A0	1.62 ± 0.05	$1.28^{+0.01}_{-0.01}$	$9.98^{+0.53}_{-0.00}$	$2.05^{+0.03}_{-0.05}$
IP Per	03:40:47.0	+32:31:54	$287.26^{+2.53}_{-2.48}$	7500-8500	0.50 ± 0.00	7500 ± 125	A7-A9	1.57 ± 0.06	$0.85^{+0.02}_{-0.02}$	$18.06^{+1.94}_{-6.88}$	$1.61^{+0.06}_{-0.01}$
XY Per A	03:49:36.3	+38:58:55	$419.21^{+5.38}_{-5.24}$	9500-10000	2.00 ± 0.25	10000 ± 244	B9	4.80 ± 0.63	$2.32^{+0.09}_{-0.12}$	$1.25^{+0.69}_{-0.25}$	$3.71^{+0.30}_{-0.34}$
AB Aur	04:55:45.9	+30:33:04	$155.01^{+0.90}_{-0.89}$	8750-10250	0.50 ± 0.00	9000 ± 125	A1-A2	2.79 ± 0.09	$1.66^{+0.01}_{-0.01}$	$4.14^{+0.20}_{-0.13}$	$2.36^{+0.04}_{-0.05}$
HD 31648	04:58:46.3	+29:50:37	$155.22^{+1.23}_{-1.24}$	8000-8500	0.00 ± 0.00	8000 ± 125	A5-A6	2.13 ± 0.07	$1.22^{+0.01}_{-0.01}$	$7.71^{+0.23}_{-0.38}$	$1.85^{+0.04}_{-0.01}$
UX Ori †	05:04:30.0	−03:47:14	$319.83^{+2.94}_{-2.89}$	8250-8750	1.00 ± 0.26 ($0.99^{+0.04}_{-0.03}$)	8250 ± 245 (*8500 ± 250*)	A3-A6	1.79 ± 0.34	$1.12^{+0.14}_{-0.20}$	$9.84^{+0.17}_{-0.00}$	$1.91^{+0.04}_{-0.00}$
HD 34282	05:16:00.5	−09:48:35	$306.49^{+2.19}_{-2.16}$	9250-9750	0.50 ± 0.00 ($0.55^{+0.03}_{-0.02}$)	9250 ± 125 (*9500 ± 250*)	A0-A1	1.47 ± 0.05	$1.16^{+0.02}_{-0.02}$	<19.87	<1.90
HD 34700	05:19:41.4	+05:38:43	$346.77^{+2.46}_{-2.42}$	5750-6250	0.00 ± 0.00	6000 ± 125	F8-G1	4.41 ± 0.19	$1.36^{+0.01}_{-0.01}$	$2.11^{+0.76}_{-0.14}$	$2.63^{+0.17}_{-0.08}$
HD 290380	05:23:31.0	−01:04:24	$343.30^{+2.52}_{-2.48}$	6250-6500	0.00 ± 0.00	6250 ± 125	F5-F8	2.16 ± 0.09	$0.81^{+0.01}_{-0.01}$	$9.32^{+0.75}_{-1.31}$	$1.59^{+0.06}_{-0.06}$
HD 35187	05:24:01.2	+24:57:37	$160.54^{+1.34}_{-1.32}$	9500-10750	0.50 ± 0.21	9500 ± 205	B9-A0	1.88 ± 0.28	$1.42^{+0.11}_{-0.15}$	$6.83^{+2.98}_{-0.00}$	$2.20^{+0.20}_{-0.00}$
HD 287823	05:24:08.0	+02:27:47	$343.04^{+3.29}_{-3.23}$	8250-8500	0.00 ± 0.00 ($0.39^{+0.03}_{-0.03}$)	8250 ± 125 (*8375 ± 125*)	A4-A6	1.69 ± 0.05	$1.08^{+0.01}_{-0.01}$	$10.56^{+3.36}_{-0.62}$	$1.83^{+0.04}_{-0.03}$
V346 Ori	05:24:42.8	+01:43:48	$336.18^{+2.19}_{-2.16}$	7500-8000	0.00 ± 0.00 ($0.33^{+0.03}_{-0.03}$)	7500 ± 125 (*7750 ± 250*)	A7-A9	1.60 ± 0.06	$0.86^{+0.01}_{-0.01}$	$16.21^{+3.37}_{-5.51}$	$1.65^{+0.04}_{-0.04}$
HD 290409	05:27:05.5	+00:25:08	$403.75^{+7.63}_{-7.35}$	9250-10250	0.50 ± 0.00 ($0.41^{+0.03}_{-0.03}$)	10000 ± 125 (*9750 ± 500*)	B9	1.67 ± 0.06	$1.40^{+0.02}_{-0.03}$	$8.00^{+0.50}_{-0.00}$	$2.18^{+0.02}_{-0.00}$
CO Ori	05:27:38.3	+11:25:39	$394.73^{+3.22}_{-3.17}$	6000-6500	2.00 ± 0.43	6500 ± 215	F3-F6	3.77 ± 0.67	$1.36^{+0.12}_{-0.17}$	$3.92^{+2.07}_{-1.19}$	$2.30^{+0.30}_{-0.35}$
HD 35929	05:27:42.8	−08:19:39	$376.71^{+3.42}_{-3.36}$	6750-7250	0.50 ± 0.05 ($0.35^{+0.05}_{-0.04}$)	7250 ± 125 (*7000 ± 250*)	A9-F0	6.14 ± 0.27	$1.97^{+0.02}_{-0.02}$	$1.20^{+0.30}_{-0.16}$	$3.53^{+0.08}_{-0.13}$
HD 290500	05:29:48.1	−00:23:43	$402.46^{+5.46}_{-5.32}$	8500-10500	1.00 ± 0.15 ($1.03^{+0.06}_{-0.07}$)	8750 ± 156 (*9500 ± 500*)	A2-A3	1.54 ± 0.12	$1.10^{+0.06}_{-0.07}$	<19.92	$1.85^{+0.05}_{-0.00}$

Notes. Column 5 lists the input ranges for the stellar temperatures assumed to carry out SED fitting, as taken from Vioque et al. (2018). The stars indicated in italics in Col. 1 have stellar parameters determined homogeneously from spectroscopy in W2020, which has been followed to set the input ranges for T_* in these cases. The rest of the columns list our results concerning the stellar characterization, as well as the distance-independent results from W2020 for the stars in common (T_* and A_v, between parentheses). Our error bars refer to SED fitting (Sect. 2.1; see also Appendix A). Stars indicated with the dagger have low-quality *Gaia* EDR3 parallaxes according to the criteria described in Sect. 2, and their distance-dependent stellar parameters should be taken with caution. These stars have not been considered in the analysis.

Table B.1. continued.

Object	RA (h:m:s)	Dec (d:m:s)	d (pc)	ΔT_* (K)	A_V (mag)	T_* (K)	Sp. type	R_* ($R_\odot$)	Log(L_*) ($L_\odot$)	t_* (Myr)	M_* ($M_\odot$)
HD 244314	05:30:19.0	+11:20:20	$398.05^{+3.16}_{-3.11}$	8250-8750	0.50 ± 0.00 ($0.51^{+0.06}_{-0.06}$)	8750 ± 125 (8500 ± 250)	A2-A3	1.91 ± 0.06	$1.29^{+0.02}_{-0.02}$	$6.99^{+0.63}_{-0.00}$	$2.12^{+0.04}_{-0.07}$
HD 36112	05:30:27.5	+25:19:57	$155.02^{+0.76}_{-0.75}$	7250-7750	0.00 ± 0.00	7250 ± 125	A9-F0	1.87 ± 0.07	$0.94^{+0.01}_{-0.01}$	$10.92^{+0.23}_{-0.97}$	$1.64^{+0.06}_{-0.04}$
HD 244604	05:31:57.3	+11:17:41	$398.41^{+3.22}_{-3.17}$	8750-9250	0.50 ± 0.00 ($0.59^{+0.04}_{-0.05}$)	8750 ± 130 (9000 ± 250)	A2-A3	2.52 ± 0.09	$1.53^{+0.02}_{-0.02}$	$5.08^{+0.16}_{-0.08}$	$2.16^{+0.04}_{-0.01}$
RY Ori	05:32:09.9	-02:49:47	$346.88^{+2.42}_{-2.39}$	6000-6500	1.00 ± 0.26	6250 ± 194	F4-F9	2.15 ± 0.27	$0.80^{+0.09}_{-0.11}$	$9.42^{+2.19}_{-2.44}$	$1.58^{+0.17}_{-0.17}$
HD 36408	05:32:14.1	+17:03:29	$345.77^{+6.75}_{-6.49}$	11000-13000	0.50 ± 0.00	13000 ± 313	B6-B7	6.53 ± 0.34	$3.04^{+0.02}_{-0.02}$	$0.40^{+0.04}_{-0.01}$	$5.73^{+0.07}_{-0.16}$
HD 288012	05:33:04.8	+02:28:10	$341.35^{+2.41}_{-2.38}$	7250-12250	0.00 ± 0.00	8750 ± 125	A2-A3	1.64 ± 0.05	$1.15^{+0.01}_{-0.01}$	$12.59^{+6.59}_{-2.53}$	$1.87^{+0.03}_{-0.00}$
HBC 442	05:34:14.2	-05:36:54	$383.32^{+2.56}_{-2.52}$	6000-6250	$0.00^{+0.05}_{-0.00}$	6000 ± 125	F8-G1	2.91 ± 0.15	$1.00^{+0.03}_{-0.03}$	$4.81^{+1.17}_{-1.06}$	$2.00^{+0.16}_{-0.14}$
HD 36917	05:34:47.0	-05:34:15	$445.04^{+11.34}_{-10.79}$	9750-12500	1.00 ± 0.00	11500 ± 144	B8	5.09 ± 0.23	$2.61^{+0.03}_{-0.03}$	$0.89^{+0.09}_{-0.09}$	$4.36^{+0.08}_{-0.16}$
HD 245185	05:35:09.6	+10:01:51	$410.35^{+5.19}_{-5.06}$	9500-10500	0.50 ± 0.00 ($0.40^{+0.03}_{-0.02}$)	10250 ± 125 (10000 ± 500)	B9	1.73 ± 0.05	$1.48^{+0.02}_{-0.02}$	$7.08^{+0.60}_{-0.00}$	$2.24^{+0.05}_{-0.00}$
HD 36982	05:35:09.8	-05:27:53	$403.99^{+3.95}_{-3.87}$	19000-21000	1.50 ± 0.00	21000 ± 500	B2	2.78 ± 0.14	$3.13^{+0.01}_{-0.01}$	<0.50	<6.40
NV Ori	05:35:31.4	-05:33:09	$383.86^{+3.01}_{-2.96}$	6500-7000	0.50 ± 0.07	7000 ± 125	F0-F2	3.14 ± 0.15	$1.33^{+0.03}_{-0.03}$	$5.04^{+0.85}_{-0.25}$	$2.09^{+0.06}_{-0.09}$
T Ori †	05:35:50.5	-05:28:35	$398.59^{+4.49}_{-4.39}$	8500-9500	2.00 ± 0.24 ($1.78^{+0.12}_{-0.13}$)	9250 ± 242 (9000 ± 500)	A0-A1	2.98 ± 0.38	$1.77^{+0.09}_{-0.12}$	$3.82^{+0.59}_{-0.82}$	$2.52^{+0.19}_{-0.21}$
CQ Tau †	05:35:58.5	+24:44:54	$148.60^{+1.34}_{-1.31}$	6000-7000	0.50 ± 0.00	6750 ± 125	F2-F3	1.88 ± 0.07	$0.82^{+0.01}_{-0.01}$	$12.42^{+2.40}_{-1.43}$	$1.50^{+0.01}_{-0.01}$
V380 Ori †	05:36:25.4	−06:42:58	$374.32^{+16.33}_{-15.02}$	9000-10500	2.50 ± 0.54 ($2.05^{+0.26}_{-0.35}$)	10250 ± 246 (9750 ± 750)	B9	3.11 ± 1.10	$1.98^{+0.23}_{-0.53}$	$2.96^{+4.82}_{-0.00}$	$2.80^{+0.60}_{-0.00}$
HD 37258	05:36:59.3	-06:09:16	$376.55^{+3.70}_{-3.63}$	9250-10250	0.50 ± 0.00 ($0.54^{+0.03}_{-0.04}$)	9250 ± 125 (9750 ± 500)	A0-A1	1.98 ± 0.07	$1.41^{+0.02}_{-0.02}$	$5.94^{+1.01}_{-0.78}$	$2.27^{+0.03}_{-0.08}$
HD 290770	05:37:02.4	-01:37:21	$392.85^{+3.87}_{-3.80}$	10250-10750	0.50 ± 0.00 ($0.34^{+0.05}_{-0.05}$)	10750 ± 125 (10500 ± 250)	B8	2.13 ± 0.05	$1.74^{+0.01}_{-0.01}$	$4.01^{+0.39}_{-0.04}$	$2.64^{+0.13}_{-0.04}$
BF Ori	05:37:13.3	-06:35:01	$377.85^{+4.03}_{-3.94}$	8750-9250	0.50 ± 0.25 ($0.74^{+0.06}_{-0.07}$)	8750 ± 128 (9000 ± 250)	A2-A3	1.59 ± 0.20	$1.13^{+0.09}_{-0.12}$	$17.14^{+2.80}_{-0.00}$	$1.85^{+0.15}_{-0.00}$
HD 37357 †	05:37:47.1	-06:42:30	$465.07^{+53.15}_{-41.32}$	9250-9750	0.50 ± 0.00 ($0.40^{+0.03}_{-0.03}$)	9750 ± 125 (9500 ± 250)	B9	3.28 ± 0.35	$1.94^{+0.08}_{-0.10}$	$2.96^{+0.44}_{-0.74}$	$2.80^{+0.20}_{-0.20}$
HD 290764	05:38:05.3	-01:15:22	$397.09^{+3.12}_{-3.07}$	7500-8250	0.50 ± 0.00 ($0.58^{+0.07}_{-0.08}$)	7750 ± 125 (7875 ± 375)	A5-A7	2.60 ± 0.10	$1.34^{+0.02}_{-0.02}$	$6.10^{+0.62}_{-0.12}$	$1.99^{+0.03}_{-0.04}$
V1787 Ori	05:38:09.3	-06:49:17	$393.79^{+2.41}_{-2.38}$	8000-8500	4.50 ± 0.00	8500 ± 125	A3-A4	2.43 ± 0.08	$1.44^{+0.01}_{-0.01}$	$5.98^{+0.02}_{-0.14}$	$2.06^{+0.03}_{-0.01}$
HD 37371	05:38:09.9	-00:11:01	$405.25^{+4.56}_{-4.46}$	9750-11500	0.50 ± 0.00	11500 ± 125	B8	2.52 ± 0.07	$2.00^{+0.02}_{-0.02}$	$2.89^{+0.07}_{-0.12}$	$3.13^{+0.10}_{-0.14}$
V599 Ori	05:38:58.6	-07:16:46	$401.27^{+3.20}_{-3.15}$	7750-8250	4.50 ± 0.12 ($4.92^{+0.25}_{-0.35}$)	8250 ± 125 (8000 ± 250)	A4-A6	2.71 ± 0.22	$1.49^{+0.06}_{-0.07}$	$5.09^{+0.91}_{-0.51}$	$2.15^{+0.11}_{-0.10}$
RR Tau †	05:39:30.5	+26:22:27	$900.58^{+375.68}_{-216.58}$	9750-10250	2.00 ± 0.16	9750 ± 228	B9	4.31 ± 0.49	$2.18^{+0.08}_{-0.10}$	$1.89^{+0.15}_{-0.53}$	$3.39^{+0.21}_{-0.33}$
HD 245906 †	05:39:30.5	+26:19:55	$799.45^{+19.62}_{-18.70}$	7750-8250	1.00 ± 0.00	7750 ± 125	A5-A7	5.56 ± 1.84	$2.00^{+0.22}_{-0.47}$	$1.53^{+2.74}_{-0.73}$	$3.40^{+0.79}_{-1.11}$
V350 Ori †	05:40:11.8	-09:42:11	$391.38^{+7.38}_{-7.11}$	8750-9250	0.50 ± 0.45 ($1.06^{+0.08}_{-0.08}$)	8750 ± 238 (9000 ± 250)	A1-A3	1.32 ± 0.42	$0.96^{+0.21}_{-0.43}$	<15.03	<1.91
HD 37806	05:41:02.3	-02:43:01	$397.07^{+4.36}_{4.27}$	9750-11500	0.50 ± 0.00	10750 ± 156	B8	4.08 ± 0.16	$2.30^{+0.02}_{-0.02}$	$1.73^{+0.14}_{-0.19}$	$3.52^{+0.08}_{-0.12}$
HD 38087	05:43:00.6	-02:18:45	$373.09^{+5.33}_{-5.18}$	12750-17000	1.00 ± 0.00	14000 ± 500	B5-B6	3.16 ± 0.25	$2.54^{+0.03}_{-0.03}$	$1.28^{+0.14}_{-0.28}$	$4.23^{+0.17}_{-0.41}$
HD 38120	05:43:11.9	-04:59:50	$380.82^{+4.94}_{-4.82}$	9750-11500	0.50 ± 0.00	11500 ± 125	B8	2.11 ± 0.06	$1.85^{+0.02}_{-0.02}$	$3.95^{+0.08}_{-0.58}$	$2.80^{+0.04}_{-0.04}$
V351 Ori	05:44:18.8	+00:08:40	$322.83^{+2.85}_{-2.80}$	7500-8000	$0.00^{+0.20}_{-0.00}$	7500 ± 190	A7-A9	2.70 ± 0.36	$1.32^{+0.10}_{-0.12}$	$6.03^{+1.96}_{-1.05}$	$1.99^{+0.17}_{-0.18}$
HD 39014 †	05:44:46.3	-65:44:08	$45.72^{+0.21}_{-0.21}$	7500-8000	0.50 ± 0.00	8000 ± 125	A5-A6	3.50 ± 0.11	$1.66^{+0.01}_{-0.01}$	$3.52^{+0.28}_{-0.31}$	$2.48^{+0.07}_{-0.06}$
UCAC4 552-019438	05:50:54.8	+20:14:48	$1428.87^{+35.42}_{-35.42}$	10000-30000	2.50 ± 0.10	11750 ± 263	B7-B8	3.14 ± 0.26	$2.23^{+0.06}_{-0.06}$	$2.00^{+0.15}_{-0.03}$	$3.20^{+0.18}_{-0.03}$
V1818 Ori †	05:53:42.6	-10:24:01	$622.79^{+22.79}_{-21.24}$	115000-14000	3.50 ± 0.24	11500 ± 125	B8	5.43 ± 0.67	$2.67^{+0.09}_{-0.12}$	$0.78^{+0.22}_{-0.18}$	$4.54^{+0.37}_{-0.46}$
HD 249879	05:58:55.8	+16:39:57	$610.86^{+9.90}_{-9.59}$	10750-13000	0.50 ± 0.00	10750 ± 155	B8	1.69 ± 0.07	$1.53^{+0.03}_{-0.03}$	<6.95	<2.40
HD 250550	06:02:00.0	+16:30:57	$743.13^{+28.22}_{-26.23}$	10500-11500	0.50 ± 0.00 ($1.55^{+0.10}_{-0.13}$)	10750 ± 143 (11000 ± 500)	B8	3.60 ± 0.20	$2.19^{+0.04}_{-0.05}$	$2.00^{+0.06}_{-0.05}$	$3.20^{+0.17}_{-0.09}$
PDS 22	06:03:37.1	-14:53:03	$663.42^{+17.60}_{-16.71}$	9500-10750	0.50 ± 0.00	9750 ± 176	B9	2.46 ± 0.13	$1.69^{+0.03}_{-0.04}$	$4.14^{+0.27}_{-0.22}$	$2.40^{+0.24}_{-0.01}$
HD 41511 †	06:04:59.1	-16:29:04	$278.20^{+7.89}_{-7.47}$	8500-9500	1.00 ± 0.20	9500 ± 198	B9-A0	15.81 ± 1.91	$3.26^{+0.09}_{-0.11}$	$0.10^{+0.04}_{-0.02}$	$8.13^{+0.86}_{-0.60}$
PDS 124	06:06:58.5	-05:55:07	$759.92^{+10.74}_{-10.44}$	10000-10500	2.00 ± 0.00 ($1.79^{+0.02}_{-0.01}$)	10500 ± 125 (10250 ± 250)	B8-B9	1.89 ± 0.06	$1.59^{+0.02}_{-0.02}$	$5.96^{+0.14}_{-0.75}$	$2.38^{+0.02}_{-0.05}$
GSC 1876-0892	06:07:15.4	+29:57:55	$4454.83^{+422.29}_{-305.04}$	16000-25000	6.00 ± 0.11	16000 ± 569	B4	21.40 ± 3.43	$4.43^{+0.11}_{-0.15}$	$0.02^{+0.01}_{-0.01}$	$16.04^{+1.98}_{-2.03}$
LkHa 208 †	06:07:49.5	+18:39:26	$574.28^{+48.82}_{-41.72}$	7250-8500	0.50 ± 0.07	7250 ± 125	A9-F0	2.05 ± 0.26	$1.02^{+0.09}_{-0.12}$	$9.96^{+3.39}_{-1.72}$	$1.65^{+0.10}_{-0.05}$
LKHa 338	06:10:47.1	-06:12:51	$841^{+15.54}_{-14.99}$	9750-11500	4.50 ± 0.00	10000 ± 125	B9	2.53 ± 0.10	$1.76^{+0.03}_{-0.03}$	$3.97^{+0.03}_{-0.37}$	$2.56^{+0.06}_{-0.06}$
LkHa 339	06:10:57.8	-06:14:40	$823.96^{+10.36}_{-10.10}$	10250-10750	3.00 ± 0.00 ($3.11^{+0.36}_{-0.54}$)	10250 ± 125 (10500 ± 250)	B9	2.06 ± 0.06	$1.62^{+0.01}_{-0.01}$	$4.91^{+0.21}_{-0.31}$	$2.52^{+0.08}_{-0.11}$
PDS 126	06:13:37.3	-06:25:02	$832.57^{+11.51}_{-11.20}$	7500-8000	1.00 ± 0.00	7750 ± 125	A5-A7	2.86 ± 0.11	$1.42^{+0.02}_{-0.02}$	$5.18^{+0.67}_{-0.19}$	$2.10^{+0.05}_{-0.05}$
MWC 137	06:18:45.5	+15:16:52	$4596.95^{+534.36}_{-508.45}$	24000-33000	5.00 ± 0.00	24000 ± 500	B1	29.95 ± 3.80	$5.43^{+0.09}_{-0.12}$	<0.01	$39.47^{+4.32}_{-4.83}$
CPM 25	06:23:56.3	+14:30:28	$3414.88^{+699.37}_{-450.67}$	16000-25000	4.50 ± 0.10	17000 ± 597	B3-B4	5.63 ± 1.31	$3.38^{+0.16}_{-0.26}$	$0.29^{+0.19}_{-0.09}$	$6.78^{+1.05}_{-1.18}$
HD 46060	06:30:49.8	-09:39:15	$913.13^{+18.69}_{-17.95}$	17000-25000	1.50 ± 0.00	17000 ± 500	B3-B4	6.57 ± 0.41	$3.51^{+0.02}_{-0.02}$	$0.20^{+0.01}_{-0.01}$	$7.47^{+0.31}_{-0.28}$
PDS 129	06:31:03.6	+10:01:13	$650.49^{+7.17}_{-7.01}$	6250-6750	1.00 ± 0.00	6750 ± 125	F2-F3	2.58 ± 0.10	$1.10^{+0.01}_{-0.01}$	$7.64^{+0.40}_{-0.66}$	$1.79^{+0.05}_{-0.04}$

Table B.1. continued.

Object	RA (h:m:s)	Dec (d:m:s)	d (pc)	ΔT_* (K)	A_V (mag)	T_* (K)	Sp. type	R_* ($R_\odot$)	Log(L_*) ($L_\odot$)	t_* (Myr)	M_* ($M_\odot$)
VY Mon †	06:31:06.9	+10:26:05	$329.91^{55.27}_{-45.13}$	8000-16000	6.00 ± 0.00 ($5.62^{+0.34}_{-0.51}$)	13000 ± 557 (12000 ± 4000)	B6-B7	3.50 ± 0.81	$2.50^{+0.16}_{-0.24}$	$1.20^{+0.80}_{-0.22}$	$3.80^{+0.42}_{-0.21}$
LkHa 215	06:32:41.8	+10:09:34	$721.25^{+14.86}_{-14.27}$	13000-15000	2.50 ± 0.22	15000 ± 882	B4-B5	3.92 ± 0.68	$2.85^{+0.10}_{-0.13}$	$0.78^{+0.18}_{-0.18}$	$4.71^{+0.36}_{-0.32}$
HD 259431	06:33:05.2	+10:19:20	$640.04^{+11.37}_{-10.98}$	11000-16000	1.50 ± 0.00	12500 ± 332	B7	6.10 ± 0.51	$2.91^{+0.05}_{-0.06}$	$0.50^{+0.10}_{-0.08}$	$5.24^{+0.30}_{-0.24}$
HBC 217	06:40:42.2	+09:33:37	$704.61^{+6.85}_{-6.72}$	6000-6500	0.50 ± 0.00	6000 ± 125	F8-G1	2.38 ± 0.10	$0.82^{+0.01}_{-0.01}$	$6.89^{+1.13}_{-1.55}$	$1.75^{+0.10}_{-0.10}$
HBC 222	06:40:51.2	+09:44:46	$701.14^{+6.97}_{-6.83}$	6000-6500	0.50 ± 0.17	6500 ± 174	F3-F6	2.42 ± 0.22	$0.97^{+0.07}_{-0.07}$	$8.24^{+1.77}_{-0.00}$	$1.70^{+0.12}_{-0.11}$
PDS 24	06:48:41.7	-16:48:06	$1055.57^{+16.07}_{-16.07}$	10000-11000	1.50 ± 0.05 ($1.54^{+0.10}_{-0.12}$)	10000 ± 125 (10500 ± 500)	B9	1.58 ± 0.07	$1.35^{+0.03}_{-0.03}$	<8.27	<2.20
PDS 130	06:49:58.6	-07:38:52	$1237.04^{+20.30}_{-19.66}$	10250-10750	2.50 ± 0.00 ($2.38^{+0.13}_{-0.15}$)	10500 ± 225 (10500 ± 250)	B8-B9	2.70 ± 0.15	$1.90^{+0.03}_{-0.03}$	$3.08^{+0.22}_{-0.08}$	$2.74^{+0.10}_{-0.13}$
HD 50083	06:51:45.8	+05:05:04	$979.95^{+29.66}_{-27.97}$	16000-20000	1.00 ± 0.00	17000 ± 500	B3-B4	13.11 ± 1.04	$4.11^{+0.04}_{-0.05}$	$0.05^{+0.01}_{-0.01}$	$12.00^{+0.43}_{-0.56}$
PDS 25	06:54:27.9	−25:02:16	$747.32^{+9.84}_{-9.59}$	7750-8250	2.00 ± 0.32	8250 ± 216	A3-A6	1.62 ± 0.24	$1.04^{+0.11}_{-0.14}$	$14.93^{+3.53}_{-0.00}$	$1.76^{+0.19}_{-0.00}$
PDS 229N †	06:55:40.0	-03:09:50	$6087.62^{+2302.38}_{-1986.23}$	12250-12750	2.50 ± 0.00 ($2.24^{+0.15}_{-0.17}$)	12500 ± 223 (12500 ± 250)	B7	12.42 ± 4.61	$3.53^{+0.24}_{-0.58}$	$0.10^{+0.38}_{-0.04}$	$8.78^{+1.88}_{-3.38}$
HT CMa	07:02:42.5	−11:26:12	$1125.28^{+20.07}_{-19.38}$	10000-11000	1.50 ± 0.00 ($1.61^{+0.09}_{-0.09}$)	10000 ± 125 (10500 ± 500)	B9	3.19 ± 0.10	$1.96^{+0.02}_{-0.02}$	$2.96^{+0.03}_{-0.11}$	$2.80^{+0.02}_{-0.02}$
Z CMa †	07:03:43.2	-11:33:06	$639.94^{+290.71}_{-154.26}$	8000-9000	4.00 ± 0.05 ($3.09^{+0.23}_{-0.28}$)	8250 ± 183 (8500 ± 500)	A4-A6	22.88 ± 8.76	$3.34^{+0.25}_{-0.62}$	$0.06^{+0.24}_{-0.03}$	$9.43^{+1.66}_{-3.62}$
HU CMa	07:04:06.7	−11:26:08	$1100.88^{+18.95}_{-18.32}$	12750-13000	1.00 ± 0.17 ($1.29^{+0.07}_{-0.07}$)	12750 ± 125 (13000 ± 250)	B7	2.10 ± 0.23	$2.02^{+0.08}_{-0.10}$	$3.13^{+0.26}_{-0.00}$	$3.00^{+0.27}_{-0.00}$
PDS 241	07:08:38.8	−04:19:05	$5063.17^{+487.41}_{-473.67}$	24000-28000	3.00 ± 0.00 ($2.92^{+0.27}_{-0.37}$)	24000 ± 804 (26000 ± 1500)	B1	11.99 ± 1.66	$4.63^{+0.09}_{-0.12}$	$0.03^{+0.01}_{-0.01}$	$17.82^{+1.40}_{-1.86}$
HD 56895	07:18:31.8	−11:11:34	$165.18^{+0.61}_{-0.61}$	6750-7250	0.00 ± 0.00	6750 ± 125	F2-F3	2.25 ± 0.09	$0.98^{+0.01}_{-0.01}$	$9.50^{+0.50}_{-0.92}$	$1.64^{+0.03}_{-0.04}$
PDS 27 †	07:19:35.9	-17:39:18	$2531.94^{+175.05}_{-153.78}$	14000-21000	5.00 ± 0.07 ($4.96^{+0.33}_{-0.49}$)	15000 ± 688 (17500 ± 3500)	B4-B5	14.83 ± 2.44	$4.00^{+0.10}_{-0.14}$	$0.05^{+0.03}_{-0.01}$	$11.65^{+1.09}_{-1.60}$
GSC 6546-3156	07:24:17.5	-26:16:05	$1271.34^{+33.84}_{-32.13}$	9500-10750	2.00 ± 0.00	9500 ± 125	B9-A0	1.75 ± 0.11	$1.35^{+0.05}_{-0.05}$	$8.02^{+9.03}_{-1.12}$	$2.08^{+0.12}_{-0.06}$
PDS 133	07:25:05.0	-25:45:50	$1389.80^{+42.20}_{-42.20}$	12000-16000	3.50 ± 0.05 ($1.92^{+0.09}_{-0.10}$)	12000 ± 189 (14000 ± 2000)	B7-B8	2.06 ± 0.13	$1.90^{+0.04}_{-0.05}$	$3.84^{+0.66}_{-0.78}$	$2.80^{+0.19}_{-0.00}$
HD 58647	07:25:56.1	-14:10:44	$302.21^{+2.34}_{-2.30}$	10250-10750	0.50 ± 0.00	10750 ± 125	B8	5.06 ± 0.14	$2.49^{+0.12}_{-0.01}$	$1.00^{+0.01}_{-0.03}$	$4.05^{+0.12}_{-0.05}$
HD 59319	07:28:36.8	−21:57:49	$694.28^{+14.49}_{-13.91}$	12000-13000	0.00 ± 0.00 ($0.06^{+0.01}_{-0.02}$)	12000 ± 125 (12500 ± 500)	B7-B8	4.26 ± 0.13	$2.53^{+0.02}_{-0.02}$	$1.04^{+0.05}_{-0.03}$	$4.00^{+0.03}_{-0.08}$
PDS 134	07:32:26.6	−21:55:36	$2406.22^{+88.61}_{-82.53}$	13000-15000	1.50 ± 0.00 ($1.70^{+0.06}_{-0.07}$)	13000 ± 313 (14000 ± 500)	B6-B7	4.82 ± 0.29	$2.78^{+0.03}_{-0.03}$	$0.74^{+0.11}_{-0.04}$	$4.62^{+0.18}_{-0.17}$
GSC 8143-1225 †	07:59:11.6	−50:22:47	$372.21^{+2.52}_{-2.49}$	6500-7000	$0.50^{+0.59}_{-0.00}$	6750 ± 230	F1-F4	1.18 ± 0.56	$0.42^{+0.29}_{-1.21}$	<19.40	<1.53
HD 68695	08:11:44.6	−44:05:09	$374.63^{+2.13}_{-2.11}$	9000-9500	0.50 ± 0.05 ($0.37^{+0.05}_{-0.05}$)	9500 ± 125 (9250 ± 250)	B9-A0	1.75 ± 0.06	$1.35^{+0.02}_{-0.02}$	$8.02^{+0.91}_{-0.74}$	$2.08^{+0.06}_{-0.03}$
PDS 277	08:23:11.8	−39:07:01	$340.73^{+1.52}_{-1.51}$	6500-7000	0.00 ± 0.00	6500 ± 125	F3-F5	2.43 ± 0.10	$0.98^{+0.01}_{-0.01}$	$8.15^{+1.18}_{-0.98}$	$1.70^{+0.05}_{-0.05}$
V388 Vel	08:42:17.3	−40:44:10	$1575.07^{+45.62}_{-43.12}$	9000-10000	4.00 ± 0.05	10000 ± 125	B9	3.89 ± 0.21	$2.13^{+0.04}_{-0.04}$	$2.00^{+0.09}_{-0.06}$	$3.20^{+0.15}_{-0.16}$
GSC 8581-2002	08:44:23.6	-59:56:58	$534.12^{+3.61}_{-3.56}$	9500-10000	1.00 ± 0.00 ($1.54^{+0.05}_{-0.07}$)	9750 ± 125 (9750 ± 250)	B9	2.02 ± 0.06	$1.52^{+0.01}_{-0.01}$	$5.12^{+0.86}_{-0.12}$	$2.40^{+0.00}_{-0.09}$
PDS 33	08:48:45.7	−40:48:21	$880.17^{+8.71}_{-8.54}$	9500-10000	1.00 ± 0.00 ($1.03^{+0.03}_{-0.02}$)	9750 ± 125 (9750 ± 250)	B9	1.61 ± 0.05	$1.33^{+0.01}_{-0.01}$	<9.19	<2.10
PDS 34	08:49:58.5	−45:53:06	$1970.93^{+53.04}_{-50.34}$	16000-25000	3.00 ± 0.00	16000 ± 500	B4	2.58 ± 0.21	$2.60^{+0.04}_{-0.05}$	$1.48^{+1.46}_{-0.00}$	$4.31^{+0.29}_{-0.00}$
HD 76534	08:55:08.7	−43:28:00	$875.09^{+23.13}_{-21.97}$	18000-20000	1.00 ± 0.00 ($0.95^{+0.07}_{-0.08}$)	20000 ± 500 (19000 ± 500)	B2	6.10 ± 0.46	$3.73^{+0.05}_{-0.05}$	$0.17^{+0.03}_{-0.04}$	$8.61^{+0.37}_{-0.54}$
SAO 220669	08:55:45.9	−44:25:14	$867.79^{+9.31}_{-9.11}$	14000-18000	2.50 ± 0.00 ($2.32^{+0.09}_{-0.09}$)	16000 ± 500 (16000 ± 1500)	B4	9.48 ± 0.82	$3.72^{+0.05}_{-0.06}$	$0.10^{+0.03}_{-0.01}$	$9.00^{+0.48}_{-0.44}$
PDS 286	09:06:00.0	−47:18:58	$1780.03^{+43.41}_{-41.39}$	27000-33000	6.00 ± 0.00 ($6.44^{+0.35}_{-0.56}$)	27000 ± 500 (30000 ± 3000)	B0	15.50 ± 0.83	$5.06^{+0.03}_{-0.04}$	$0.02^{+0.01}_{-0.01}$	$26.08^{+1.41}_{-1.55}$
PDS 297	09:42:40.3	−56:15:34	$1592.64^{+30.50}_{-29.38}$	10500-11000	1.50 ± 0.00 ($1.23^{+0.06}_{-0.06}$)	11000 ± 125 (10750 ± 250)	B8	3.67 ± 0.11	$2.25^{+0.02}_{-0.02}$	$1.97^{+0.02}_{-0.05}$	$3.36^{+0.04}_{-0.10}$
HD 87403	10:02:51.4	−59:16:55	$1464.29^{+70.38}_{-64.21}$	9750-10250	0.50 ± 0.00 ($0.34^{+0.04}_{-0.05}$)	10250 ± 125 (10000 ± 250)	B9	8.22 ± 0.43	$2.83^{+0.04}_{-0.04}$	$0.40^{+0.05}_{-0.06}$	$5.54^{+0.23}_{-0.26}$
HD 87643 †	10:04:30.3	−58:39:52	$1951.01^{+1806.83}_{-474.27}$	16000-25000	2.50 ± 0.17	16000 ± 500	B4	21.28 ± 7.24	$4.43^{+0.22}_{-0.48}$	$0.02^{+0.05}_{-0.01}$	$16.02^{+3.98}_{-5.23}$
PDS 37	10:10:00.3	−57:02:07	$1629.07^{+62.54}_{-58.08}$	14000-21000	5.50 ± 0.00 ($5.64^{+0.38}_{-0.60}$)	19000 ± 625 (17500 ± 3500)	B2-B3	7.42 ± 0.71	$3.81^{+0.06}_{-0.06}$	$0.10^{+0.04}_{-0.01}$	$9.04^{+0.73}_{-0.21}$
HD 305298	10:33:05.0	−60:19:51	$4431.37^{+264.85}_{-236.57}$	33000-35000	2.00 ± 0.18 ($1.51^{+0.12}_{-0.14}$)	34000 ± 500 (34000 ± 1000)	O	7.70 ± 1.00	$4.85^{+0.10}_{-0.13}$	<0.04	$23.22^{+1.03}_{-2.94}$
PDS 322 †	10:52:08.7	−56:12:07	$4280.71^{+1166.21}_{-1197.71}$	16000-25000	1.50 ± 0.00	21000 ± 500	B2	5.91 ± 1.83	$3.79^{+0.21}_{-0.41}$	$0.14^{+0.17}_{-0.05}$	$8.99^{+1.44}_{-1.91}$
HD 94509	10:53:27.2	−58:25:24	$1608.62^{+45.44}_{-43.01}$	10500-12500	0.50 ± 0.00 ($0.35^{+0.01}_{-0.02}$)	12250 ± 138 (11500 ± 1000)	B7	7.98 ± 0.37	$3.11^{+0.03}_{-0.04}$	$030^{+0.02}_{-0.02}$	$6.21^{+0.20}_{-0.20}$
PDS 324	10:57:24.2	−62:53:13	$3440.69^{+262.53}_{-227.77}$	19000-29000	3.50 ± 0.00	19000 ± 500	B2-B3	3.97 ± 0.35	$3.27^{+0.06}_{-0.07}$	$0.35^{+0.06}_{-0.06}$	$6.59^{+0.42}_{-0.23}$
HD 95881	11:01:57.6	−71:30:48	$1098.03^{+24.34}_{-23.30}$	9750-10250	0.50 ± 0.00 ($0.72^{+0.03}_{-0.04}$)	9750 ± 125 (10000 ± 250)	B9	10.66 ± 0.36	$2.97^{+0.02}_{-0.02}$	$0.23^{+0.04}_{-0.03}$	$6.40^{+0.07}_{-0.19}$
HD 96042	11:03:40.5	−59:25:59	$2702.01^{+188.06}_{-165.08}$	24000-27000	1.50 ± 0.00 ($1.13^{+0.08}_{-0.08}$)	27000 ± 500 (25500 ± 1500)	B0	13.51 ± 1.02	$4.94^{+0.05}_{-0.06}$	$0.02^{+0.01}_{-0.01}$	$23.74^{+0.30}_{-1.98}$
HD 97048	11:08:03.2	−77:39:17	$184.11^{+0.85}_{-0.84}$	10000-11000	1.50 ± 0.00 ($1.37^{+0.05}_{-0.06}$)	11000 ± 125 (10500 ± 500)	B8	2.22 ± 0.06	$1.81^{+0.01}_{-0.01}$	$3.90^{+0.07}_{-0.60}$	$2.80^{+0.03}_{-0.03}$
HD 98922	11:22:31.7	−53:22:11	$643.56^{+8.70}_{-8.47}$	10250-10750	0.50 ± 0.00 ($0.45^{+0.07}_{-0.07}$)	10500 ± 125 (10500 ± 250)	B8-B9	11.45 ± 0.36	$3.16^{+0.02}_{-0.02}$	$0.20^{+0.01}_{-0.01}$	$7.01^{+0.11}_{-0.02}$
HD 100453	11:33:05.5	−54:19:29	$103.61^{+0.24}_{-0.24}$	7000-7500	0.00 ± 0.00 ($0.12^{+0.04}_{-0.04}$)	7250 ± 125 (7250 ± 250)	A9-F0	1.58 ± 0.06	$0.79^{+0.01}_{-0.01}$	$19.28^{+0.70}_{-0.68}$	$1.60^{+0.05}_{-0.04}$
HD 100546	11:33:25.3	−70:11:41	$107.97^{+0.44}_{-0.44}$	9250-10250	0.00 ± 0.00 ($0.17^{+0.02}_{-0.03}$)	9250 ± 125 (9750 ± 500)	A0-A1	1.83 ± 0.05	$1.34^{+0.01}_{-0.01}$	$7.67^{+0.36}_{-0.67}$	$2.10^{+0.05}_{-0.03}$
HD 101412	11:39:44.4	−60:10:28	$409.90^{2.52}_{-2.49}$	9500-10000	0.50 ± 0.00 ($0.69^{+0.03}_{-0.03}$)	9500 ± 125 (9750 ± 250)	B9-A0	2.57 ± 0.07	$1.69^{+0.01}_{-0.01}$	$4.06^{+0.08}_{-0.01}$	$2.39^{+0.01}_{-0.02}$

Table B.1. continued.

Object	RA (h:m:s)	Dec (d:m:s)	d (pc)	ΔT_* (K)	A_v (mag)	T_* (K)	Sp. type	R_* ($R_\odot$)	Log(L_*) ($L_\odot$)	t_* (Myr)	M_* ($M_\odot$)
PDS 344	11:40:32.8	−64:32:06	$2150.65^{+53.63}_{-51.08}$	14000-16000	1.50 ± 0.00 ($1.27^{+0.07}_{-0.07}$)	14000 ± 500 (15250 ± 500)	B5-B6	2.32 ± 0.20	$2.27^{+0.04}_{-0.04}$	$2.09^{+1.89}_{-0.00}$	$3.56^{+0.24}_{-0.00}$
PDS 138	11:53:13.2	−62:05:21	$9691.91^{+1380.35}_{-1041.98}$	24000-33000	5.00 ± 0.00	24000 ± 500	B1	33.72 ± 4.49	$5.53^{+0.10}_{-0.13}$	<0.01	$44.33^{+5.40}_{-6.50}$
HD 104237	12:00:04.9	−78:11:35	$106.49^{+0.49}_{-0.48}$	7750-8250	$0.00^{+0.07}_{-0.00}$ ($0.29^{+0.05}_{-0.06}$)	7750 ± 125 (8000 ± 250)	A5-A7	2.44 ± 0.13	$1.29^{+0.04}_{-0.04}$	$6.99^{+0.43}_{-0.87}$	$1.90^{+0.07}_{-0.05}$
GSC 8645-1401	12:17:47.5	−59:43:59	$1828.76^{+63.34}_{-59.24}$	6750-7250	2.50 ± 0.37	7000 ± 222	A9-F2	8.27 ± 1.91	$2.17^{+0.16}_{-0.26}$	$0.69^{+0.72}_{-0.29}$	$4.26^{+0.70}_{-0.86}$
Hen 2-80 †	12:22:23.2	−63:17:17	$10154.04^{+8252.45}_{-3371.34}$	13000-15000	3.00 ± 0.26	15000 ± 985	B4-B5	24.94 ± 11.80	$4.45^{+0.28}_{-1.04}$	$0.02^{+0.19}_{-0.01}$	$17.13^{+5.83}_{-10.12}$
Hen 3-823 †	12:48:42.4	−59:54:35	$1512.52^{+155.09}_{-128.70}$	15000-20000	1.50 ± 0.00	16000 ± 500	B4	5.59 ± 0.89	$3.27^{+0.10}_{-0.13}$	$0.31^{+0.15}_{-0.06}$	$6.28^{+0.68}_{-0.65}$
PDS 361S	13:03:21.5	−62:13:26	$3282.52^{+118.64}_{-110.64}$	17000-20000	2.00 ± 0.00 ($2.20^{+0.13}_{-0.15}$)	17000 ± 500 (18500 ± 1000)	B3-B4	4.53 ± 0.31	$3.19^{+0.03}_{-0.03}$	$0.40^{+0.03}_{-0.01}$	$5.85^{+0.16}_{-0.07}$
GSC 8994-3902	13:19:04.0	−62:34:10	$2032.91^{+71.54}_{-66.84}$	16000-25000	1.50 ± 0.00	16000 ± 500	B4	6.10 ± 0.45	$3.34^{+0.03}_{-0.04}$	$0.29^{+0.01}_{-0.05}$	$6.63^{+0.35}_{-0.23}$
PDS 364 †	13:20:03.6	−62:23:54	$5069.50^{+2307.70}_{-1374.96}$	11500-14000	2.00 ± 0.00 ($2.02^{+0.18}_{-0.22}$)	11500 ± 125 (12500 ± 1000)	B8	7.74 ± 2.82	$2.98^{+0.24}_{-0.56}$	$0.37^{+1.07}_{-0.17}$	$5.80^{+1.21}_{-2.13}$
Hen 3-938	13:52:42.8	−63:32:49	$5898.42^{+478.53}_{-411.73}$	29000-35000	5.50 ± 0.00	31000 ± 500	O	20.24 ± 1.78	$5.53^{+0.07}_{-0.08}$	<0.01	$43.92^{+2.33}_{-3.99}$
PDS 69	13:57:43.9	−39:58:47	$672.74^{+7.41}_{-7.25}$	13000-17000	2.00 ± 0.22 ($1.65^{+0.19}_{-0.23}$)	16000 ± 886 (15000 ± 2000)	B4-B5	4.10 ± 0.75	$3.00^{+0.11}_{-0.15}$	$0.60^{+0.17}_{-0.15}$	$5.20^{+0.41}_{-0.40}$
DG Cir	15:03:23.8	−63:22:59	$861.12^{+14.80}_{-14.31}$	8000-14000	4.00 ± 0.26 ($4.00^{+0.25}_{-0.32}$)	8750 ± 215 (11000 ± 3000)	A2-A3	5.04 ± 0.60	$2.13^{+0.09}_{-0.11}$	$1.61^{+0.39}_{-0.54}$	$3.43^{+0.35}_{-0.26}$
HD 132947	15:04:56.0	−63:07:53	$377.28^{+2.93}_{-2.88}$	10000-10500	0.50 ± 0.00 ($0.29^{+0.03}_{-0.02}$)	10500 ± 125 (10250 ± 250)	B8-B9	2.40 ± 0.06	$1.80^{+0.01}_{-0.01}$	$3.75^{+0.04}_{-0.81}$	$2.77^{+0.05}_{-0.01}$
PDS 389	15:14:47.0	−62:17:00	$765.01^{+8.55}_{-8.36}$	8250-9000	5.00 ± 0.00	9000 ± 125	A1-A2	4.66 ± 0.18	$2.11^{+0.02}_{-0.02}$	$1.87^{+0.09}_{-0.18}$	$3.37^{+0.04}_{-0.15}$
HD 135344B	15:15:48.4	−37:09:16	$134.44^{+0.43}_{-0.43}$	6250-6500	0.00 ± 0.00 ($0.53^{+0.18}_{-0.22}$)	6250 ± 125 (6375 ± 125)	F5-F8	1.92 ± 0.08	$0.71^{+0.01}_{-0.01}$	$10.48^{+0.97}_{-0.49}$	$1.46^{+0.07}_{-0.04}$
HD 135344	15:15:48.9	−37:08:56	$134.36^{+0.73}_{-0.72}$	6500-7000	0.00 ± 0.00	7000 ± 125	F0-F2	2.22 ± 0.08	$1.03^{+0.01}_{-0.01}$	$9.35^{+0.51}_{-0.35}$	$1.66^{+0.04}_{-0.01}$
HD 139614	15:40:46.4	−42:29:54	$133.10^{+0.48}_{-0.48}$	7500-8000	0.00 ± 0.00 ($0.21^{+0.04}_{-0.04}$)	7500 ± 125 (7750 ± 250)	A7-A9	1.54 ± 0.05	$0.83^{+0.01}_{-0.01}$	$19.35^{+0.64}_{-0.00}$	$1.60^{+0.02}_{-0.00}$
HD 141569	15:49:57.7	−03:55:17	$111.13^{+0.36}_{-0.36}$	9250-9750	0.50 ± 0.00 ($0.38^{+0.02}_{-0.03}$)	9750 ± 125 (9500 ± 250)	B9	1.75 ± 0.05	$1.40^{+0.01}_{-0.01}$	$7.97^{+0.03}_{-0.03}$	$2.12^{+0.04}_{-0.01}$
HD 141926	15:54:21.8	−55:19:44	$1323.57^{+32.21}_{-30.71}$	26000-30000	2.50 ± 0.09 ($2.61^{+0.17}_{-0.20}$)	26000 ± 500 (28000 ± 1500)	B0	9.84 ± 0.66	$4.60^{+0.05}_{-0.05}$	$0.03^{+0.01}_{-0.01}$	$16.91^{+1.00}_{-0.88}$
HD 142666	15:56:40.0	−22:01:40	$145.52^{+0.46}_{-0.46}$	7000-7500	1.00 ± 0.00 ($0.82^{+0.07}_{-0.08}$)	7250 ± 125 (7250 ± 250)	A9-F0	2.33 ± 0.08	$1.13^{+0.01}_{-0.01}$	$8.73^{+0.08}_{-0.74}$	$1.75^{+0.03}_{-0.00}$
HD 142527	15:56:41.9	−42:19:24	$158.51^{+0.72}_{-0.71}$	6250-6750	1.00 ± 0.00 ($1.20^{+0.04}_{-0.05}$)	6750 ± 125 (6500 ± 250)	F2-F3	3.46 ± 0.13	$1.35^{+0.01}_{-0.01}$	$4.40^{+0.49}_{-0.38}$	$2.20^{+0.05}_{-0.05}$
Hen 3-1121 †	15:58:09.6	−53:51:18	$3056.53^{+656.16}_{-593.80}$	22000-32000	4.00 ± 0.00	22000 ± 500	B1-B2	7.36 ± 1.55	$4.06^{+0.15}_{-0.23}$	$0.08^{+0.04}_{-0.02}$	$10.99^{+1.09}_{-1.95}$
Hen 3-1121S †	15:58:09.7	−53:51:35	$2243.01^{+620.75}_{-475.41}$	24000-33000	3.50 ± 0.00	30000 ± 568	O-B0	8.54 ± 2.27	$4.73^{+0.18}_{-0.32}$	$0.03^{+0.03}_{-0.01}$	$19.14^{+3.92}_{-3.44}$
HD 143006	15:58:36.9	−22:57:16	$166.38^{+0.51}_{-0.50}$	5250-5500	0.50 ± 0.05	5500 ± 125	G7-G9	2.06 ± 0.10	$0.54^{+0.02}_{-0.02}$	$5.10^{+1.89}_{-0.00}$	$1.74^{+0.10}_{-0.13}$
HD 144432	16:06:57.9	−27:43:10	$154.03^{+0.59}_{-0.58}$	7250-7750	0.50 ± 0.00 ($0.48^{+0.04}_{-0.05}$)	7750 ± 125 (7500 ± 250)	A5-A7	2.23 ± 0.08	$1.21^{+0.01}_{-0.01}$	$7.98^{+0.02}_{-0.21}$	$1.82^{+0.03}_{-0.01}$
HR 5999	16:08:34.3	−39:06:19	$157.79^{+0.85}_{-0.84}$	8250-8750	1.00 ± 0.20 ($0.87^{+0.03}_{-0.03}$)	8250 ± 202 (8500 ± 250)	A4-A6	4.74 ± 0.52	$1.97^{+0.08}_{-0.09}$	$1,98^{+0.33}_{-0.41}$	$3.19^{+0.21}_{-0.29}$
WRAY 15-1435	16:13:06.7	−50:23:20	$2469.38^{+128.95}_{-116.76}$	19000-29000	4.00 ± 0.00	19000 ± 500	B2-B3	7.93 ± 0.58	$3.87^{+0.05}_{-0.05}$	$0.10^{+0.01}_{-0.01}$	$9.96^{+0.31}_{-0.63}$
V718 Sco	16:13:11.6	−22:29:07	$153.92^{+0.49}_{-0.48}$	7500-8000	1.00 ± 0.07 ($1.10^{+0.06}_{-0.06}$)	7500 ± 125 (7750 ± 250)	A7-A8	2.05 ± 0.11	$1.08^{+0.03}_{-0.04}$	$9.02^{+0.56}_{-0.11}$	$1.71^{+0.04}_{-0.02}$
Hen 3-1191	16:27:15.1	−48:39:27	$1687.14^{+139.17}_{-119.46}$	24000-33000	4.50 ± 0.12	24000 ± 500	B1	4.17 ± 0.50	$3.72^{+0.09}_{-0.11}$	$0.19^{+0.05}_{-0.00}$	$9.38^{+0.65}_{-0.00}$
HD 149914	16:38:28.6	−18:13:14	$153.45^{+0.63}_{-0.62}$	9500-11250	1.00 ± 0.00	9500 ± 125	B9-A0	3.92 ± 0.11	$2.05^{+0.01}_{-0.01}$	$2.02^{+0.05}_{-0.02}$	$3.07^{+0.07}_{-0.05}$
HD 150193	16:40:17.9	−23:53:45	$150.02^{+0.48}_{-0.47}$	9000-9500	1.50 ± 0.00 ($1.88^{+0.16}_{-0.20}$)	9000 ± 125 (9250 ± 250)	A1-A2	1.98 ± 0.06	$1.36^{+0.01}_{-0.01}$	$6.00^{+1.00}_{-0.02}$	$2.25^{+0.00}_{-0.08}$
AK Sco †	16:54:44.8	−36:53:19	$139.15^{+0.61}_{-0.60}$	6000-6500	0.50 ± 0.25 ($0.51^{+0.03}_{-0.02}$)	6000 ± 246 (6250 ± 250)	F7-G5	2.20 ± 0.34	$0.75^{+0.10}_{-0.13}$	$7.83^{+2.92}_{-2.78}$	$1.65^{+0.25}_{-0.22}$
PDS 431	16:54:59.2	−43:21:50	$1632^{+42.37}_{-40.28}$	10000-11000	2.00 ± 0.00 ($2.10^{+0.12}_{-0.14}$)	10000 ± 125 (10500 ± 500)	B9	3.02 ± 0.12	$1.92^{+0.03}_{-0.03}$	$3.01^{+0.06}_{-0.02}$	$2.72^{+0.08}_{-0.10}$
V921 Sco	16:59:06.8	−42:42:08	$1398.97^{+72.65}_{-65.71}$	24000-33000	5.50 ± 0.00	26000 ± 946	B0-B1	14.31 ± 2.09	$4.93^{+0.10}_{-0.13}$	$0.02^{+0.01}_{-0.01}$	$23.47^{+1.11}_{-3.45}$
HD 155448	17:12:58.8	−32:14:34	$1011.57^{+47.08}_{-43.07}$	9750-11500	0.50 ± 0.00	11500 ± 125	B8	6.44 ± 0.34	$2.82^{+0.04}_{-0.04}$	$0.52^{+0.08}_{-0.04}$	$5.08^{+0.20}_{-0.21}$
MWC 878	17:24:44.7	−38:43:51	$1787.61^{+74.20}_{-68.51}$	19000-29000	3.50 ± 0.00	28500 ± 500	B0	9.37 ± 0.65	$4.69^{+0.05}_{-0.06}$	$0.03^{+0.01}_{-0.01}$	$18.05^{+1.17}_{-0.34}$
HD 319896	17:31:05.9	−35:08:29	$1290.16^{+42.22}_{-39.63}$	15000-17000	2.50 ± 0.00	15000 ± 500	B4-B5	6.11 ± 0.45	$3.23^{+0.03}_{-0.03}$	$0.31^{+0.07}_{-0.01}$	$6.22^{+0.19}_{-0.20}$
HD 158643 †	17:31:25.0	−23:57:46	$125.07^{+1.66}_{-1.62}$	9500-10750	0.00 ± 0.00	9500 ± 150	B9-A0	4.93 ± 0.15	$2.25^{+0.01}_{-0.01}$	$1.35^{+0.16}_{-0.14}$	$3.60^{+0.07}_{-0.02}$
HD 323771	17:34:04.6	−39:23:41	$1060.75^{+29.21}_{-27.69}$	14000-16000	1.50 ± 0.19	14000 ± 755	B5-B6	3.16 ± 0.72	$2.54^{+0.15}_{-0.22}$	$1.28^{+0.74}_{-0.30}$	$4.22^{+0.16}_{-0.62}$
SAO 185668	17:43:55.6	−22:05:45	$1469.34^{+40.38}_{-38.38}$	16000-20000	2.00 ± 0.00	17000 ± 500	B3-B4	8.87 ± 0.85	$3.77^{+0.06}_{-0.07}$	$0.10^{+0.04}_{-0.01}$	$9.03^{+0.84}_{-0.36}$
MWC 593	17:49:10.2	−24:14:21	$1389.03^{+45.93}_{-43.08}$	15000-17000	2.50 ± 0.00	15000 ± 500	B4-B5	10.44 ± 0.78	$3.70^{+0.03}_{-0.03}$	$0.10^{+0.01}_{-0.01}$	$9.00^{+0.28}_{-0.15}$
PDS 469	17:50:58.1	−14:16:12	$979.83^{+58.46}_{-52.22}$	8750-10250	2.00 ± 0.09 ($1.94^{+0.12}_{-0.13}$)	9500 ± 377 (9500 ± 750)	B9-A1	2.48 ± 0.33	$1.66^{+0.08}_{-0.10}$	$4.16^{+0.80}_{-0.16}$	$2.35^{+0.07}_{-0.06}$
HD 163296	17:56:21.3	−21:57:22	$100.57^{+0.41}_{-0.41}$	8750-9250	$0.00^{+0.09}_{-0.00}$ ($0.29^{+0.01}_{-0.02}$)	8750 ± 125 (9000 ± 250)	A2-A3	1.70 ± 0.10	$1.19^{+0.04}_{-0.05}$	$10.00^{+9.50}_{-2.00}$	$1.91^{+0.12}_{-0.00}$
PDS 477 †	18:00:30.3	−16:47:26	$5342.63^{+2012.55}_{-1544.05}$	19000-29000	4.50 ± 0.00	19000 ± 500	B2-B3	11.48 ± 3.88	$4.19^{+0.22}_{-0.48}$	$0.05^{+0.12}_{-0.02}$	$12.17^{+3.18}_{-3.74}$
HD 313571	18:01:07.2	−22:15:04	$1468.81^{+47.82}_{-44.90}$	15000-20000	2.50 ± 0.00	16000 ± 500	B4	10.26 ± 0.86	$3.79^{+0.05}_{-0.05}$	$0.10^{+0.01}_{-0.02}$	$9.54^{+0.46}_{-0.54}$

Table B.1. continued.

Object	RA (h:m:s)	Dec (d:m:s)	d (pc)	ΔT_* (K)	A_v (mag)	T_* (K)	Sp. type	R_* ($R_\odot$)	Log(L_*) ($L_\odot$)	t_* (Myr)	M_* ($M_\odot$)
LKHa 260 †	18:19:09.4	−13:50:41	$1526.97^{+97.37}_{-86.35}$	13000-15000	4.00 ± 0.21	14000 ± 798	B5-B6	3.32 ± 0.70	$2.58^{+0.13}_{-0.19}$	$1.13^{+0.79}_{-0.23}$	$4.01^{+0.38}_{-0.21}$
HD 169142	18:24:29.8	−29:46:50	$114.42^{+0.35}_{-0.35}$	7000-8000	0.00 ± 0.00	7250 ± 125	A9-F0	1.51 ± 0.05	$0.76^{+0.01}_{-0.01}$	<20.00	$1.55^{+0.03}_{-0.00}$
MWC 297	18:27:39.5	−03:49:52	$407.79^{+5.06}_{-4.94}$	22000-26000	8.50 ± 0.00 ($7.87^{+0.41}_{-0.64}$)	26000 ± 500 (24000 ± 2000)	B0	12.05 ± 0.61	$4.78^{+0.03}_{-0.03}$	$0.02^{+0.01}_{-0.01}$	$19.98^{+0.06}_{-0.45}$
VV Ser †	18:28:47.9	+00:08:40	$403.44^{+6.06}_{-5.89}$	13000-15000	4.00 ± 0.36 ($3.74^{+0.22}_{-0.27}$)	14000 ± 709 (14000 ± 1000)	B5-B6	2.43 ± 0.54	$2.31^{+0.15}_{-0.22}$	$2.00^{+1.00}_{-0.00}$	$3.61^{+0.49}_{-0.00}$
V431 Sct	18:29:25.7	−06:04:37	$1693.96^{+78.36}_{-71.72}$	21000-25000	4.00 ± 0.00 ($3.85^{+0.21}_{-0.28}$)	21000 ± 500 (23000 ± 2000)	B2	8.49 ± 0.56	$4.10^{+0.04}_{-0.04}$	$0.07^{+0.01}_{-0.01}$	$11.21^{+0.68}_{-0.21}$
PDS 520 †	18:30:06.2	+00:42:33	$374.89^{+12.01}_{-11.29}$	6500-7000	4.50 ± 0.60	6750 ± 239	F1-F4	2.07 ± 0.59	$0.91^{+0.19}_{-0.35}$	$10.22^{+9.65}_{-0.00}$	$1.55^{+0.25}_{-0.00}$
AS 310	18:33:21.2	−04:58:06	$2380.46^{+73.64}_{-69.35}$	24000-28000	4.00 ± 0.09 ($3.86^{+0.20}_{-0.24}$)	28000 ± 500 (26000 ± 2000)	B0	6.32 ± 0.52	$4.34^{+0.06}_{-0.07}$	$0.05^{+0.01}_{-0.01}$	$14.40^{+0.97}_{-0.62}$
PDS 530 †	18:41:34.4	+08:08:21	$905.99^{+267.44}_{-156.87}$	8000-8500	1.50 ± 0.24	8000 ± 244	A4-A7	1.56 ± 0.61	$0.95^{+0.25}_{-0.65}$	$18.34^{+1.51}_{-0.00}$	$1.70^{+0.20}_{-0.00}$
MWC 953	18:43:28.4	−03:46:17	$1996.16^{+74.97}_{-69.74}$	16000-25000	3.50 ± 0.14	16000 ± 575	B4	14.70 ± 2.43	$4.11^{+0.11}_{-0.15}$	$0.05^{+0.02}_{-0.01}$	$12.06^{+1.88}_{-1.22}$
PDS 543	18:48:00.7	+02:54:17	$1445.70^{+60.29}_{-55.65}$	26000-31000	6.50 ± 0.00 ($7.11^{+0.28}_{-0.40}$)	30000 ± 554 (28500 ± 2500)	O-B0	12.81 ± 0.90	$5.08^{+0.05}_{-0.05}$	$0.02^{+0.01}_{-0.01}$	$26.92^{+1.07}_{-2.44}$
HD 174571	18:50:47.2	+08:42:10	$1287.18^{+30.65}_{-29.25}$	16000-25000	2.50 ± 0.00	22000 ± 521	B1-B2	12.07 ± 0.85	$4.49^{+0.04}_{-0.05}$	$0.04^{+0.01}_{-0.01}$	$15.87^{+0.16}_{-1.02}$
HD 176386	19:01:38.9	−36:53:27	$154.32^{+0.72}_{-0.71}$	9750-11500	0.50 ± 0.00	9750 ± 125	B9	2.32 ± 0.06	$1.64^{+0.01}_{-0.01}$	$3.88^{+0.57}_{-0.01}$	$2.63^{+0.00}_{-0.25}$
TY CrA †	19:01:40.8	−36:52:34	$158.30^{+4.44}_{-4.20}$	9750-11500	2.00 ± 0.61	11250 ± 250	B8	1.60 ± 0.62	$1.57^{+0.25}_{-0.64}$	<4.00	$2.58^{+0.22}_{-0.00}$
HD 179218	19:11:11.3	+15:47:15	$257.95^{+2.21}_{-2.17}$	9250-9750	0.50 ± 0.00 ($0.33^{+0.02}_{-0.02}$)	9750 ± 125 (9500 ± 250)	B9	3.59 ± 0.10	$2.02^{+0.01}_{-0.01}$	$2.35^{+0.19}_{-0.16}$	$2.99^{+0.01}_{-0.04}$
HD 344261	19:21:53.5	+21:31:51	$292.42^{+1.18}_{-1.17}$	6750-7250	0.50 ± 0.00	7000 ± 125	F0-F2	1.67 ± 0.06	$0.78^{+0.01}_{-0.01}$	$18.09^{+1.28}_{-1.93}$	$1.55^{+0.06}_{-0.05}$
WW Vul	19:25:58.8	+21:12:31	$480.13^{+4.29}_{-4.22}$	8500-9250	1.00 ± 0.09	8500 ± 125	A3-A4	2.33 ± 0.16	$1.41^{+0.05}_{-0.06}$	$6.02^{+0.52}_{-0.20}$	$2.04^{+0.06}_{-0.05}$
PX Vul †	19:26:40.3	+23:53:51	$621.71^{+20.53}_{-19.25}$	6500-7250	1.50 ± 0.00	6500 ± 125	F3-F5	4.38 ± 0.24	$1.49^{+0.03}_{-0.03}$	$2.95^{+0.20}_{-0.64}$	$2.59^{+0.13}_{-0.18}$
PDS 581 †	19:36:18.9	+29:32:50	$1574.38^{+229.55}_{-188.43}$	19000-29000	3.00 ± 0.00	19000 ± 500	B2-B3	5.69 ± 0.82	$3.58^{+0.10}_{-0.13}$	$0.20^{+0.07}_{-0.03}$	$7.85^{+0.39}_{-0.85}$
V1295 Aql	20:03:02.5	+05:44:17	$824.16^{+21.83}_{-20.73}$	9500-10000	0.50 ± 0.00 ($0.20^{+0.04}_{-0.04}$)	9750 ± 125 (9750 ± 250)	B9	9.68 ± 0.44	$2.88^{+0.03}_{-0.03}$	$0.30^{+0.02}_{-0.02}$	$6.00^{+0.20}_{-0.21}$
V1685 Cyg	20:20:28.2	+41:21:51	$893.41^{+15.63}_{-15.10}$	19000-27000	3.50 ± 0.00 ($3.33^{+0.34}_{-0.51}$)	19000 ± 500 (23000 ± 4000)	B2-B3	6.52 ± 0.36	$3.70^{+0.02}_{-0.02}$	$0.17^{+0.01}_{-0.02}$	$8.33^{+0.28}_{-0.20}$
V1686 Cyg †	20:20:29.3	+41:21:28	$665.82^{+78.36}_{-83.28}$	5750-6250	2.50 ± 0.69	6250 ± 237	F4-G0	4.00 ± 1.33	$1.34^{+0.22}_{-0.45}$	$3.02^{+5.98}_{-1.11}$	$2.40^{+0.60}_{-0.77}$
MWC 1021	20:29:26.9	+41:40:44	$3090.47^{+258.70}_{-221.60}$	10000-30000	9.00 ± 0.00	13000 ± 313	B6-B7	154.47 ± 17.18	$5.79^{+0.08}_{-0.10}$	<0.01	$73.64^{+6.30}_{-6.63}$
V1478 Cyg †	20:32:45.5	+40:39:37	$1669.83^{+201.74}_{-176.25}$	10000-30000	9.00 ± 0.00	14000 ± 900	B5-B6	66.87 ± 15.68	$5.19^{+0.14}_{-0.22}$	<0.01	$36.19^{+8.78}_{-8.05}$
V1977 Cyg	20:47:37.5	+43:47:25	$820.69^{+8.08}_{-7.92}$	10750-11250	2.50 ± 0.00	10750 ± 125	B8	5.14 ± 0.13	$2.50^{+0.01}_{-0.01}$	$1.00^{+0.01}_{-0.07}$	$4.13^{+0.07}_{-0.10}$
V2019 Cyg	20:48:04.8	+43:47:26	$831.30^{+10.32}_{-10.07}$	10750-11250	2.50 ± 0.05 ($2.44^{+0.19}_{-0.24}$)	11250 ± 184 (11000 ± 250)	B8	4.30 ± 0.20	$2.43^{+0.03}_{-0.03}$	$1.21^{+0.21}_{-0.13}$	$3.80^{+0.08}_{-0.14}$
HBC 705	20:51:02.7	+43:49:32	$2167.43^{+58.86}_{-55.83}$	16000-25000	5.50 ± 0.00	20000 ± 559	B2	7.02 ± 0.63	$3.85^{+0.06}_{-0.07}$	$0.11^{+0.03}_{-0.01}$	$9.28^{+0.69}_{-0.30}$
V1493 Cyg †	20:52:04.6	+44:37:30	$1090.35^{+56.72}_{-51.37}$	8500-9500	6.50 ± 0.00	9000 ± 125	A1-A2	8.67 ± 0.57	$2.65^{+0.05}_{-0.06}$	$0.42^{+0.09}_{-0.04}$	$5.20^{+0.28}_{-0.24}$
HBC 717 †	20:52:06.0	+44:17:16	$827.96^{+78.38}_{-65.90}$	6250-6500	2.50 ± 0.00	6250 ± 125	F5-F8	4.09 ± 0.39	$1.36^{+0.07}_{-0.08}$	$3.00^{+1.00}_{-0.79}$	$2.43^{+0.27}_{-0.22}$
HD 199603	20:58:41.8	-14:29:00	$89.04^{+0.35}_{-0.34}$	7000-7500	0.00 ± 0.00	7500 ± 125	A7-A9	2.93 ± 0.10	$1.39^{+0.01}_{-0.01}$	$5.19^{+0.54}_{-0.19}$	$2.10^{+0.04}_{-0.05}$
HD 200775	21:01:36.9	+68:09:48	$352.40^{+4.70}_{-4.58}$	16000-22000	2.00 ± 0.00 ($1.85^{+0.15}_{-0.17}$)	16000 ± 500 (19000 ± 3000)	B4	6.69 ± 0.43	$3.42^{+0.01}_{-0.01}$	$0.22^{+0.03}_{-0.02}$	$7.01^{+0.09}_{-0.01}$
LkHa 324	21:03:54.2	+50:15:10	$620.61^{+3.55}_{-3.51}$	12000-13000	3.50 ± 0.05 ($3.94^{+0.14}_{-0.16}$)	12000 ± 125 (12500 ± 500)	B7-B8	2.62 ± 0.10	$2.11^{+0.03}_{-0.03}$	$1.99^{+0.51}_{-0.09}$	$3.19^{+0.24}_{-0.00}$
HD 235495	21:21:27.5	+50:59:48	$511.40^{+3.91}_{-3.85}$	9500-10750	1.00 ± 0.00	9750 ± 134	B9	3.21 ± 0.11	$1.93^{+0.02}_{-0.02}$	$2.99^{+0.01}_{-0.07}$	$2.78^{+0.02}_{-0.07}$
AS 470	21:36:14.2	+57:21:31	$9102.29^{+817.30}_{-807.02}$	7500-9750	2.50 ± 0.23	8000 ± 228	A4-A7	42.78 ± 7.73	$3.83^{+0.13}_{-0.18}$	$0.02^{+0.01}_{-0.01}$	$13.29^{+0.75}_{-1.44}$
GSC 3975-0579	21:38:08.5	+57:26:48	$901.32^{+11.07}_{-10.80}$	8500-9500	1.00 ± 0.00	9250 ± 125	A0-A1	2.53 ± 0.08	$1.62^{+0.01}_{-0.02}$	$4.74^{+0.14}_{-0.27}$	$2.29^{+0.01}_{-0.04}$
V361 Cep	21:42:50.2	+66:06:35	$882.10^{+10.66}_{-10.40}$	16000-18000	2.00 ± 0.00 ($1.97^{+0.14}_{-0.15}$)	16000 ± 500 (16750 ± 500)	B4	4.57 ± 0.29	$3.09^{+0.01}_{-0.01}$	$0.50^{+0.01}_{-0.03}$	$5.54^{+0.06}_{-0.11}$
V373 Cep	21:43:06.8	+66:06:54	$872.52^{+15.44}_{-14.91}$	10250-12750	3.50 ± 0.00 ($3.24^{+0.20}_{-0.23}$)	12750 ± 125 (11500 ± 1250)	B7	3.32 ± 0.10	$2.42^{+0.02}_{-0.02}$	$1.43^{+0.14}_{-0.10}$	$3.60^{+0.04}_{-0.00}$
AS 477	21:52:34.1	+47:13:44	$758.32^{+7.13}_{-6.99}$	10000-11000	1.50 ± 0.22 ($1.46^{+0.08}_{-0.08}$)	10250 ± 344 (10500 ± 500)	B8-B9	4.75 ± 0.84	$2.35^{+0.12}_{-0.17}$	$1.19^{+0.79}_{-0.28}$	$3.78^{+0.42}_{-0.56}$
LkHa 257	21:54:18.8	+47:12:10	$784.36^{+8.38}_{-8.20}$	9000-9500	2.00 ± 0.00 ($2.28^{+0.07}_{-0.08}$)	9000 ± 125 (9250 ± 250)	A1-A2	1.69 ± 0.05	$1.23^{+0.01}_{-0.01}$	$10.00^{+1.21}_{-0.41}$	$1.95^{+0.03}_{-0.00}$
BH Cep	22:01:42.9	+69:44:36	$323.94^{+1.19}_{-1.18}$	6250-6750	1.00 ± 0.25	6750 ± 251	F1-F4	1.83 ± 0.21	$0.80^{+0.07}_{-0.08}$	$13.49^{+5.72}_{-3.04}$	$1.49^{+0.06}_{-0.07}$
BO Cep	22:16:54.1	+70:03:45	$367.93^{+1.96}_{-1.94}$	6500-6750	0.50 ± 0.00	6500 ± 125	F3-F5	1.62 ± 0.06	$0.63^{+0.01}_{-0.01}$	$16.74^{+2.30}_{-3.02}$	$1.35^{+0.04}_{-0.00}$
SV Cep	22:21:33.2	+73:40:27	$340.32^{+1.66}_{-1.65}$	7500-8500	1.50 ± 0.19 ($0.78^{+0.04}_{-0.05}$)	8500 ± 189 (8000 ± 500)	A3-A4	2.11 ± 0.18	$1.32^{+0.06}_{-0.07}$	$6.46^{+0.55}_{-0.50}$	$2.00^{+0.10}_{-0.04}$
MWC 655	22:38:31.8	+55:50:05	$1881.25^{+46.73}_{-44.52}$	19000-29000	1.50 ± 0.07	19000 ± 500	B2-B3	9.70 ± 0.72	$4.04^{+0.04}_{-0.05}$	$0.08^{+0.01}_{-0.02}$	$11.00^{+0.52}_{-0.37}$
IL Cep	22:53:15.6	+62:08:45	$797.43^{+8.76}_{-8.57}$	20000-23000	3.00 ± 0.00 ($2.86^{+0.13}_{-0.15}$)	20000 ± 500 (21500 ± 1000)	B2	7.87 ± 0.40	$3.95^{+0.01}_{-0.01}$	$0.09^{+0.01}_{-0.01}$	$10.02^{+0.10}_{-0.02}$
V374 Cep	23:05:07.5	+62:15:36	$825.85^{+8.57}_{-8.39}$	14000-17000	3.00 ± 0.53 ($3.20^{+0.15}_{-0.18}$)	16000 ± 1450 (15500 ± 1000)	B3-B5	6.56 ± 2.67	$3.40^{+0.24}_{-0.57}$	$0.23^{+0.55}_{-0.11}$	$7.00^{+1.58}_{-2.21}$
MWC 1080	23:17:25.6	+60:50:43	$1424.30^{+64.04}_{-58.76}$	26000-36000	5.00 ± 0.19 ($5.05^{+0.36}_{-0.55}$)	28000 ± 1735 (31000 ± 5000)	B0	9.03 ± 1.72	$4.66^{+0.11}_{-0.15}$	$0.03^{+0.01}_{-0.01}$	$17.97^{+1.91}_{-2.03}$
BP Psc †	23:22:24.7	-02:13:42	$211.39^{+28.74}_{-18.22}$	5250-5500	1.00 ± 0.32	5250 ± 125	G9-K0	1.92 ± 0.47	$0.40^{+0.17}_{-0.28}$	$4.89^{+8.26}_{-2.75}$	$1.65^{+0.24}_{-0.43}$
LkHa 259	23:58:41.6	+66:26:13	$701.84^{+7.31}_{-7.16}$	7000-7500	5.00 ± 0.00	7500 ± 125	A7-A9	3.65 ± 0.13	$1.58^{+0.01}_{-0.01}$	$3.64^{+0.32}_{-0.34}$	$2.41^{+0.09}_{-0.02}$

Table B.2. SED classifications and disk parameters.

Object	Meeus group	*JH-K* group	Log($\dot{M}_{\rm acc}$) ($M_\odot$yr^{-1})	Log($L_{\rm acc}$) ($L_\odot$)	$M_{\rm disk}^{\rm min}$ ($M_\odot$)	IR$_{\rm start}$ (μm)	$r_{\rm in}$ (au)	Notes
HBC 1	I	*J*	$-5.07^{+1.13}_{-1.14}$	$1.88^{+0.76}_{-0.83}$	1.278	1.24	0.92 ± 0.08	
MQ Cas	II	*J*	$-6.28^{+0.34}_{-0.38}$	$0.98^{+0.31}_{-0.31}$	0.392	1.24	0.29 ± 0.03	
VX Cas	II	*J*	$-6.80^{+0.30}_{-0.30}$	$0.57^{+0.28}_{-0.27}$	0.529	1.24	0.19 ± 0.02	*
V594 Cas	II	*J*	$-5.66^{+0.45}_{-0.45}$	$1.58^{+0.38}_{-0.39}$	0.516	1.24	0.58 ± 0.05	
HBC 7		*K*s	$-4.93^{+0.66}_{-0.63}$	$2.43^{+0.60}_{-0.59}$	0.247	2.16	6.09 ± 0.49	
PDS 2	I	*J*	$-7.25^{+0.20}_{-0.21}$	$-0.08^{+0.03}_{-0.18}$	0.230	1.24	0.09 ± 0.01	
HD 9672	II	> *K*s	$-6.96^{+0.25}_{-0.25}$	$0.37^{+0.23}_{-0.23}$	0.005	8.23	1.82 ± 0.61	
HD 17081	II	>*K*s	$-5.45^{+0.56}_{-0.55}$	$1.80^{+0.51}_{-0.51}$	0.823	8.23	10.40 ± 3.46	
BD+30 549	I	*J*	$-6.64^{+0.40}_{-0.44}$	$0.75^{+0.35}_{-0.35}$	0.049	1.24	0.23 ± 0.02	
PDS 4	I	*H*	$-6.91^{+0.25}_{-0.24}$	$0.45^{+0.22}_{-0.22}$	0.332	1.66	0.24 ± 0.02	*
IP Per	I	*J*	$-7.26^{+0.22}_{-0.23}$	$0.01^{+0.20}_{-0.19}$	0.234	1.24	0.10 ± 0.01	*
XY Per A	II	*J*	$-5.62^{+0.49}_{-0.55}$	$1.52^{+0.40}_{-0.46}$	1.118	1.24	0.53 ± 0.05	
AB Aur	I	*J*	$-6.34^{+0.28}_{-0.27}$	$0.84^{+0.25}_{-0.25}$	0.501	1.24	0.25 ± 0.02	
HD 31648	II	*J*	$-6.81^{+0.24}_{-0.24}$	$0.39^{+0.22}_{-0.22}$	0.559	1.24	0.15 ± 0.01	
UX Ori	II	*J*	$-7.00^{+0.43}_{-0.49}$	$0.28^{+0.36}_{-0.18}$	0.143	1.24	0.13 ± 0.01	
HD 34282	I	*J*	>−7.28	>0.10	0.116	1.24	0.14 ± 0.01	
HD 34700	I	*K*s	$-6.50^{+0.26}_{-0.27}$	$0.53^{+0.23}_{-0.23}$	0.451	2.16	0.35 ± 0.03	
HD 290380	II	*J*	$-7.16^{+0.22}_{-0.22}$	$-0.04^{+0.11}_{-0.18}$	0.367	1.24	0.09 ± 0.01	
HD 35187	II	*J*	$-6.73^{+0.41}_{-0.47}$	$0.59^{+0.35}_{-0.37}$	0.290	1.24	0.19 ± 0.02	*
HD 287823	I	*J*	$-7.05^{+0.23}_{-0.23}$	$0.24^{+0.21}_{-0.21}$	0.171	1.24	0.13 ± 0.01	
V346 Ori	I	*H*	$-7.25^{+0.22}_{-0.22}$	$0.02^{+0.19}_{-0.16}$	0.249	1.66	0.14 ± 0.01	*
HD 290409	I	*J*	$-6.80^{+0.26}_{-0.27}$	$0.57^{+0.24}_{-0.25}$	0.174	1.24	0.18 ± 0.02	*
CO Ori	II	*J*	$-6.51^{+0.49}_{-0.52}$	$0.53^{+0.35}_{-0.38}$	0.445	1.24	0.17 ± 0.02	
HD 35929	II	*K*s	$-5.86^{+0.32}_{-0.32}$	$1.16^{+0.29}_{-0.29}$	0.833	2.16	0.73 ± 0.06	
HD 290500	I	*H*	$-7.07^{+0.30}_{-0.31}$	$0.26^{+0.26}_{-0.26}$	0.288	1.66	0.19 ± 0.02	
HD 244314	II	*J*	$-6.84^{+0.26}_{-0.25}$	$0.46^{+0.24}_{-0.23}$	0.136	1.24	0.16 ± 0.01	
HD 36112	I	*J*	$-7.11^{+0.22}_{-0.23}$	$0.10^{+0.20}_{-0.00}$	0.315	1.24	0.11 ± 0.01	
HD 244604	II	*J*	$-6.48^{+0.27}_{-0.28}$	$0.71^{+0.25}_{-0.25}$	0.618	1.24	0.21 ± 0.02	
RY Ori	II	*J*	$-7.17^{+0.37}_{-0.38}$	$-0.05^{+0.18}_{-0.28}$	0.362	1.24	0.09 ± 0.01	
HD 36408	II	>*K*s	$-5.18^{+0.56}_{-0.55}$	$2.01^{+0.53}_{-0.52}$	0.596	10.15	20.73 ± 8.27	
HD 288012	I	>*K*s	$-7.00^{+0.23}_{-0.23}$	$0.31^{+0.21}_{-0.21}$	0.179	3.35	0.52 ± 0.07	*
HBC 442	I	*J*	$-6.93^{+0.28}_{-0.27}$	$0.16^{+0.22}_{-0.10}$	0.405	1.24	0.11 ± 0.01	
HD 36917	II	*J*	$-5.43^{+0.53}_{-0.52}$	$1.76^{+0.50}_{-0.49}$	0.968	1.24	0.75 ± 0.07	
HD 245185	I	*J*	$-6.71^{+0.26}_{-0.27}$	$0.65^{+0.25}_{-0.25}$	0.221	1.24	0.20 ± 0.02	*
HD 36982	I	>*K*s	>−6.10	>1.54	0.077	10.15	24.16 ± 9.64	*
NV Ori	I	*H*	$-6.58^{+0.29}_{-0.28}$	$0.05^{+0.25}_{-0.24}$	0.685	1.66	0.24 ± 0.03	
T Ori		*J*	$-6.23^{+0.44}_{-0.46}$	$0.95^{+0.35}_{-0.36}$	0.453	1.24	0.28 ± 0.02	
CQ Tau	I	*H*	$-7.18^{+0.21}_{-0.20}$	$-0.03^{+0.14}_{-0.19}$	0.303	1.66	0.14 ± 0.01	
V380 Ori	I?	*J*	$-6.04^{+0.66}_{-1.05}$	$1.17^{+0.52}_{-0.77}$	0.379	1.24	0.36 ± 0.03	
HD 37258	II	*J*	$-6.73^{+0.28}_{-0.26}$	$0.58^{+0.25}_{-0.24}$	0.274	1.24	0.19 ± 0.02	*

Notes. For the stars with an asterisk in the last column, accretion-based disk masses have been reestimated because $t_* > t_{\rm MS}$ (Sect. 2.2.3).

Table B.2. continued.

Object	Meeus group	*JH-K* group	Log($\dot{M}_{\rm acc}$) ($M_\odot {\rm yr}^{-1}$)	Log($L_{\rm acc}$) ($L_\odot$)	$M_{\rm disk}^{\rm min}$ ($M_\odot$)	IR$_{\rm start}$ (μm)	$r_{\rm in}$ (au)	Notes
HD 290770	II	*J*	$-6.43^{+0.28}_{-0.29}$	$0.92^{+0.26}_{-0.26}$	0.045	1.24	0.27 ± 0.02	
BF Ori	II	*J*	$-7.03^{+0.35}_{-0.41}$	$0.29^{+0.30}_{-0.27}$	0.507	1.24	0.13 ± 0.01	*
HD 37357	II	*J*	$-6.06^{+0.43}_{-0.44}$	$1.13^{+0.35}_{-0.36}$	0.362	1.24	0.34 ± 0.03	
HD 290764	I	*J*	$-6.63^{+0.26}_{-0.26}$	$0.51^{+0.24}_{-0.24}$	0.715	1.24	0.17 ± 0.02	
V1787 Ori	I	*J*	$-6.57^{+0.25}_{-0.26}$	$0.61^{+0.24}_{-0.23}$	0.648	1.24	0.19 ± 0.02	
HD 37371		>*K*s	$-6.16^{+0.32}_{-0.31}$	$1.19^{+0.29}_{-0.29}$	0.627	4.60	2.16 ± 0.33	*
V599 Ori	I	*J*	$-6.49^{+0.35}_{-0.35}$	$0.66^{+0.30}_{-0.30}$	0.638	1.24	0.20 ± 0.02	
RR Tau	II	*H*	$-5.78^{+0.46}_{-0.46}$	$1.38^{+0.37}_{-0.38}$	0.368	1.66	0.67 ± 0.07	
HD 245906	I	*J*	$-5.85^{+0.81}_{-0.74}$	$1.19^{+0.51}_{-0.47}$	0.697	1.24	0.36 ± 0.03	
V350 Ori	II	*J*	>−8.06	>−0.48	0.019	1.24	0.11 ± 0.01	
HD 37806	II	*J*	$-5.69^{+0.35}_{-0.34}$	$1.50^{+0.32}_{-0.31}$	0.513	1.24	0.52 ± 0.05	
HD 38087	I	*J*	$-5.67^{+0.46}_{-0.54}$	$1.71^{+0.38}_{-0.49}$	0.083	1.24	0.71 ± 0.06	
HD 38120	I	*J*	$-6.34^{+0.30}_{-0.30}$	$1.04^{+0.28}_{-0.28}$	0.096	1.24	0.31 ± 0.03	*
V351 Ori	I	*J*	$-6.63^{+0.42}_{-0.43}$	$0.49^{+0.33}_{-0.33}$	0.723	1.24	0.16 ± 0.01	
HD 39014	II	>*K*s	$-6.27^{+0.28}_{-0.28}$	$0.84^{+0.25}_{-0.25}$	0.606	51.99	35.41 ± 13.87	
UCAC4 552-019438	I	*J*	$-5.84^{+0.39}_{-0.41}$	$1.43^{+0.36}_{-0.35}$	0.413	1.24	0.49 ± 0.04	
V1818 Ori	I	*H*	$-5.39^{+0.64}_{-0.64}$	$1.79^{+0.54}_{-0.55}$	0.854	1.66	1.19 ± 0.12	
HD 249879	II	*H*	>−6.98	>0.45	0.198	1.66	0.32 ± 0.03	
HD 250550	I	*J*	$-5.82^{+0.37}_{-0.38}$	$1.39^{+0.33}_{-0.33}$	0.433	1.24	0.46 ± 0.04	
PDS 22	I	*H*	$-6.37^{+0.30}_{-0.35}$	$0.87^{+0.28}_{-0.28}$	0.408	1.66	0.38 ± 0.04	
HD 41511	II	*J*	$-4.82^{+0.67}_{-0.69}$	$2.15^{+0.59}_{-0.59}$	1.329	1.24	1.57 ± 0.14	
PDS 124	I	*H*	$-6.59^{+0.28}_{-0.27}$	$0.77^{+0.26}_{-0.26}$	0.082	1.66	0.34 ± 0.04	*
GSC 1876-0892	I	*H*	$-4.28^{+0.82}_{-0.83}$	$2.85^{+0.70}_{-0.70}$	1.168	166	9.42 ± 0.95	
LkHa 208	I	*J*	$-6.98^{+0.36}_{-0.39}$	$0.18^{+0.29}_{-0.06}$	0.464	1.24	0.12 ± 0.01	
LKHa 338		*J*	$-6.32^{+0.31}_{-0.31}$	$0.94^{+0.28}_{-0.28}$	0.235	1.24	0.28 ± 0.03	
LkHa 339	I	*H*	$-6.54^{+0.28}_{-0.28}$	$0.80^{+0.25}_{-0.25}$	0.156	1.66	0.36 ± 0.04	*
PDS 126	II	*J*	$-6.53^{+0.27}_{-0.27}$	$0.59^{+0.25}_{-0.24}$	0.719	1.24	0.19 ± 0.02	
MWC 137	I	*H*	$-3.93^{+0.87}_{-0.87}$	$3.45^{+0.77}_{-0.77}$	2.614	1.66	30.88 ± 3.11	
CPM 25	I	*J*	$-5.12^{+0.82}_{-0.85}$	$2.22^{+0.65}_{-0.68}$	0.641	1.24	1.89 ± 0.17	
HD 46060	II	>*K*s	$-5.02^{+0.61}_{-0.61}$	$2.30^{+0.56}_{-0.56}$	0.859	10.15	36.64 ± 14.62	
PDS 129	I	*H*	$-6.83^{+0.24}_{-0.24}$	$0.26^{+0.21}_{-0.21}$	0.623	1.66	0.19 ± 0.02	
VY Mon	I	*J*	$-5.59^{+0.60}_{-0.77}$	$1.71^{+0.49}_{-0.61}$	1.126	1.24	0.67 ± 0.06	
LkHa 215	I	*J*	$-5.44^{+0.67}_{-0.68}$	$1.90^{+0.57}_{-0.57}$	0.271	1.24	1.01 ± 0.09	
HD 259431	I	*J*	$-5.25^{+0.59}_{-0.60}$	$1.94^{+0.54}_{-0.53}$	0.289	1.24	1.08 ± 0.09	
HBC 217	I	*J*	$-7.15^{+0.23}_{-0.23}$	$-0.03^{+0.14}_{-0.19}$	0.341	1.24	0.09 ± 0.01	
HBC 222		*J*	$-6.97^{+0.32}_{-0.33}$	$0.13^{+0.25}_{-0.00}$	0.511	1.24	0.11 ± 0.01	
PDS 24	I	*J*	>−7.15	>0.27	0.316	1.24	0.17 ± 0.02	
PDS 130	I	*J*	$-6.18^{+0.34}_{-0.33}$	$1.09^{+0.30}_{-0.29}$	0.360	1.24	0.33 ± 0.03	
HD 50083	II	>*K*s	$-4.56^{+0.68}_{-0.68}$	$2.66^{+0.63}_{-0.62}$	1.023	3.35	16.70 ± 2.20	
PDS 25	I	*J*	$-7.09^{+0.38}_{-0.44}$	$0.20^{+0.32}_{-0.08}$	0.904	1.24	0.12 ± 0.01	*
PDS 229N	I	*H*	$-4.80^{+1.06}_{-1.14}$	$2.31^{+0.72}_{-0.85}$	0.867	1.66	3.25 ± 0.33	
HT CMa	II?	*J*	$-6.05^{+0.31}_{-0.30}$	$1.15^{+0.29}_{-0.29}$	0.370	1.24	0.35 ± 0.03	
Z CMa	I	*H*	$-4.68^{+1.06}_{-1.14}$	$2.19^{+0.71}_{-0.86}$	1.081	1.66	2.51 ± 0.25	

Table B.2. continued.

Object	Meeus group	*JH-K* group	Log($\dot{M}_{\rm acc}$) ($M_\odot$yr^{-1})	Log($L_{\rm acc}$) ($L_\odot$)	$M_{\rm disk}^{\rm min}$ ($M_\odot$)	IR$_{\rm start}$ (μm)	$r_{\rm in}$ (au)	Notes
HU CMa	I	*J*	$-6.20^{+0.41}_{-0.45}$	$1.21^{+0.36}_{-0.37}$	0.655	1.24	0.39 ± 0.03	*
PDS 241	I	>*K*s	$-4.46^{+0.81}_{-0.80}$	$2.97^{+0.70}_{-0.70}$	0.747	3.35	31.51 ± 4.16	
HD 56895	II	>*K*s	$-6.98^{+0.23}_{-0.22}$	$0.14^{+0.20}_{-0.08}$	0.499	10.15	1.80 ± 0.72	
PDS 27	I	*J*	$-4.56^{+0.79}_{-0.78}$	$2.59^{+0.66}_{-0.66}$	1.087	1.24	3.84 ± 0.34	
GSC 6546-3156	I	*H*	$-6.81^{+0.31}_{-0.32}$	$0.52^{+0.27}_{-0.27}$	0.093	1.66	0.26 ± 0.03	
PDS 133	I	*J*	$-6.30^{+0.33}_{-0.37}$	$1.09^{+0.30}_{-0.31}$	0.164	1.24	0.33 ± 0.03	*
HD 58647	II	*H*	$-5.48^{+0.35}_{-0.50}$	$1.68^{+0.33}_{-0.47}$	1.317	1.66	0.97 ± 0.10	
HD 59319	I	>*K*s	$-5.49^{+0.36}_{-0.53}$	$1.74^{+0.33}_{-0.51}$	1.313	10.15	11.43 ± 4.56	
PDS 134	I	>*K*s	$-5.38^{+0.55}_{-0.55}$	$1.86^{+0.51}_{-0.51}$	0.751	4.60	5.33 ± 0.81	
GSC 8143-1225	I	*J*	>−9.38	>−1.73	0.062	1.24	0.06 ± 0.01	
HD 68695	I	*H*	$-6.81^{+0.26}_{-0.26}$	$0.52^{+0.24}_{-0.24}$	0.093	1.66	0.26 ± 0.03	
PDS 277	I	*J*	$-6.96^{+0.23}_{-0.23}$	$0.14^{+0.20}_{-0.08}$	0.527	1.24	0.11 ± 0.01	
V388 Vel	I	>*K*s	$-5.85^{+0.37}_{-0.36}$	$1.32^{+0.32}_{-0.32}$	0.404	3.35	1.63 ± 0.21	
GSC 8581-2002	I	>*K*s	$-6.64^{+0.27}_{-0.25}$	$0.70^{+0.24}_{-0.24}$	0.023	10.15	3.51 ± 1.40	
PDS 33	I	*J*	>−7.11	>0.27	0.168	1.24	0.17 ± 0.02	
PDS 34	I	*J*	$-5.73^{+0.54}_{-0.57}$	$1.75^{+0.51}_{-0.50}$	0.450	1.24	0.76 ± 0.07	*
HD 76534		>*K*s	$-4.98^{+0.66}_{-0.65}$	$2.43^{+0.60}_{-0.59}$	0.216	3.35	10.93 ± 1.44	
SAO 220669	I	>*K*s	$-4.81^{+0.66}_{-0.66}$	$2.42^{+0.60}_{-0.60}$	0.624	10.15	46.55 ± 18.57	
PDS 286	II	*J*	$-4.26^{+0.74}_{-0.74}$	$3.23^{+0.70}_{-0.70}$	1.223	1.24	13.77 ± 1.21	
PDS 297		>*K*s	$-5.77^{+0.34}_{-0.33}$	$1.45^{+0.31}_{-0.31}$	0.299	11.56	9.76 ± 3.10	
HD 87403		>*K*s	$-5.20^{+0.57}_{-0.56}$	$1.89^{+0.52}_{-0.52}$	0.669	22.09	44.70 ± 5.54	
HD 87643	I	*J*	$-4.28^{+1.07}_{-1.15}$	$2.85^{+0.77}_{-0.87}$	1.168	1.24	6.30 ± 0.55	
PDS 37	I	*H*	$-4.87^{+0.67}_{-0.68}$	$2.48^{+0.61}_{-0.61}$	0.538	1.66	4.68 ± 0.47	
HD 305298	I	>*K*s	$-4.64^{+0.84}_{-0.80}$	$3.10^{+0.73}_{-0.73}$	0.399	3.35	42.05 ± 5.55	
PDS 322		*K*s	$-4.97^{+0.94}_{-1.01}$	$2.46^{+0.72}_{-0.79}$	0.114	2.16	6.53 ± 0.53	
HD 94509		>*K*s	$-5.09^{+0.57}_{-0.57}$	$2.06^{+0.54}_{-0.54}$	0.982	3.35	5.11 ± 0.67	
PDS 324	I	*J*	$-5.32^{+0.62}_{-0.63}$	$2.15^{+0.57}_{-0.57}$	0.261	1.24	1.69 ± 0.15	
HD 95881	II	*J*	$-5.06^{+0.55}_{-0.54}$	$1.97^{+0.52}_{-0.52}$	1.239	1.24	1.12 ± 0.10	
HD 96042	I	>*K*s	$-4.35^{+0.77}_{-0.74}$	$3.15^{+0.70}_{-0.70}$	0.994	10.15	199.03 ± 79.41	
HD 97048	I	*J*	$-6.36^{+0.28}_{-0.28}$	$0.99^{+0.27}_{-0.26}$	0.102	1.24	0.30 ± 0.03	*
HD 98922	II	*J*	$-4.96^{+0.55}_{-0.55}$	$2.09^{+0.54}_{-0.53}$	1.301	1.24	1.40 ± 0.12	
HD 100453	I	*J*	$-7.32^{+0.21}_{-0.21}$	$-0.06^{+0.07}_{-0.18}$	0.096	1.24	0.09 ± 0.01	*
HD 100546	I	*J*	$-6.81^{+0.25}_{-0.25}$	$0.51^{+0.23}_{-0.23}$	0.097	1.24	0.17 ± 0.02	
HD 101412	II	*J*	$-6.35^{+0.27}_{-0.27}$	$0.87^{+0.26}_{-0.25}$	0.470	1.24	0.26 ± 0.02	
PDS 344	I	*J*	$-5.97^{+0.37}_{-0.40}$	$1.47^{+0.34}_{-0.33}$	0.164	1.24	0.52 ± 0.05	*
PDS 138	I	>*K*s	$-3.87^{+0.90}_{-0.89}$	$3.51^{+0.78}_{-0.78}$	2.395	10.15	387.92 ± 154.78	
HD 104237	II	*J*	$-6.69^{+0.29}_{-0.29}$	$0.46^{+0.26}_{-0.25}$	0.711	1.24	0.16 ± 0.01	
GSC 8645-1401	I	*J*	$-5.48^{+0.52}_{-0.76}$	$1.49^{+0.33}_{-0.58}$	1.417	1.24	0.43 ± 0.04	
Hen 2-80	I	*J*	$-4.23^{+1.37}_{-1.57}$	$2.86^{+0.82}_{-1.17}$	1.310	1.24	6.45 ± 0.57	
Hen 3-823		*K*s	$-5.15^{+0.71}_{-0.71}$	$2.15^{+0.60}_{-0.60}$	0.776	2.16	3.49 ± 0.28	
PDS 361S	I	*J*	$-5.26^{+0.58}_{-0.58}$	$2.10^{+0.55}_{-0.54}$	0.439	1.24	1.52 ± 0.13	
GSC 8994-3902		>*K*s	$-5.10^{+0.60}_{-0.61}$	$2.19^{+0.56}_{-0.56}$	0.764	3.35	6.84 ± 0.90	
PDS 364	I	*J*	$-5.15^{+1.17}_{-1.08}$	$1.98^{+0.84}_{-0.80}$	0.754	1.24	1.15 ± 0.10	

Table B.2. continued.

Object	Meeus group	*JH-K* group	Log($\dot{M}_{\rm acc}$) ($M_\odot {\rm yr}^{-1}$)	Log($L_{\rm acc}$) ($L_\odot$)	$M_{\rm disk}^{\rm min}$ ($M_\odot$)	IR$_{\rm start}$ (μm)	$r_{\rm in}$ (au)	Notes
Hen 3-938	II	*J*	$-4.08^{+0.84}_{-0.82}$	$3.51^{+0.76}_{-0.75}$	1.851	1.24	24.04 ± 2.11	
PDS 69	I	*H*	$-5.37^{+0.69}_{-0.71}$	$1.99^{+0.58}_{-0.59}$	1.028	1.66	1.80 ± 0.18	*
DG Cir	I	*J*	$-5.76^{+0.46}_{-0.48}$	$1.32^{+0.38}_{-0.38}$	0.723	1.24	0.42 ± 0.04	
HD 132947	II	>*K*s	$-6.33^{+0.28}_{-0.28}$	$0.98^{+0.27}_{-0.26}$	0.273	10.15	4.87 ± 1.94	*
PDS 389	I	*H*	$-5.81^{+0.34}_{-032}$	$1.30^{+0.30}_{-0.30}$	0.396	1.66	0.61 ± 0.06	
HD 135344B	I	*J*	$-7.28^{+0.21}_{-0.22}$	$-0.14^{+0.10}_{-0.18}$	0.346	1.24	0.08 ± 0.01	
HD 135344		>*K*s	$-6.94^{+0.22}_{-0.23}$	$0.19^{+0.20}_{-0.18}$	0.533	22.09	5.42 ± 0.67	
HD 139614	I	*H*	$-7.29^{+0.20}_{-0.21}$	$-0.02^{+0.16}_{-0.19}$	0.152	1.66	0.14 ± 0.01	*
HD 141569	II	>*K*s	$-6.77^{+0.25}_{-0.25}$	$0.57^{+0.23}_{-0.23}$	0.005	3.35	0.69 ± 0.09	
HD 141926	II	*J*	$-4.54^{+0.72}_{-0.72}$	$2.95^{+0.66}_{-0.66}$	0.621	1.24	8.08 ± 0.71	
HD 142666	II	*H*	$-6.84^{+0.23}_{-0.23}$	$0.29^{+0.21}_{-0.21}$	0.589	1.66	0.19 ± 0.02	
HD 142527	I	*J*	$-6.54^{+0.26}_{-0.25}$	$0.52^{+0.23}_{-0.23}$	0.532	1.24	0.17 ± 0.02	
Hen 3-1121	I	*J*	$-4.80^{+0.86}_{-0.86}$	$2.63^{+0.71}_{-0.71}$	0.519	1.24	4.25 ± 0.37	
Hen 3-1121S		>*K*s	$-4.58^{+0.96}_{-1.03}$	$3.03^{+0.77}_{-0.81}$	0.567	10.15	156.97 ± 62.63	
HD 143006	I	*J*	$-7.50^{+0.23}_{-0.22}$	$-0.31^{+0.18}_{-0.17}$	0.162	1.24	0.07 ± 0.01	
HD 144432	II	*J*	$-6.79^{+0.24}_{-0.24}$	$0.38^{+0.22}_{-0.22}$	0.611	1.24	0.14 ± 0.01	
HR 5999	II	*H*	$-5.92^{+0.44}_{-0.43}$	$1.16^{+0.36}_{-0.35}$	0.374	1.66	0.52 ± 0.05	
WRAY 15-1435	I	*J*	$-4.83^{+0.67}_{-0.65}$	$2.51^{+0.61}_{-0.61}$	0.494	1.24	3.37 ± 0.30	
V718 Sco	II	*K*s	$-6.93^{+0.26}_{-0.27}$	$0.24^{+0.23}_{-0.23}$	0.508	2.16	0.26 ± 0.02	
Hen 3-1191	II	*J*	$-5.19^{+0.68}_{-0.71}$	$2.42^{+0.63}_{-0.62}$	0.674	1.24	2.89 ± 0.25	*
HD 149914	II	>*K*s	$-5.91^{+0.30}_{-0.31}$	$1.24^{+0.29}_{-0.28}$	0.461	8.23	4.87 ± 1.62	
HD 150193	II	*J*	$-6.78^{+0.26}_{-0.24}$	$0.53^{+0.23}_{-0.23}$	0.182	1.24	0.18 ± 0.02	*
AK Sco	II	*H*	$-7.23^{+0.41}_{-0.43}$	$-0.10^{+0.09}_{-0.29}$	0.314	1.66	0.12 ± 0.01	
PDS 431	I	>*K*s	$-6.10^{+0.33}_{-0.32}$	$1.11^{+0.30}_{-0.29}$	0.536	10.15	5.53 ± 2.21	
V921 Sco	I	*J*	$-4.32^{+0.86}_{-0.82}$	$3.15^{+0.73}_{-0.73}$	1.065	1.24	11.75 ± 1.03	
HD 155448	I	>*K*s	$-5.27^{+0.56}_{-0.56}$	$1.88^{+0.52}_{-0.52}$	0.263	3.35	3.61 ± 0.48	
MWC 878	II	*J*	$-4.54^{+0.72}_{-0.73}$	$3.00^{+0.68}_{-0.68}$	0.621	1.24	8.99 ± 0.79	
HD 319896	I	*K*s	$-5.14^{+0.59}_{-0.59}$	$2.13^{+0.55}_{-0.54}$	0.827	2.16	3.33 ± 0.27	
HD 158643	II	*K*s	$-5.67^{+0.32}_{-0.32}$	$1.45^{+0.30}_{-0.30}$	1.017	2.16	1.03 ± 0.08	
HD 323771	II	*J*	$-5.67^{+0.67}_{-0.72}$	$1.71^{+0.51}_{-0.59}$	0.102	1.24	0.71 ± 0.06	
SAO 185668	I	>*K*s	$-4.81^{+0.67}_{-0.69}$	$2.45^{+0.61}_{-0.61}$	0.620	7.95	35.74 ± 10.10	
MWC 593	I?	*J*	$-4.78^{+0.62}_{-0.63}$	$2.41^{+0.59}_{-0.58}$	0.669	1.24	2.70 ± 0.24	
PDS 469	I	*J*	$-6.39^{+0.40}_{-0.41}$	$0.84^{+0.33}_{-0.34}$	0.455	1.24	0.25 ± 0.02	
HD 163296	II	*J*	$-6.95^{+0.27}_{-0.31}$	$0.36^{+0.25}_{-0.25}$	0.145	1.24	0.14 ± 0.01	
PDS 477	I	*J*	$-4.58^{+1.04}_{-1.13}$	$2.70^{+0.75}_{-0.85}$	0.947	1.24	4.88 ± 0.43	
HD 313571		*K*s	$-4.76^{+0.67}_{-0.66}$	$2.46^{+0.61}_{-0.60}$	0.607	2.16	6.40 ± 0.52	
LKHa 260	II	*H*	$-5.60^{+0.62}_{-0.72}$	$1.74^{+0.51}_{-0.58}$	0.857	1.66	1.10 ± 0.11	
HD 169142	I	*J*	$-7.35^{+0.20}_{-0.20}$	$-0.09^{+0.01}_{-0.18}$	0.278	1.24	0.09 ± 0.01	
MWC 297	I	*J*	$-4.42^{+0.70}_{-0.69}$	$3.06^{+0.67}_{-0.67}$	0.846	1.24	9.89 ± 0.87	
VV Ser	II	*J*	$-5.92^{+0.55}_{-0.67}$	$1.51^{+0.46}_{-0.50}$	0.231	1.24	0.54 ± 0.05	*
V431 Sct	II	*H*	$-4.73^{+0.66}_{-0.67}$	$2.65^{+0.63}_{-0.62}$	0.671	1.66	6.61 ± 0.67	
PDS 520	I	*J*	$-7.06^{+0.50}_{-0.73}$	$0.07^{+0.39}_{-0.38}$	0.459	1.24	0.10 ± 0.01	
AS 310	I	>*K*s	$-4.82^{+0.71}_{-0.72}$	$2.79^{+0.66}_{-0.65}$	0.262	10.15	100.50 ± 40.10	

Table B.2. continued.

Object	Meeus group	*JH-K* group	Log($\dot{M}_{\rm acc}$) ($M_\odot$yr^{-1})	Log($L_{\rm acc}$) ($L_\odot$)	$M_{\rm disk}^{\rm min}$ ($M_\odot$)	IR$_{\rm start}$ (μm)	$r_{\rm in}$ (au)	Notes
PDS 530	I	*H*	$-7.18^{+0.61}_{-1.07}$	$0.11^{+0.46}_{-0.59}$	0.275	1.66	0.16 ± 0.02	*
MWC 953		*J*	$-4.51^{+0.79}_{-0.82}$	$2.66^{+0.67}_{-0.68}$	1.135	1.24	4.35 ± 0.38	
PDS 543	I	>*K*s	$-4.34^{+0.78}_{-0.75}$	$3.24^{+0.71}_{-0.70}$	1.017	3.35	53.79 ± 7.09	
HD 174571	II	>*K*s	$-4.49^{+0.71}_{-0.69}$	$2.88^{+0.66}_{-0.66}$	0.564	7.95	83.57 ± 23.61	
HD 176386		>*K*s	$-6.49^{+0.31}_{-0.26}$	$0.82^{+0.25}_{-0.25}$	0.093	3.35	0.92 ± 0.12	
TY CrA	I	*J*	$-6.72^{+0.66}_{-1.09}$	$075^{+0.51}_{-0.65}$	0.826	1.24	0.23 ± 0.02	*
HD 179218	I	*H*	$-5.97^{+0.30}_{-0.29}$	$1.21^{+0.28}_{-0.28}$	0.201	1.66	0.56 ± 0.06	
HD 344261		>*K*s	$-7.29^{+0.21}_{-0.21}$	$-0.07^{+0.05}_{-0.18}$	0.089	22.09	4.08 ± 0.51	*
WW Vul	II	*J*	$-6.62^{+0.32}_{-0.32}$	$0.58^{+0.28}_{-0.28}$	0.622	1.24	0.18 ± 0.02	
PX Vul	II	*J*	$-6.36^{+0.32}_{-0.30}$	$0.66^{+0.26}_{-0.26}$	0.500	1.24	0.20 ± 0.02	
PDS 581	I	*H*	$-5.06^{+0.73}_{-0.71}$	$2.34^{+0.62}_{-0.62}$	0.543	1.66	3.59 ± 0.36	
V1295 Aql	II	*J*	$-5.13^{+0.56}_{-0.55}$	$1.92^{+0.52}_{-0.52}$	1.003	1.24	1.01 ± 0.09	
V1685 Cyg	I	*J*	$-4.95^{+0.61}_{-0.62}$	$2.41^{+0.58}_{-0.58}$	0.507	1.24	2.77 ± 0.24	
V1686 Cyg	I	*J*	$-6.52^{+0.75}_{-0.92}$	$0.51^{+0.46}_{-0.38}$	0.495	1.24	0.17 ± 0.01	
MWC 1021	II	*K*s	$-3.27^{+0.87}_{-0.87}$	$3.66^{+0.79}_{-0.79}$	9.535	2.16	62.30 ± 5.04	
V1478 Cyg	II	*J*	$-3.69^{+0.98}_{-1.01}$	$3.30^{+0.78}_{-0.80}$	3.625	1.24	14.96 ± 1.31	
V1977 Cyg	II	*J*	$-5.47^{+0.50}_{-0.49}$	$1.69^{+0.48}_{-0.48}$	1.171	1.24	0.66 ± 0.06	
V2019 Cyg	I	*J*	$-5.57^{+0.37}_{-0.36}$	$1.63^{+0.34}_{-0.33}$	1.162	1.24	0.61 ± 0.05	
HBC 705		*J*	$-4.88^{+0.67}_{-0.69}$	$2.50^{+0.62}_{-0.61}$	0.408	1.24	3.32 ± 0.29	
V1493 Cyg	I	*H*	$-5.25^{+0.56}_{-0.57}$	$1.78^{+0.52}_{-0.51}$	0.670	1.66	1.14 ± 0.12	
HBC 717	I	*J*	$-6.50^{+0.38}_{-0.38}$	$0.53^{+0.30}_{-0.29}$	0.496	1.24	0.17 ± 0.02	
HD 199603	II	>*K*s	$-6.55^{+0.26}_{-0.25}$	$0.56^{+0.23}_{-0.23}$	0.685	21.73	8.09 ± 2.49	
HD 200775	I	*H*	$-5.03^{+0.58}_{-0.58}$	$2.24^{+0.55}_{-0.55}$	1.026	1.66	2.94 ± 0.30	
LkHa 324		>*K*s	$-6.04^{+0.33}_{-0.36}$	$1.30^{+0.31}_{-0.31}$	0.276	3.35	1.61 ± 0.21	
HD 235495	II	*J*	$-6.08^{+0.31}_{-0.30}$	$1.12^{+0.29}_{-0.28}$	0.389	1.24	0.34 ± 0.03	
AS 470		*K*s	$-4.26^{+0.79}_{-0.78}$	$2.49^{+0.66}_{-0.67}$	1.582	2.16	6.22 ± 0.50	
GSC 3975-0579	I?	*J*	$-6.41^{+0.27}_{-0.27}$	$0.80^{+0.25}_{-0.26}$	0.345	1.24	0.24 ± 0.02	
V361 Cep		*K*s	$-5.30^{+0.56}_{-0.56}$	$2.04^{+0.52}_{-0.52}$	0.108	2.16	2.85 ± 0.23	
V373 Cep		*J*	$-5.67^{+0.34}_{-0.34}$	$1.62^{+0.33}_{-0.32}$	0.903	1.24	0.61 ± 0.05	
AS 477	II	*J*	$-5.61^{+0.57}_{-0.63}$	$1.55^{+0.43}_{-0.50}$	1.122	1.24	0.55 ± 0.05	
LkHa 257	I	*J*	$-6.92^{+0.23}_{-0.24}$	$0.40^{+0.22}_{-0.22}$	0.086	1.24	0.15 ± 0.01	
BH Cep	II	*J*	$-7.21^{+0.32}_{-0.32}$	$-0.05^{+0.16}_{-0.25}$	0.259	1.24	0.09 ± 0.01	
BO Cep	I	*H*	$-7.40^{+0.19}_{-0.20}$	$-0.22^{+0.17}_{-0.17}$	0.255	1.66	0.11 ± 0.01	
SV Cep	II	*H*	$-6.74^{+0.33}_{-0.34}$	$0.49^{+0.28}_{-0.28}$	0.503	1.66	0.25 ± 0.03	
MWC 655	I	*J*	$-4.70^{+0.67}_{-0.67}$	$2.61^{+0.62}_{-0.62}$	0.652	1.24	4.12 ± 0.36	
IL Cep	II	>*K*s	$-4.80^{+0.62}_{-0.62}$	$2.56^{+0.59}_{-0.59}$	0.575	4.60	21.52 ± 3.25	
V374 Cep	I	*J*	$-5.05^{+1.02}_{-1.15}$	$2.23^{+0.71}_{-0.84}$	0.940	1.24	1.94 ± 0.17	
MWC 1080	I	*J*	$-4.57^{+0.85}_{-0.86}$	$2.99^{+0.72}_{-0.72}$	0.580	1.24	8.66 ± 0.76	
BP Psc	I	*J*	$-7.65^{+0.56}_{-0.59}$	$-0.46^{+0.33}_{-0.41}$	0.125	1.24	0.06 ± 0.01	
LkHa 259	I	*J*	$-6.32^{+0.27}_{-0.28}$	$0.76^{+0.25}_{-0.25}$	0.610	1.24	0.22 ± 0.02	

Table B.3. Disk masses derived by millimeter fluxes.

Object	β	T_D (K)	M_{disk} ($M_\odot$)	N° photometric points	References
HBC 1	1.0	21	7.808 ± 0.887	1	(16)
VX Cas	1.0	33	<0.007	1	(27)
V594 Cas	1.1	32	0.039 ± 0.001	2	(7) (31)
HD 9672	0.6	39	2.920E-4 ± 3.060E-5	2	(24)
AB Aur	1.2	40	0.009 ± 0.002	5	(1) (2) (3)
HD 31648	0.9	20	0.051 ± 4.410E-4	6	(1) (2) (5) (20)
UX Ori	0.8	22	0.016 ± 0.001	2	(27) (32)
HD 34282	1.5	38	0.040 ± 0.004	6	(1) (11) (16) (21)
HD 34700	1.1	28	0.008 ± 0.001	4	(8) (11) (22) (23)
HD 35187	0.5	42	0.003 ± 1.800E-4	3	(1) (4)
CO Ori	1.0	16	<0.006	1	(8)
HD 36112	1.5	31	0.006 ± 1.140E-4	3	(1) (5)
HD 245185	0.1	46	0.016 ± 0.003	2	(5)
T Ori	1.0	28	0.108 ± 0.023	1	(8)
CQ Tau	0.4	19	0.028 ± 3.410E-4	2	(5)
V380 Ori	1.0	33	0.041 ± 0.016	1	(34)
BF Ori	1.0	25	0.005 ± 0.002	1	(8)
HD 290764	1.0	19	0.244 ± 0.026	1	(19)
V599 Ori	1.0	22	0.091 ± 0.007	1	(36)
RR Tau	0.3	29	0.058 ± 0.005	2	(31)
HD 250550	1.0	38	<0.085	1	(7)
HD 41511	0.3	16	0.019 ± 0.002	2	(2)
GSC 1876-0892	1.0	71	19.646 ± 6.445	1	(9)
LkHa 208	1.0	17	<0.014	1	(27)
MWC 137	1.2	143	1.948 ± 0.281	6	(14)
VY Mon	1.9	58	0.052 ± 0.006	5	(1) (31)
LkHa 215	1.8	70	0.061 ± 0.015	3	(14)
HD 259431	1.0	44	<0.052	1	(14)
HT CMa	1.0	33	<0.180	1	(6)
Z CMa	1.9	36	1.383 ± 0.017	8	(33)
PDS 241	1.0	172	57.362 ± 1.616	9	(28)
V388 Vel	1.9	47	0.294 ± 0.093	3	(35)
HD 76534	1.0	101	<0.019	1	(6)
PDS 37	1.0	101	15.663 ± 3.040	1	(29)
HD 97048	1.6	24	0.094 ± 0.007	3	(25) (26)
HD 100453	1.0	17	0.025 ± 0.002	1	(4)
HD 100546	1.3	13	0.061 ± 0.003	4	(4) (6) (10)
HD 104237	1.0	19	0.008 ± 0.002	1	(6)
HD 135344B	1.4	30	0.013 ± 0.002	3	(1) (11)
HD 135344	1.7	27	0.011 ± 0.009	3	(10)
HD 139614	0.6	29	0.022 ± 0.001	4	(4) (11)
HD 141569	1.0	46	1.460E-4 ± 1.570E-5	3	(1) (5)
HD 142666	0.5	30	0.013 ± 0.001	3	(1) (11)
HD 142527	0.3	19	0.211 ± 5.810E-5	2	(5)
HD 143006	1.0	15	0.032 ± 4.940E-5	1	(12)
HD 144432	1.6	6	0.021 ± 0.002	3	(4)
HR 5999	0.0	15	0.008 ± 2.190E-4	2	(1) (13)
HD 150193	0.6	40	0.004 ± 0.001	4	(1) (2) (4)

References. mm flux measurements: (1) Sandell et al. (2011); (2) Mannings & Sargent (1997); (3) Guedel et al. (1989); (4) Acke et al. (2004); (5) Péricaud et al. (2017); (6) Henning et al. (1994b); (7) Hillenbrand et al. (1992); (8) Mendigutía et al. (2012); (9) Ginsburg et al. (2013); (10) Planck Collaboration (2013); (11) Sylvester et al. (1996); (12) Barenfeld et al. (2016); (13) Meeus et al. (2012); (14) Mannings (1994); (15) Di Francesco et al. (2008); (16) Mannings & Sargent (2000); (17) Pezzuto et al. (1997); (18) Kauffmann et al. (2008); (19) Kraus et al. (2017); (20) Piétu et al. (2006); (21) Piétu et al. (2003); (22) Sylvester et al. (2001); (23) Sheret et al. (2004); (24) Cotten & Song (2016); (25) Henning et al. (1993); (26) Ribas et al. (2018); (27) Natta et al. (1997); (28) Planck Collaboration Int. LIV. (2018); (29) Urquhart et al. (2014); (30) Enoch et al. (2008); (31) Boissier et al. (2011); (32) Natta et al. (2000); (33) Alonso-Albi et al. (2009); (34) Reipurth et al. (1993); (35) Giannini et al. (1996); (36) Mairs et al. (2016).

Table B.3. continued.

Object	β	T_D (K)	M_{disk} ($M_\odot$)	N° photometric points	References
AK Sco	0.3	27	0.003 ± 7.350E-6	4	(4) (5)
V921 Sco	1.0	215	0.360 ± 0.047	1	(7)
HD 158643	1.0	28	3.780E-4 ± 4.530E-5	1	(13)
HD 163296	0.4	34	0.034 ± 0.001	8	(14)
HD 169142	1.2	31	0.010 ± 3.090E-4	5	(1) (4) (5)
MWC 297	0.0	200	0.029 ± 0.001	3	(1) (6)
VV Ser	0.0	35	9.540E-4 ± 2.730E-4	2	(31)
V431 Sct	1.0	101	0.225 ± 0.062	1	(6)
PDS 520	1.0	16	0.162 ± 0.021	1	(30)
AS 310	1.0	215	0.768 ± 0.050	1	(6)
HD 176386	1.0	33	0.121 ± 0.010	1	(15)
TY CrA	1.0	38	<0.017	1	(17)
HD 179218	1.4	24	0.029 ± 0.003	2	(16)
WW Vul	1.0	23	0.016 ± 0.001	1	(4)
V1685 Cyg	1.0	101	0.255 ± 0.033	1	(7)
V1686 Cyg	1.0	16	<0.040	1	(8)
V1478 Cyg	0.0	35	12.973 ± 0.349	2	(1)
HD 200775	1.0	71	<0.015	1	(17)
HD 235495	1.0	33	0.038 ± 0.005	1	(18)
V361 Cep	1.0	71	<0.032	1	(7)
V373 Cep	1.0	44	<0.051	1	(33)
AS 477	1.0	33	<0.051	1	(7)
SV Cep	1.0	23	0.005 ± 0.001	1	(27)
MWC 1080	1.6	229	0.308 ± 0.039	7	(14)
LkHa 259	1.0	18	93.196 ± 40.276	1	(10)

Appendix C: SEDs

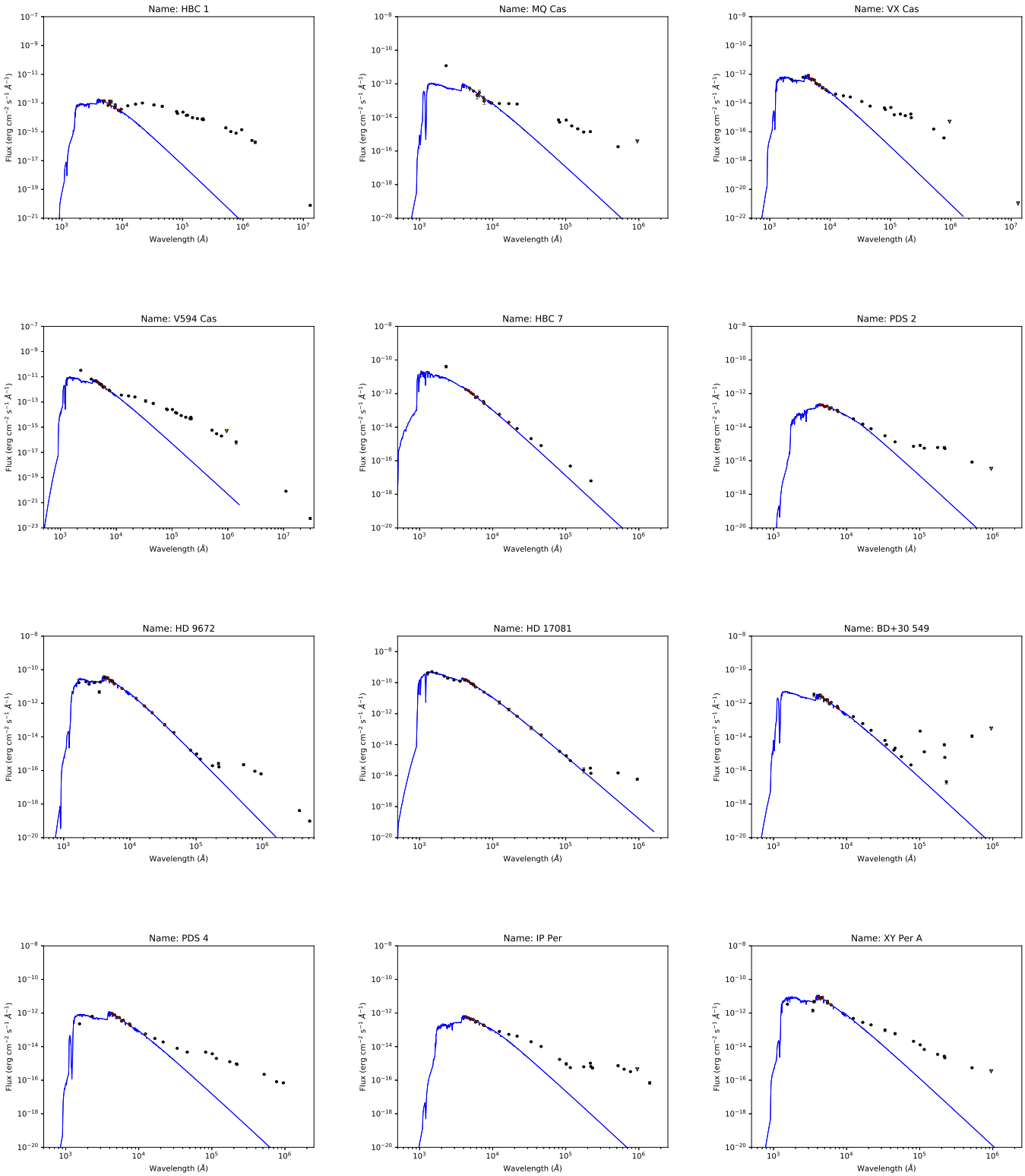

Fig. C.1. SEDs of the whole sample. The solid blue line corresponds to the best photospheric model that fits the deredenned optical photometry (red dots). Yellow triangles are upper limits.

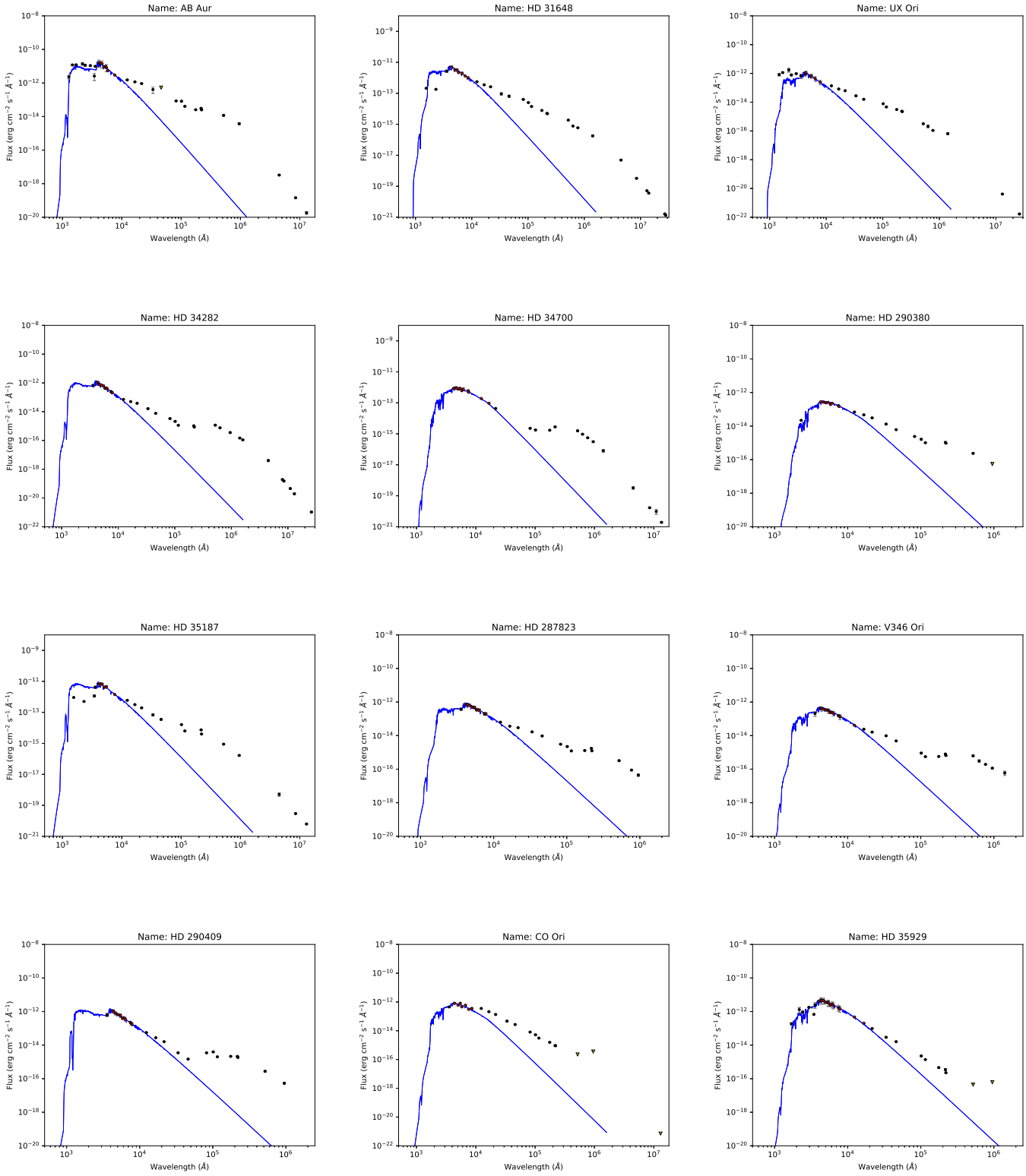

Fig. C.1. continued.

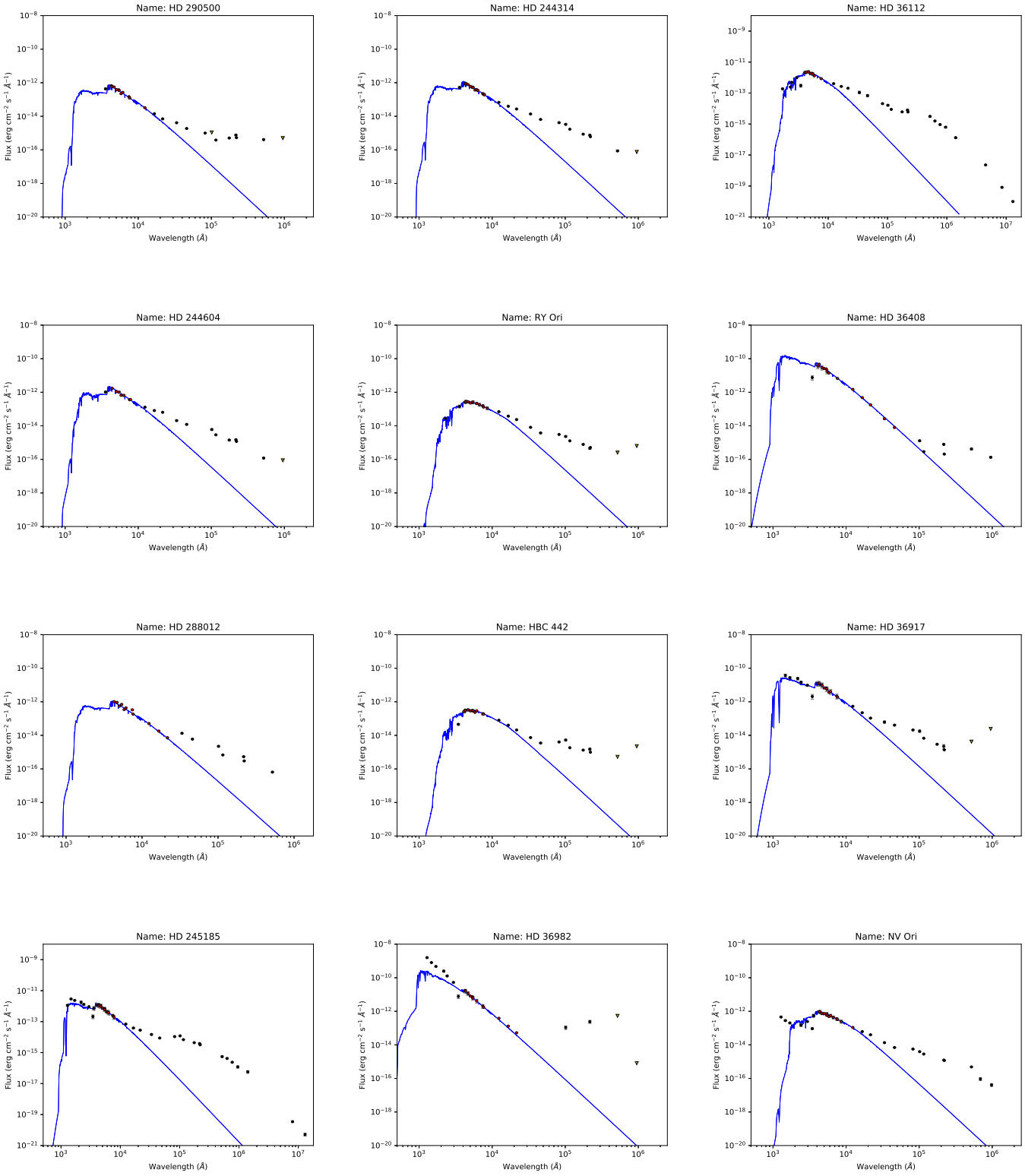

Fig. C.1. continued.

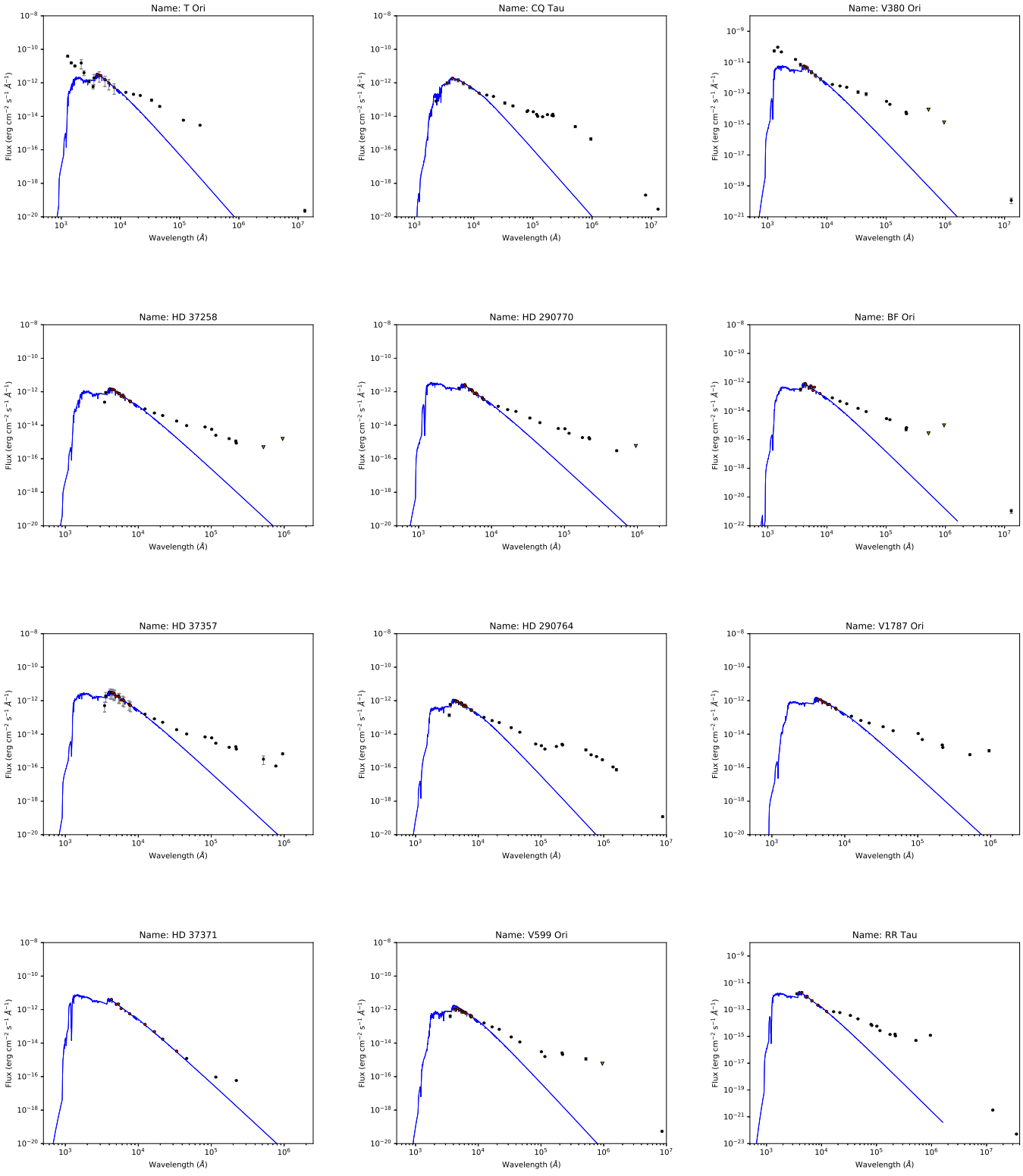

Fig. C.1. continued.

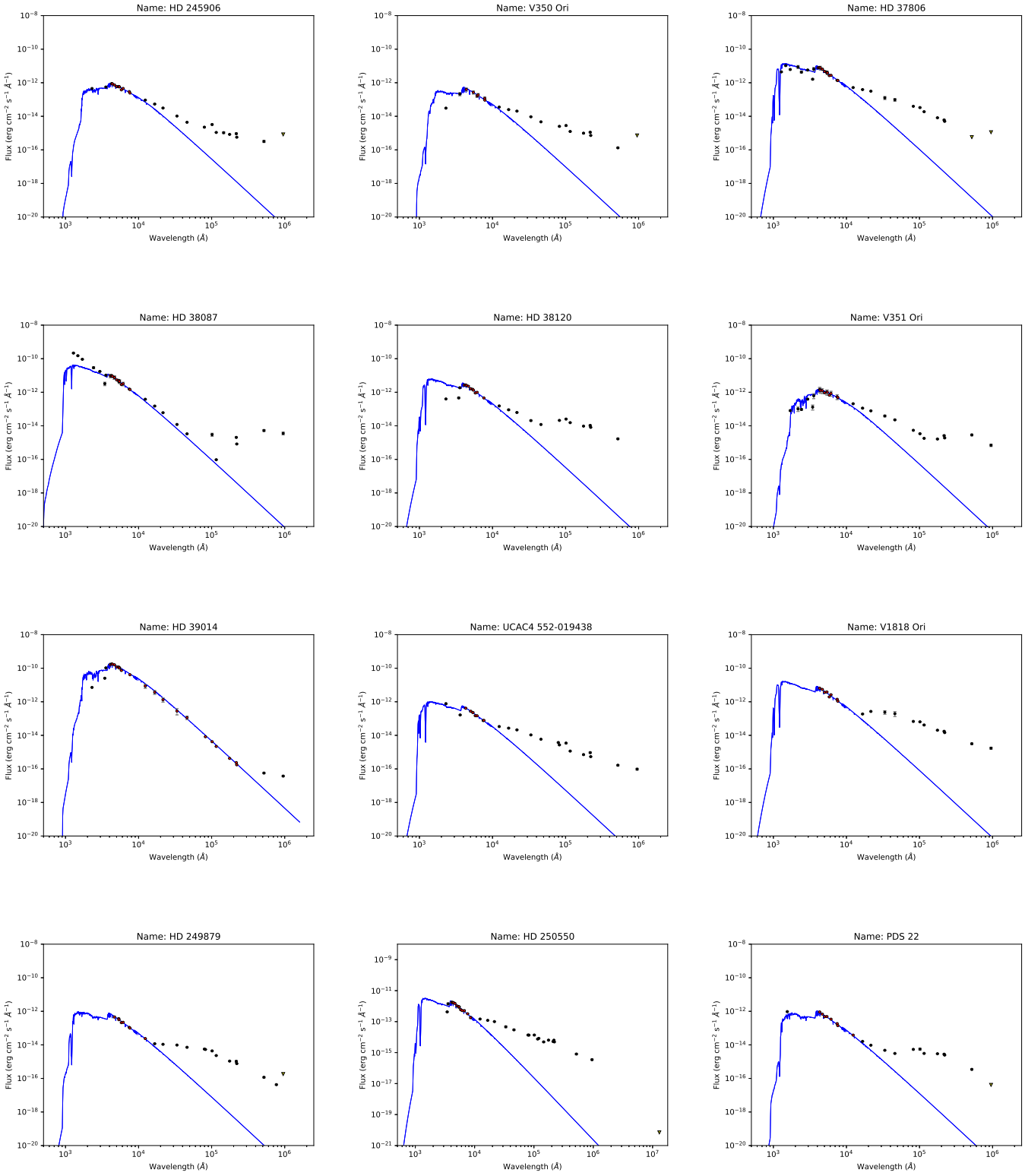

Fig. C.1. continued.

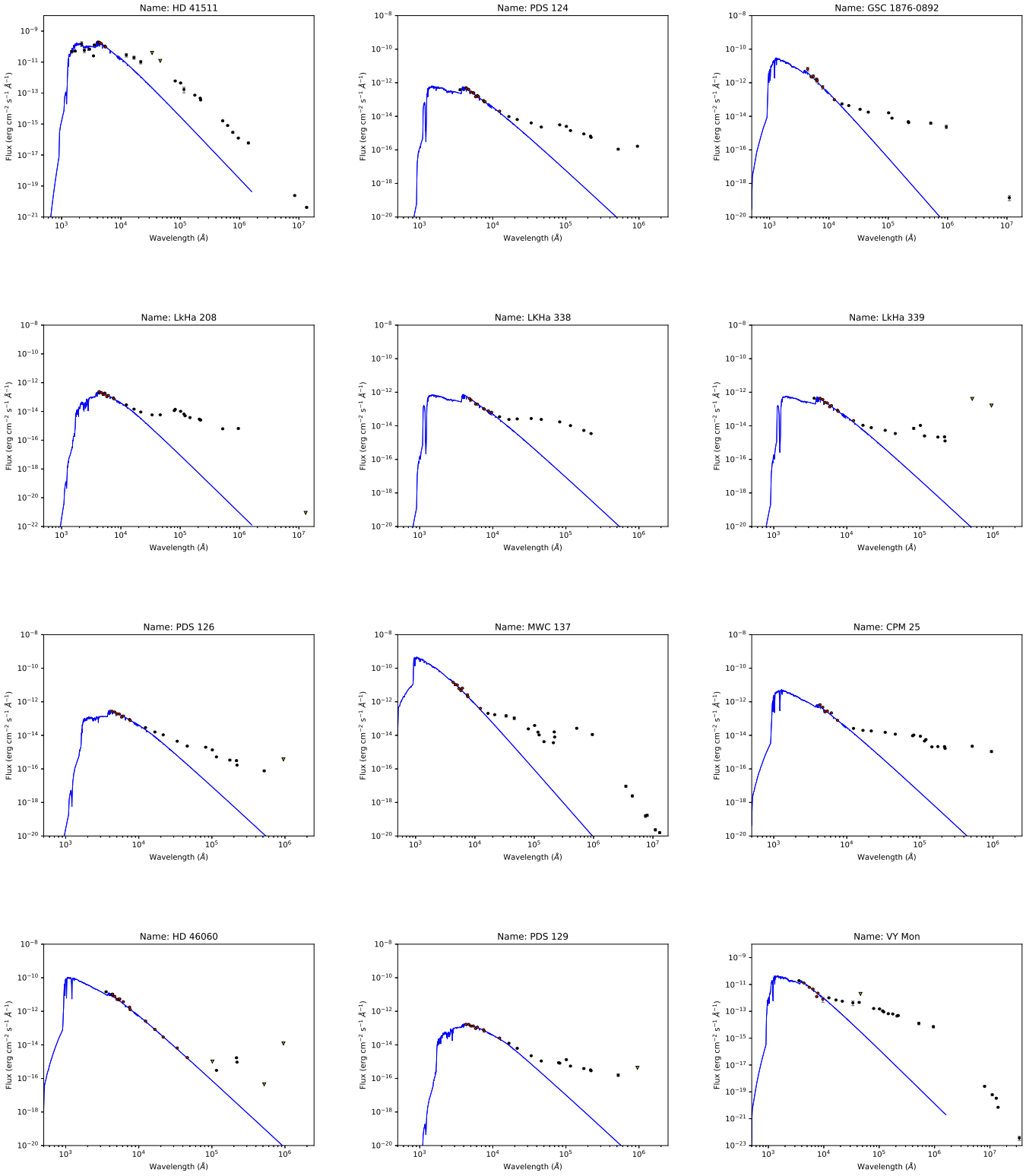

Fig. C.1. continued.

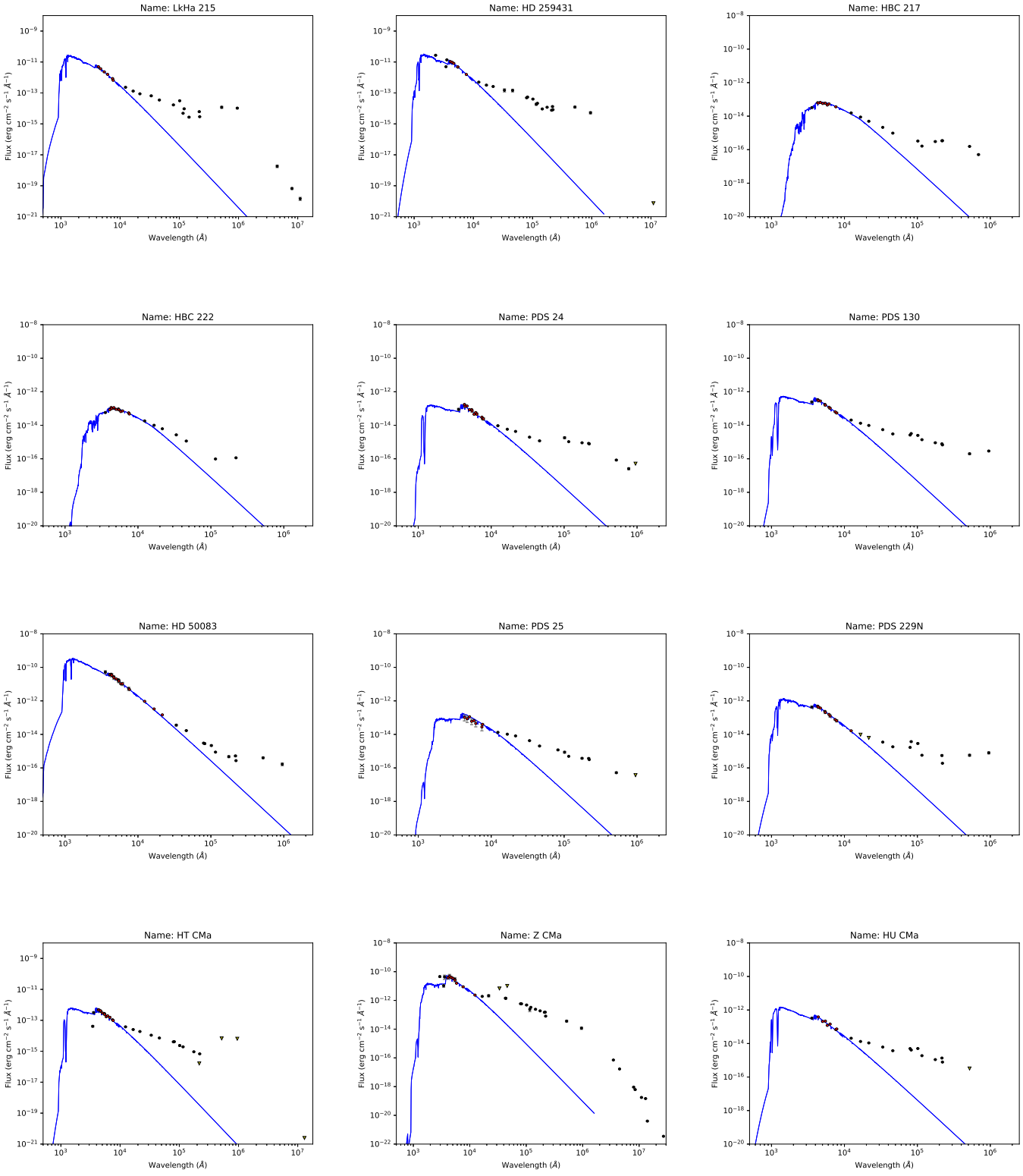

Fig. C.1. continued.

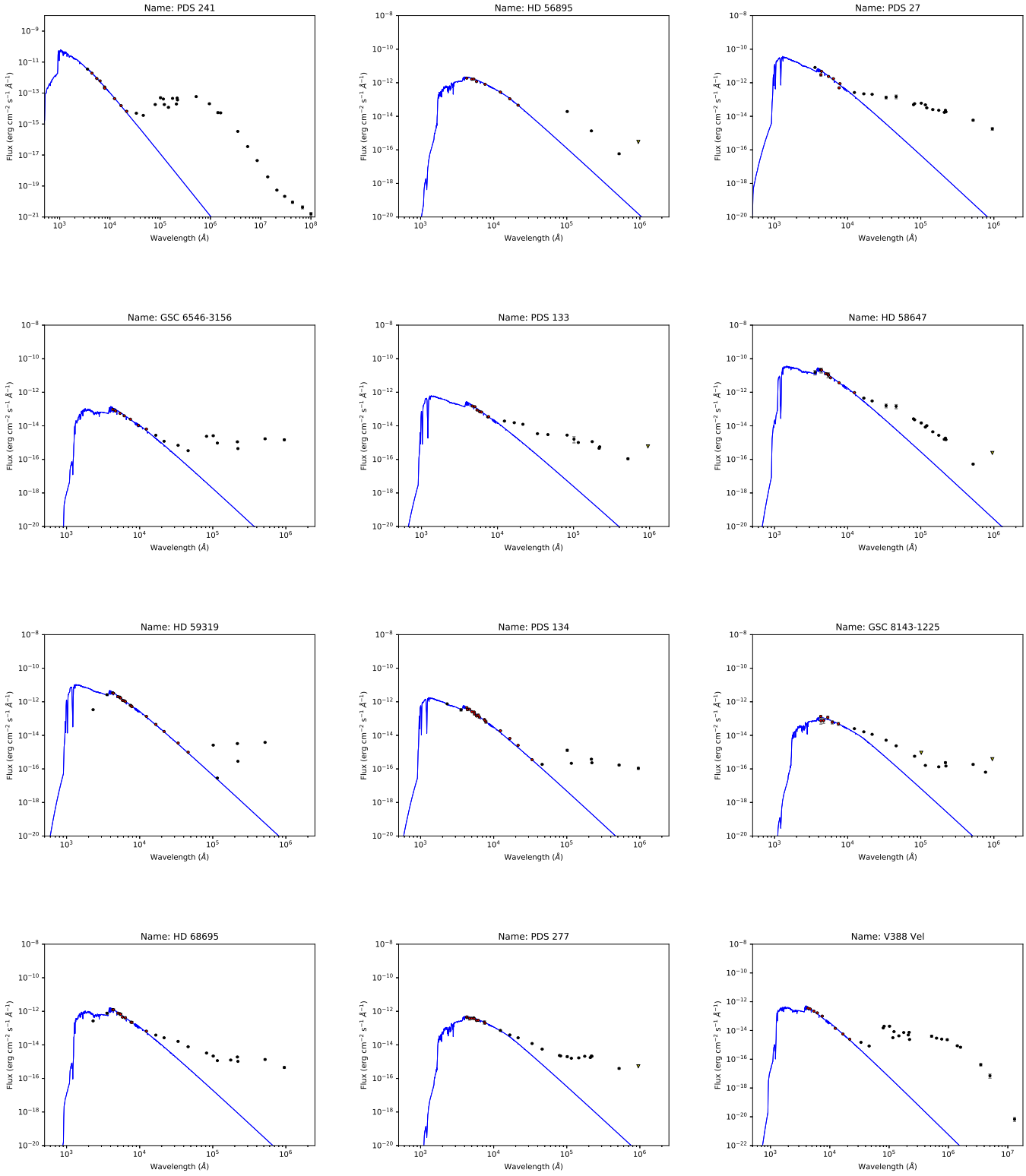

Fig. C.1. continued.

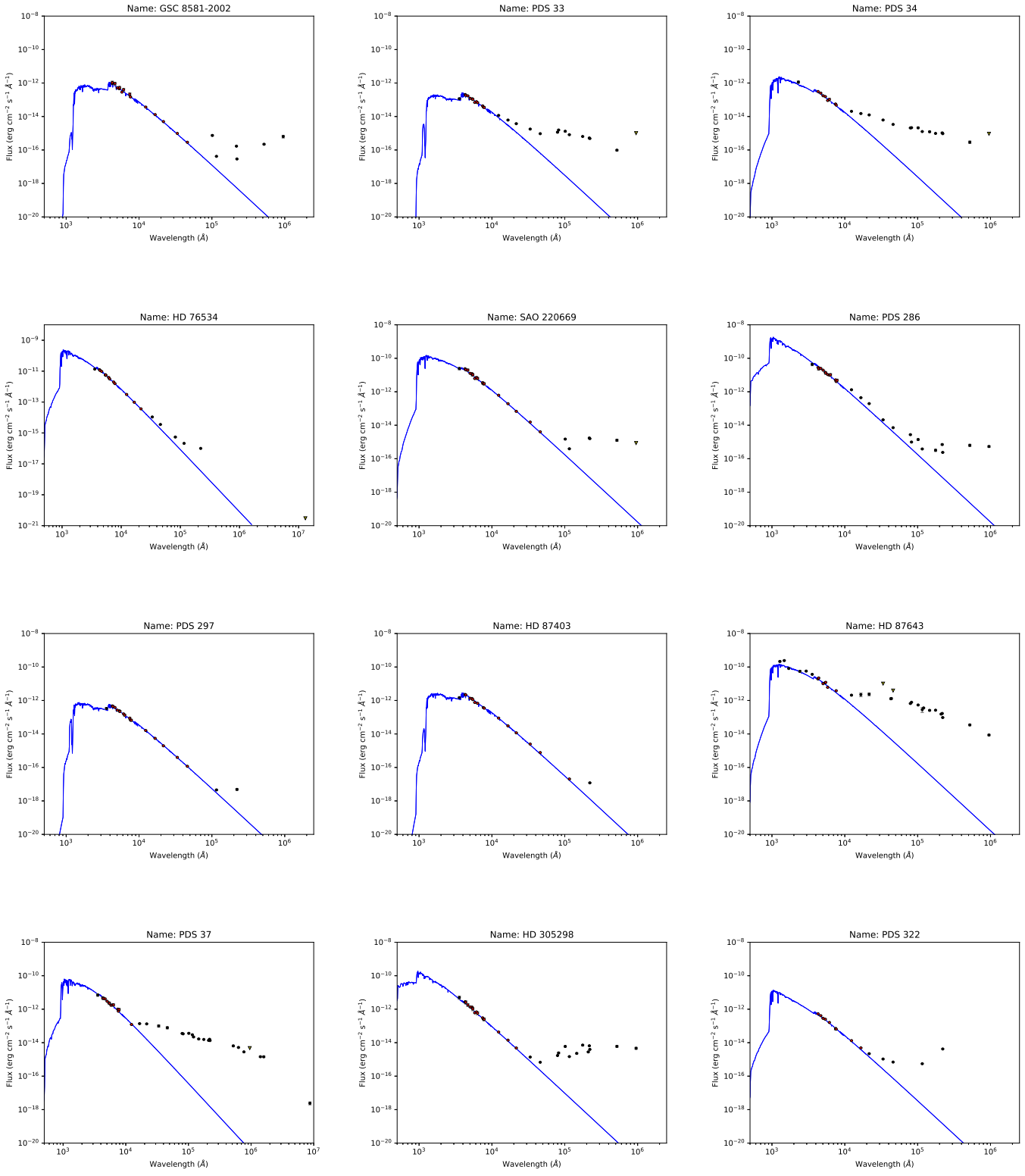

Fig. C.1. continued.

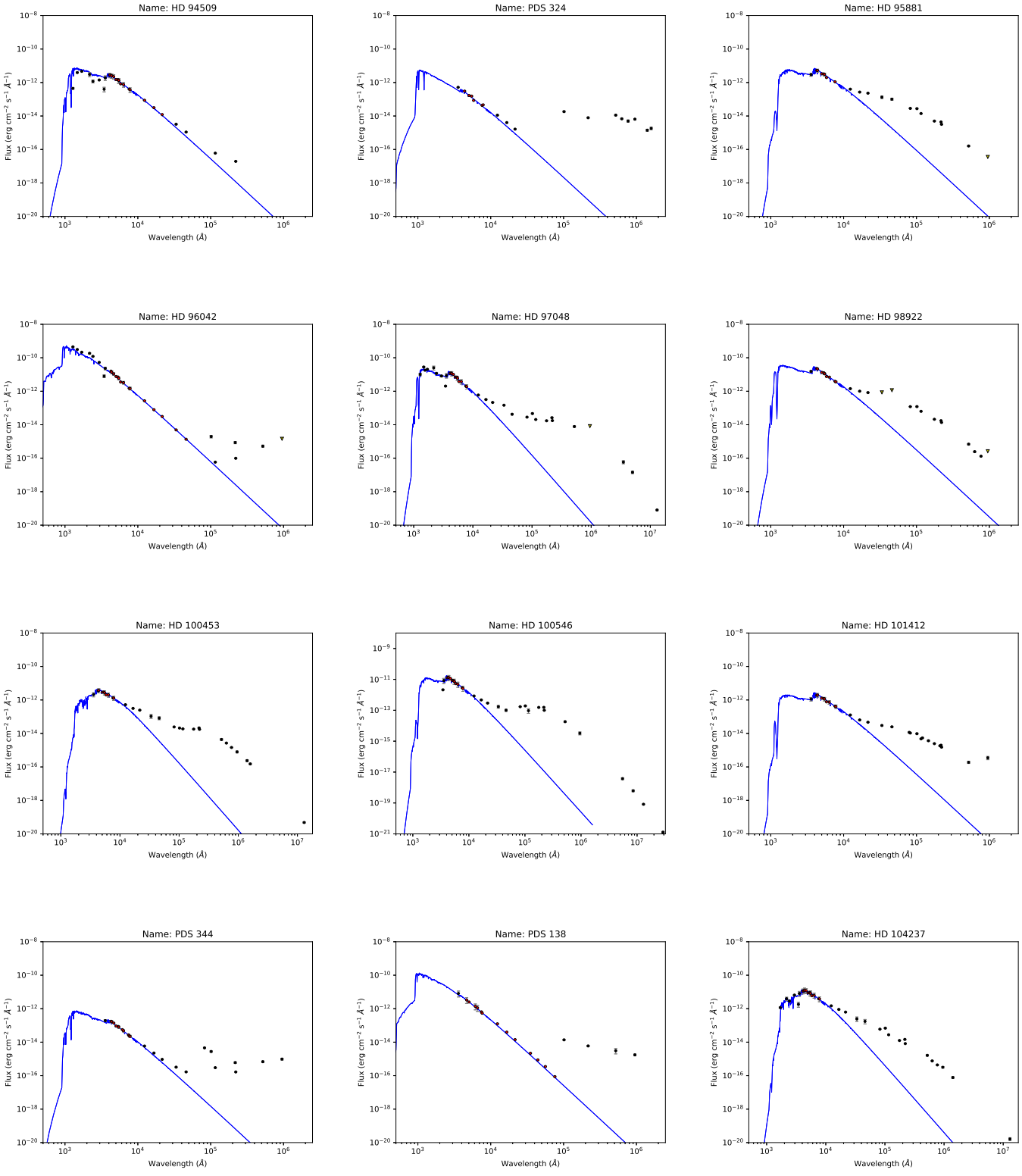

Fig. C.1. continued.

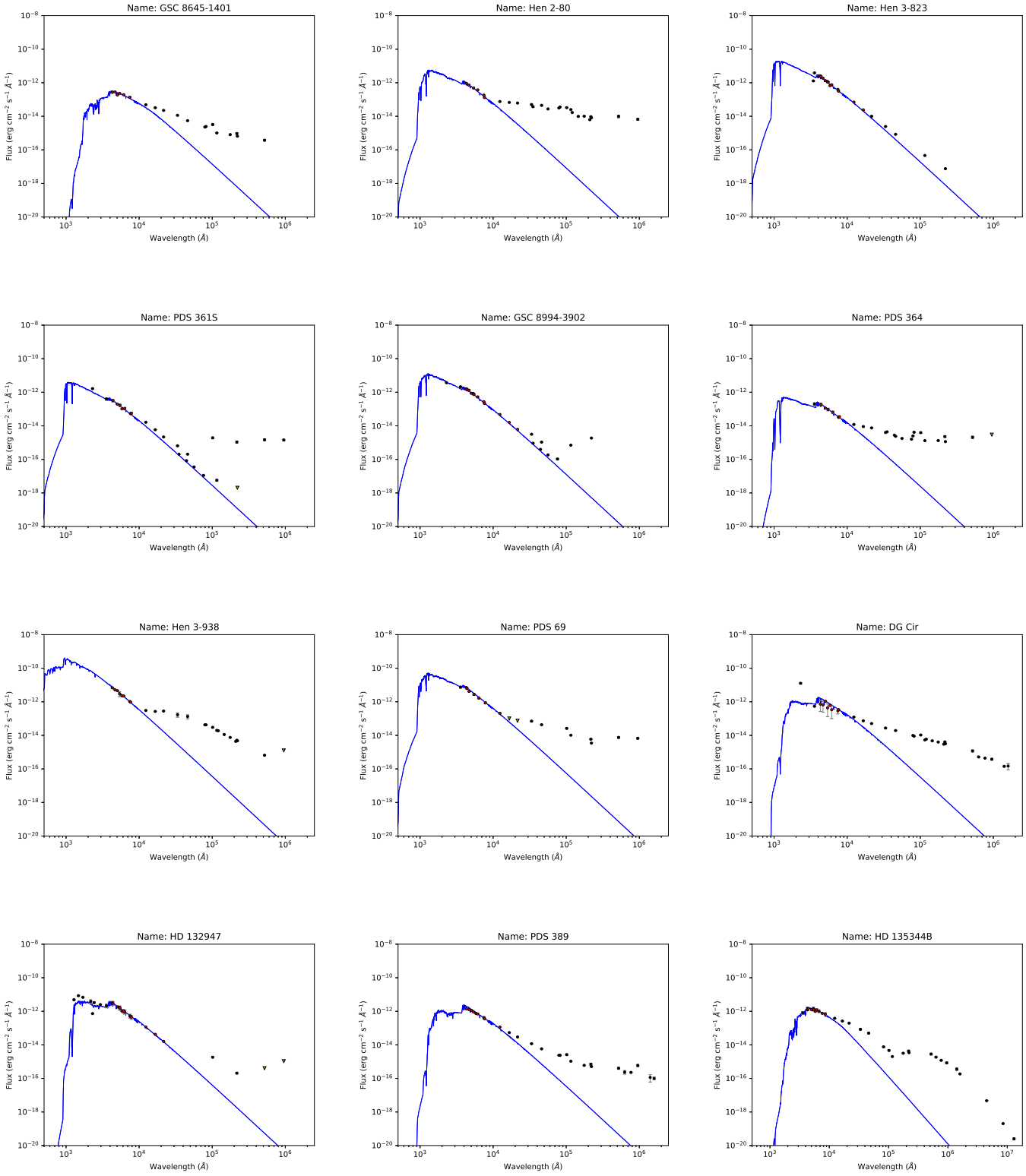

Fig. C.1. continued.

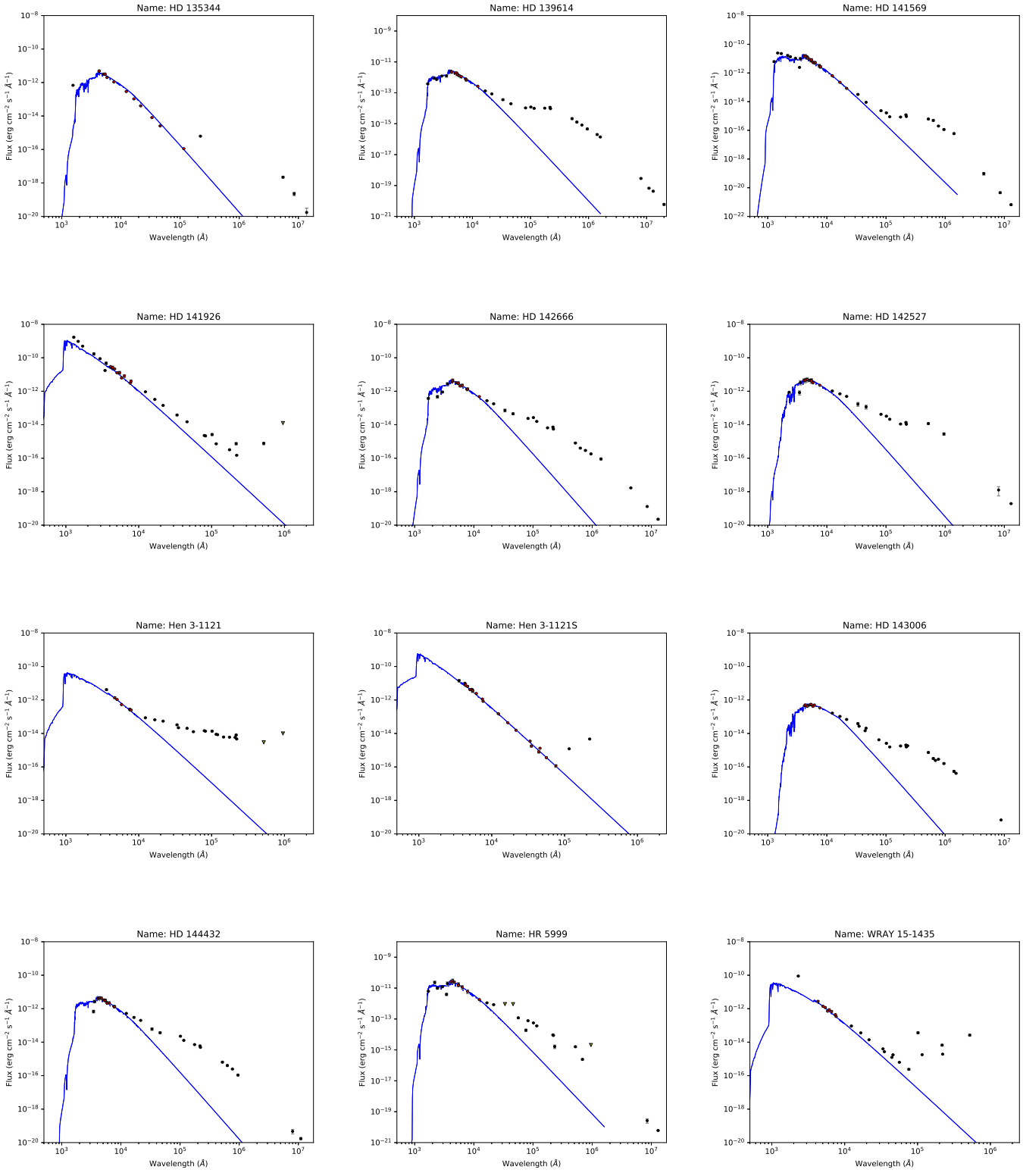

Fig. C.1. continued.

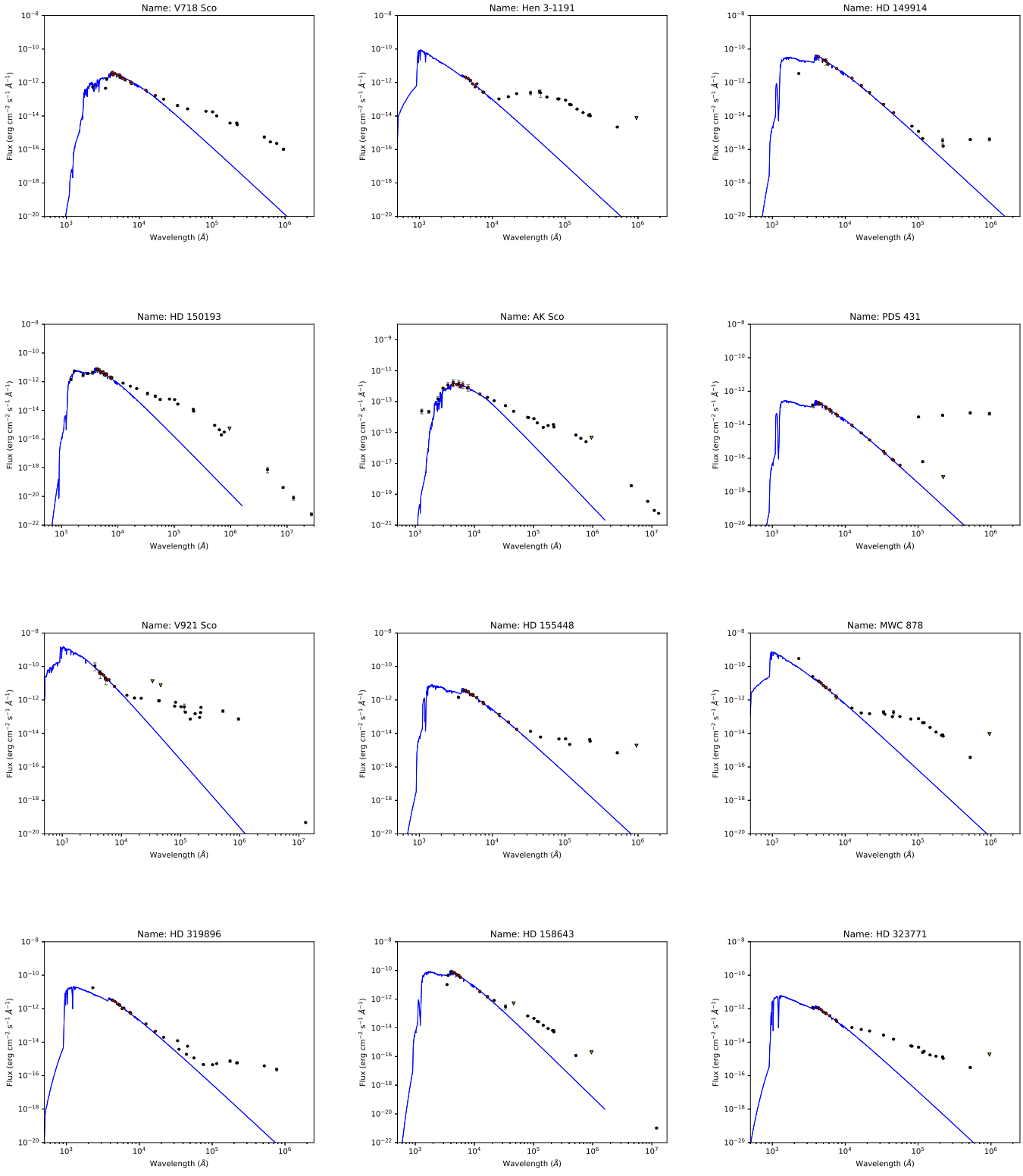

Fig. C.1. continued.

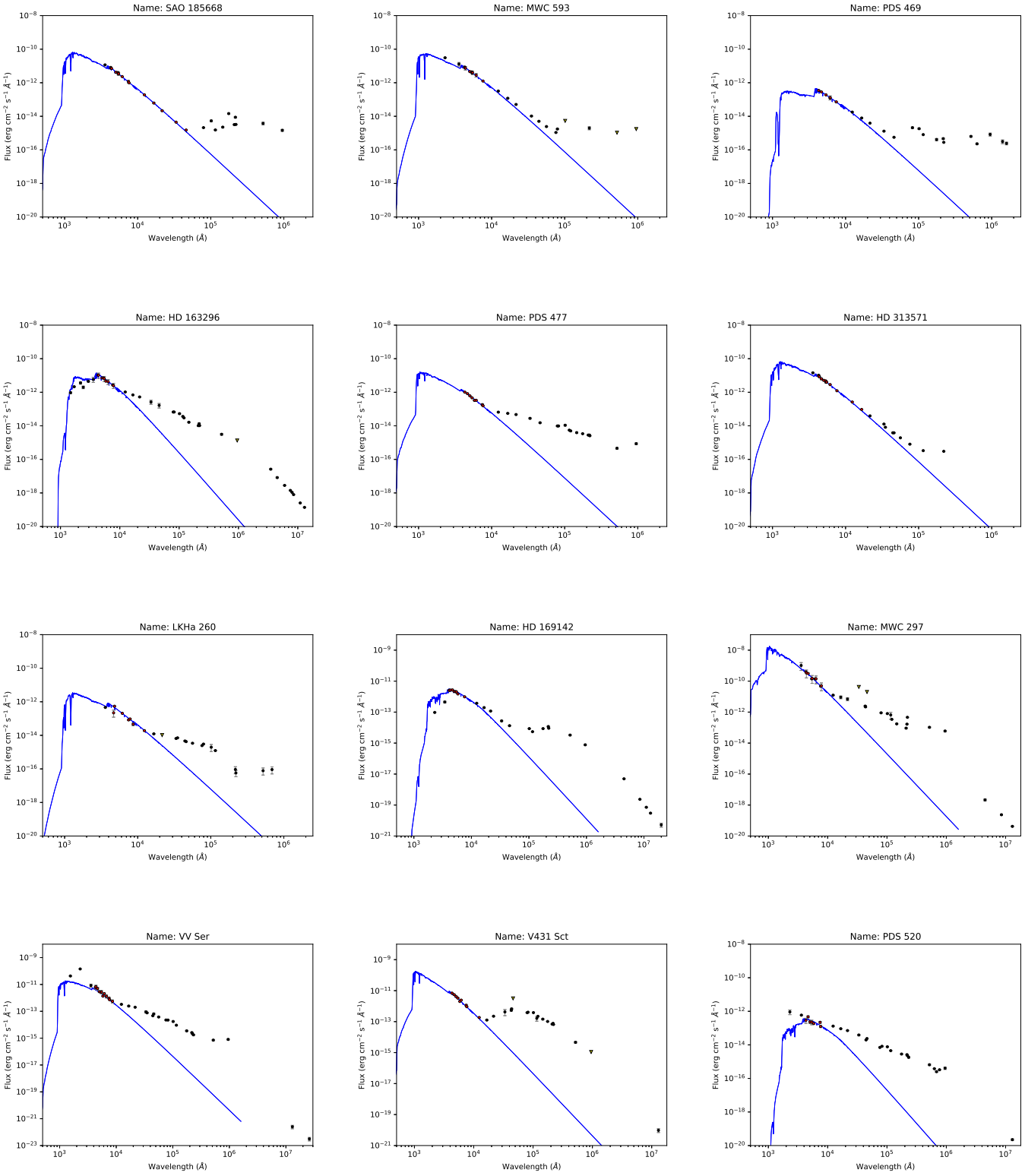

Fig. C.1. continued.

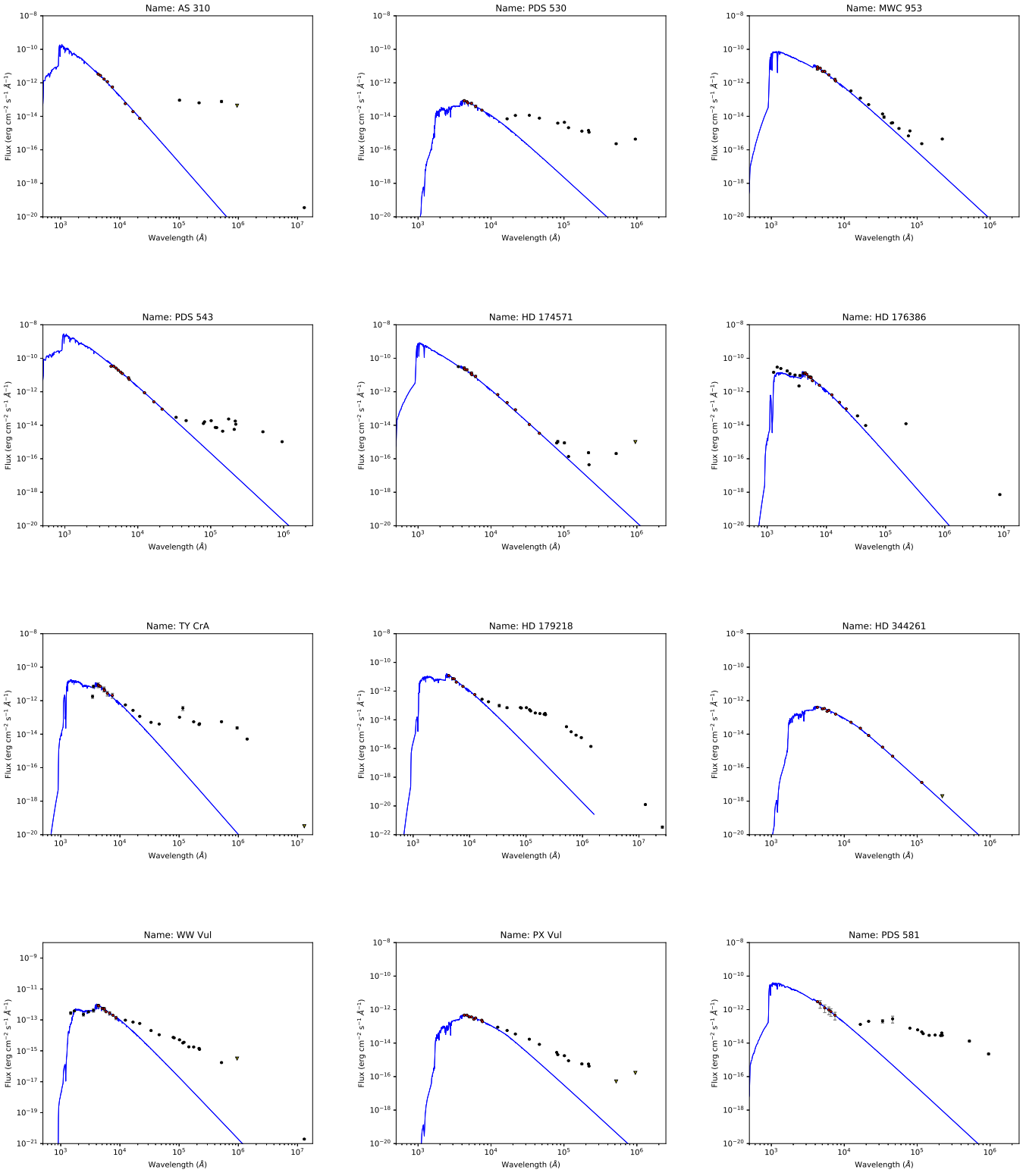

Fig. C.1. continued.

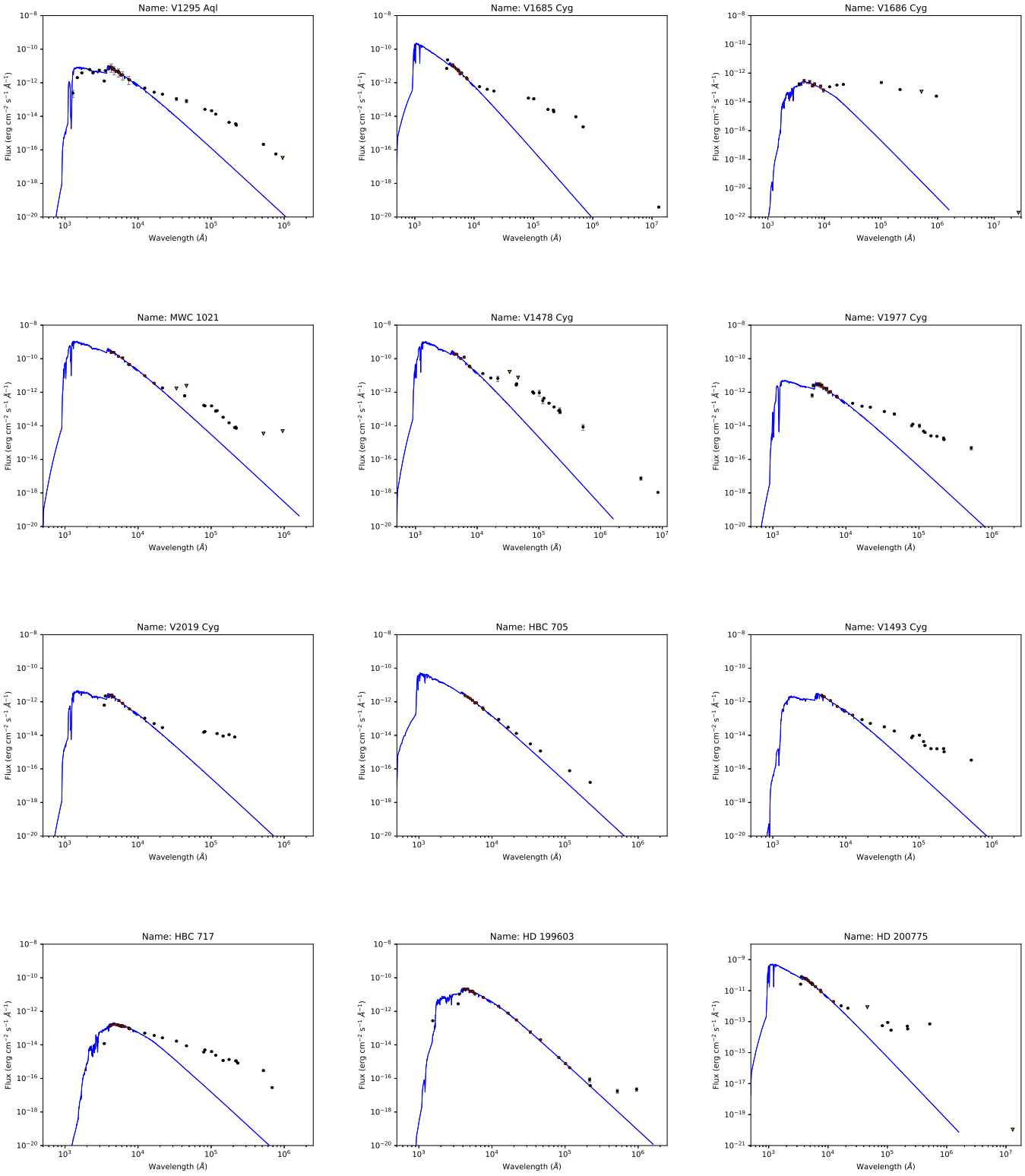

Fig. C.1. continued.

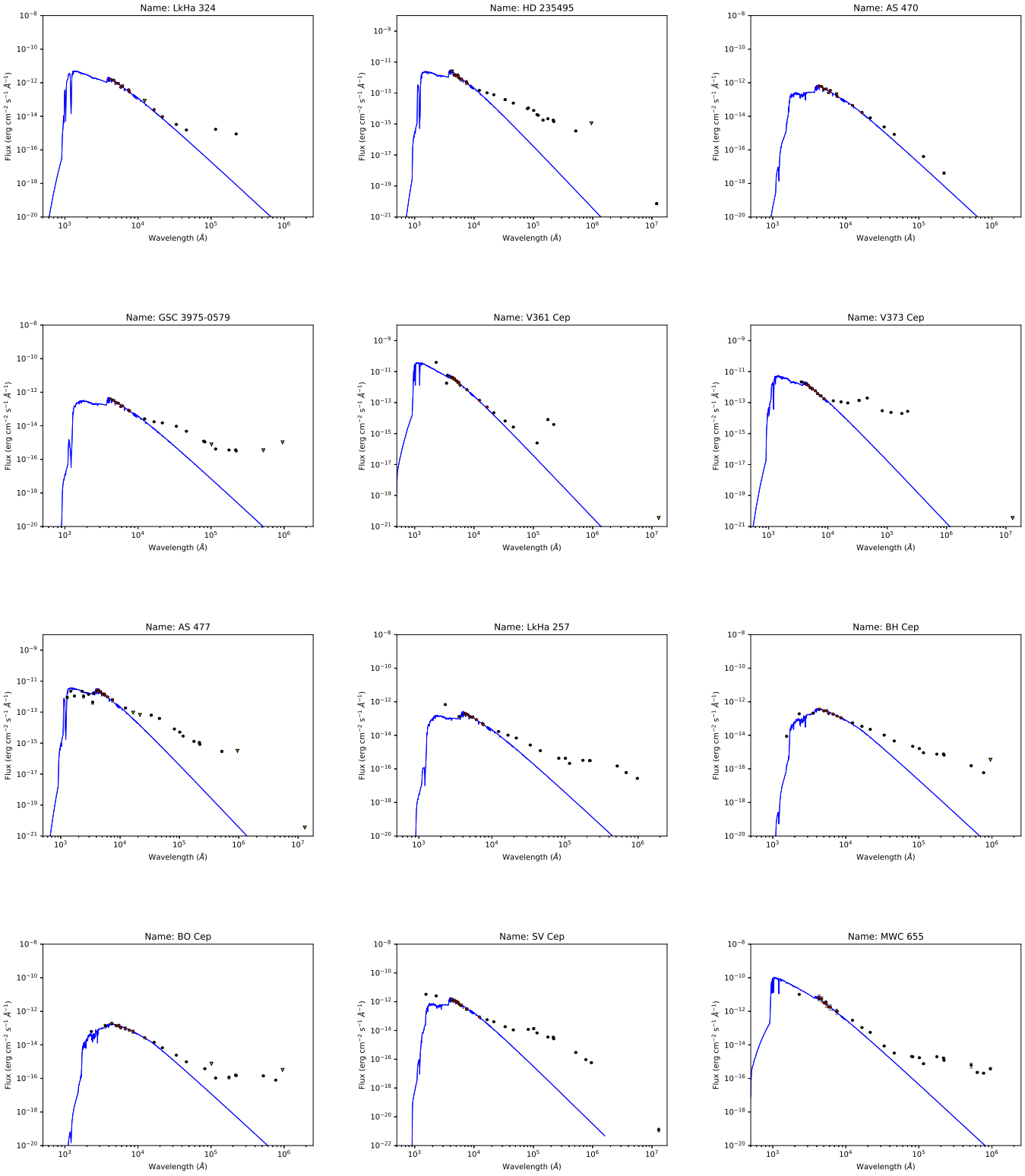

Fig. C.1. continued.

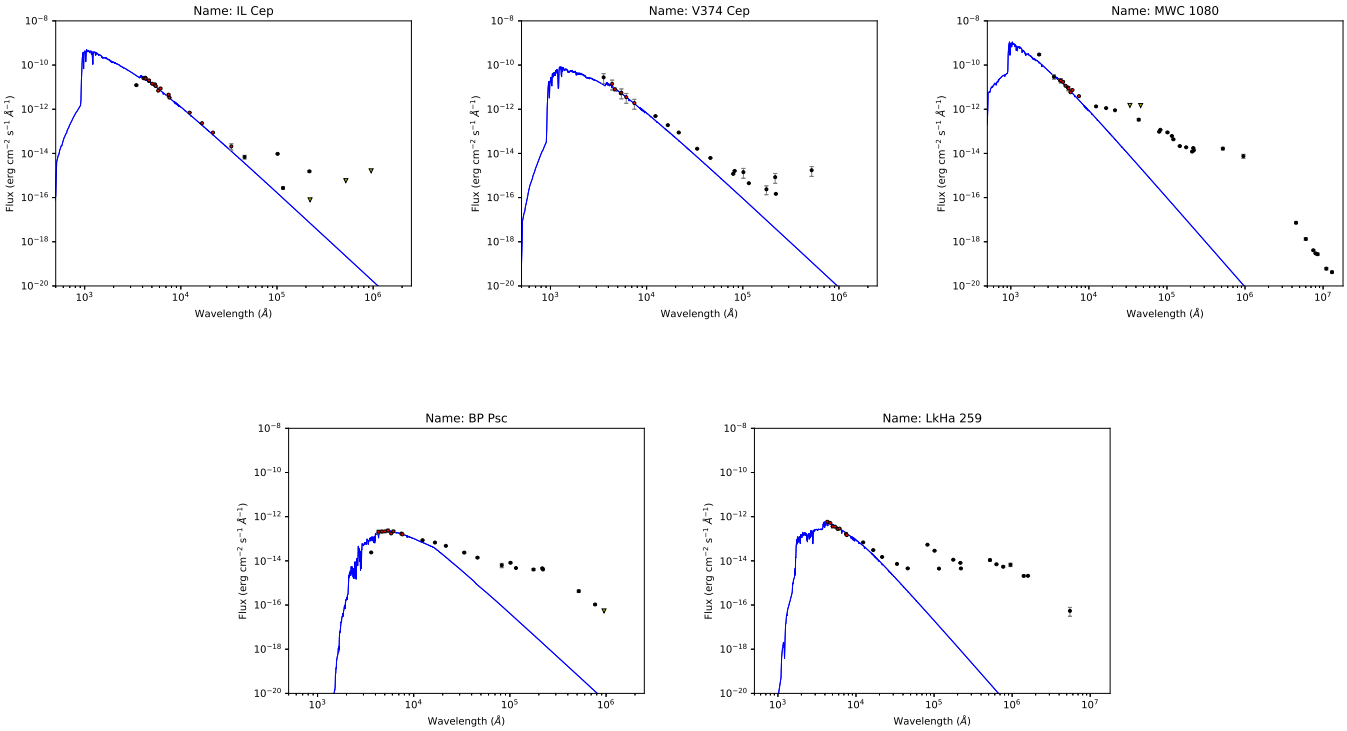

Fig. C.1. continued.